



City Research Online

City, University of London Institutional Repository

Citation: Fostiropoulos, S. R. (2020). Heat transfer and breakup of emulsified fuel droplets. (Unpublished Doctoral thesis, City, University of London)

This is the accepted version of the paper.

This version of the publication may differ from the final published version.

Permanent repository link: <https://openaccess.city.ac.uk/id/eprint/25882/>

Link to published version:

Copyright: City Research Online aims to make research outputs of City, University of London available to a wider audience. Copyright and Moral Rights remain with the author(s) and/or copyright holders. URLs from City Research Online may be freely distributed and linked to.

Reuse: Copies of full items can be used for personal research or study, educational, or not-for-profit purposes without prior permission or charge. Provided that the authors, title and full bibliographic details are credited, a hyperlink and/or URL is given for the original metadata page and the content is not changed in any way.

Heat transfer and breakup of emulsified fuel droplets

Fostiropoulos Stavros Rafail

Thesis submitted for the fulfilment of the requirements for
the Degree of Doctor of Philosophy



**School of Mathematics, Computer Science &
Engineering**

Department of Mechanical Engineering & Aeronautics

October 2020

Contents

Contents	vii
List of Figures	xi
List of Tables	xv
Acknowledgements	xvii
Declaration	xix
Abstract	xxi
Thesis Contribution	xxiii
Nomenclature	xxv
Chapter 1 Introduction	1
1.1 Background and Motivation.....	1
1.1.1 Addition of water in combustion process	3
1.1.2 Breakup of water in fuel emulsion	4
1.2 Literature review	5
1.2.1 Boiling heat transfer-Vapor bubble growth	5
1.2.2 Emulsion fuel droplet breakup (Puffing/Micro-explosion)	9
1.2.3 Aerodynamic breakup of neat fuel droplet.....	12
1.3 Thesis outline.....	13
Chapter 2 Numerical models	14
2.1 Mathematical description of the model equations	14
2.1.1 Fluid flow and Volume of Fluid.....	15
2.2 Vapor bubble formation model	17
2.3 Phase change model-OCASIMAT algorithm.....	19
2.4 Local grid refinement	21
Chapter 3 Preliminary computational studies-Model validation	24

3.1 Vapor bubble growth inside an infinite liquid pool	24
3.1.1 Theoretical solution	24
3.1.2 CFD simulations	26
3.2 Nonlinear droplet oscillation.....	31
3.3 Breakup of stationary emulsion droplet	32
3.3.1 Computational setup and examined conditions.....	33
3.3.2 Results	34
Chapter 4 Computational study of emulsion droplet breakup	37
4.1 Convective heating of emulsion droplets	37
4.1.1 Computational setup and examined conditions.....	37
4.1.2 Results	38
4.2 Emulsion breakup subjected to aerodynamic forcing	42
4.2.1 Computational setup and examined conditions.....	42
4.2.2 Results	45
4.3 Conclusions.....	52
Chapter 5 A simple model for breakup time prediction of emulsion droplets.....	54
5.1 Examined conditions	55
5.2 Mathematical description	57
5.3 Discussion	59
5.3.1 Overall performance.....	59
5.3.2 Parametric study with We and $p - T$ conditions	59
5.3.3 Extrapolation to emulsion configurations not studied with CFD.....	64
5.3.4 Model performance for multiple parameter variation.....	66
5.4 Conclusions.....	67
Chapter 6 Conclusions and future work	69
6.1 Conclusions.....	69
6.2 Future work	70
6.2.1 Case-specific work	70
6.2.2 Further expansion and applications of the CFD methodology	72
Appendix A. Fitting model	74
Derivation of heating time period.....	74
Derivation of bubble growth time period	77

Publications.....	80
Bibliography	82

List of Figures

Figure 1-1: Schematic diagram of emulsion fuel spray.....	2
Figure 1-2: Water addition methods.	3
Figure 1-3: Micro-explosion of water in fuel emulsion droplet.	5
Figure 1-4: Pressure and temperature field inside and outside of the vapor bubble for surface tension (a), inertia (b) and heat diffusion (c) growth phases.	6
Figure 1-5: Puffing of a spray emulsion droplet with diameter $d = 50 \mu\text{m}$	11
Figure 2-1: An interface between two fluids (a) and the corresponding volume fractions (b). Derived by [78].....	16
Figure 2-2: Configuration of vapor bubble formation	19
Figure 2-3: OCASIMAT one cell algorithm for the evaluation of temperature gradient at the interface.....	20
Figure 2-4: VoF values indicating the initial location (a) and collision (b) of two droplets.....	22
Figure 3-1: Schematic representation of spherical bubble growth	25
Figure 3-2: Computational mesh refined locally alongside with boundary conditions (Left panel). Schematic illustration of thermal boundary layer (Right panel).....	27
Figure 3-3: Temperature distribution during bubble growth at three time instances.	29
Figure 3-4: Prediction of the bubble growth rate for different grid resolutions	30
Figure 3-5: Map indicating the error between the predictions of CFD and analytical solution.....	31
Figure 3-6: Nonlinear droplet oscillations predicted by the current code (Left panel) and the numerical model of [83] (Right panel).	32
Figure 3-7: Schematic illustration of the stationary emulsion droplet (Left panel) alongside with the computational mesh (right panel)	33
Figure 3-8: Stationary emulsion droplet breakup at $t = 0.4$, $t = 2.2$ and $t = 3.2 \mu\text{s}$, predicted by the current CFD methodology (Right panel) and that of [26] (Left panel).	35

Figure 4-1: Upper panel: Computational 2-D planar domain of an emulsion droplet with one embedded water sub-droplet, initially located upstream. Lower panel: Computational mesh with 3 levels of refinement at the liquid-air interfaces	38
Figure 4-2: Convective heating of an emulsion droplet with one embedded water sub-droplet located upstream. The airflow is from the left to the right	40
Figure 4-3: Time sequence of the three water sub-droplets moving inside an oil droplet. The air flow is from the left to the right.....	41
Figure 4-4: Computational axisymmetric domain, with zoom at levels of local refinement around the HFO-air and HFO-water interfaces.....	43
Figure 4-5: Temporal evolution of emulsion droplet breakup. Upper part: Temperature profile. Lower part: HFO, water and vapor phases indicated by blue, green and red respectively.	47
Figure 4-6: Nondimensional vapor bubble radius predicted by Scriven solution (red solid line) and CFD simulation (black scatter) for the front bubble with $We = 70$ and a corresponding breakup initiation time (vertical blue line).....	47
Figure 4-7: Temporal evolution of W/HFO emulsion droplet (Left panel) and neat HFO droplet (Right panel) for We number equal to 70.	48
Figure 4-8: Breakup time of W/HFO emulsion droplet for a range of We numbers (black scatter). Aerodynamic breakup of neat HFO droplet for the corresponding range of We numbers (blue solid line).....	49
Figure 4-9: Temporal evolution of the dimensionless surface area of the W/HFO emulsion (scatter) and the neat HFO droplet (blue line)	51
Figure 4-10: Breakup initiation time of W/HFO emulsion with superheat degree (red scatter), bubble surface depth (blue scatter) and We number (black scatter).....	52
Figure 5-1: Schematic illustration of the emulsion droplet.....	55
Figure 5-2: Emulsion breakup time as predicted by Eq. 5-1 (black solid line) alongside with $\pm 10\%$ deviation lines (black dashed lines) and the CFD simulations (scatter symbols)	59
Figure 5-3: Dimensional (upper panel) and non-dimensional (lower panel) breakup time (black solid line) of an emulsion droplet alongside with heating (red dashed line) and bubble growth (blue dash-dot line) times predicted by the semi analytical model and CFD simulations (black scatter symbols) against We . Black dashed line indicates breakup initiation time of a neat HFO droplet	61
Figure 5-4: Dependence of t_{grow} (red line), β (black line) and g_p (blue line) on pressure ($T^\infty = 1000$ K).....	62

Figure 5-5: Breakup time maps for various pressure and temperature values (shown in vertical and horizontal axis respectively). The isolines correspond to different breakup times ($We = 68, \delta = 0.06, DwDoil = 0.2$)..... 63

Figure 5-6: Heating (black scatter symbol) and breakup (red scatter symbol) time of an emulsion droplet against the radius of the water droplet. 64

Figure 5-7: Upper panel: Emulsion breakup initiation time against water droplet surface depth for two different water droplet sizes and ref $We = 68$. Lower panel: Emulsion breakup initiation time against We for three sets of water droplet surface depth and size. 65

Figure 5-8: Emulsion breakup time as predicted by Eq. 5-1 (black solid line) alongside with $\pm 10\%$ deviation lines (black dashed lines) and the CFD simulations (scatter symbols)..... 67

Figure A-1: Nondimensional heating time predicted by CFD simulations (black scatter symbols) against $T_{sat}' - T_0 T^\infty - T_0$ parameter (upper panel), nondimensional surface depth δ (middle panel) and nondimensional We (lower panel). Fitting functions for CFD model predictions are illustrated with red solid line. 76

Figure A-2: Nondimensional bubble radius predicted by CFD model (black scatter symbols), Scriven solution (blue solid line) and the current analytical model (red solid line)..... 77

Figure A-3: Correction factors gbr (left upper panel), gp (right upper panel), gT (left lower panel) and gWe (right lower panel) calibrated from CFD model predictions (black scatter symbols)..... 78

List of Tables

Table 3.1: Initial conditions and material properties of the default numerical simulation	28
Table 4.1: Thermophysical properties (computed by [91]). The pressure was assumed constant at 30bar.	44
Table 4.2: Non-dimensional numbers.....	44
Table 5.1: Operating conditions for the examined cases. For all cases $Oh \sim 0.9$	57
Table 5.2: Operating conditions for the examined cases.....	66

Acknowledgements

This dissertation is the final destination of a long journey that lasted a bit more than 4 years. I was always thinking about the moment that I would write the current paragraph just as a moment of great relief. Now that I am actually writing it, I am looking back in these days and I feel wistful, since I know that this period of my life was so significant and unique and it will not be repeated again. During my doctoral studies, I have been through difficult moments, where I was feeling disappointed about my research, but I had also moments of great satisfaction. Thankfully, I was blessed to share all these moments with amazing people to whom I would like to say a big ‘Thank you’.

First of all, I would like to thank my first supervisor Prof. Manolis Gavaises. Thanks to him I learnt a lot, while his insightful comments and suggestions helped me to push my research forward. I would like to thank Dr. Nikos Nikolopoulos who gave me the opportunity to work with him at the Center for Research and Technology Hellas (CERTH). Despite his tight schedule, Nikos was always available to discuss my progress and research issues. I have to thank my daily supervisor Prof. Giorgos Strotos. He was the *deus ex machina* which made it possible for me to overcome my obstacles and I owe him a lot. Finally, I could not forget to thank my daily supervisor and friend Dr. Ilias Malgarinos. Besides sharing his knowledge with me, I will never forget the times we laughed our heads off. A big thanks goes to my permanent colleagues from CERTH. Dionysi and Myrtw, I was lucky being in the same office with you. Moreover, I would like to thank my colleagues from HAoS project and City University, Thodoris, Akis, Kostas, Nikos, Daniel and especially Nikos Chatziarsenis, for the amazing time we had when going to meetings and conferences.

Next I would like to thank all my friends whom are an important part of my life. My longtime friends from childhood and school, Giannis, Michalis, George, Jack, Lopas, Alex, Nikos, Dim Paz and especially Anna who was also my housemate and a co-passenger to my journey. Many thanks to my close friends Marianna, Spiros, Jo, Vas and my buddies Kostas, Dimitris, Anastasis, Giannis, Panos and Labros. Guys thank you so much for the

summer vacations and the Saturday coffee time. I would also like to thank all my friends that live abroad and especially Kon, Themo and Toni for the remote support and the great time we share together in Athens. Last one but not least, I owe special thanks to Chara for encouraging me all these years. She has affected my life in many different ways.

Finally, I am more than thankful to my family, my dad Giannis, my sister Maih, my grandmother Stasa and of course my missing mom Efi, for their love and support.

Declaration

I hereby declare that the contents of this dissertation are original and have not been submitted in whole or in part for consideration for any other degree or qualification in this, or any other university. This dissertation is my own work, except where specific reference is made to a joint effort in the text and Acknowledgements accordingly.

I grant powers of discretion to the University Librarian to allow the thesis to be copied in whole or in part without further reference to me. This permission covers only single copies made for study purposes, subject to normal conditions of acknowledgement.

London, October 2020

Stavros Rafail Fostiropoulos

Abstract

The current work investigates the breakup of a single emulsion droplet under pressure and temperature conditions realized in Diesel engine at the time of injection. The heating of immiscible heavy fuel oil-water droplets, termed as W/HFO emulsions, leads to explosive boiling of the water inside the surrounding fuel, due to their different boiling points; the resulting accelerated droplet breakup regimes are termed as either puffing or micro-explosion. The relevant processes are investigated here by numerical simulations based on the solution of the Navier-Stokes equations alongside with the energy conservation equation and transport equation of the formed interfaces using the Volume of Fluid (VoF) method. In contrast to past studies, which predefine the presence of vapor bubble inside the parent HFO droplet, this is modeled here with the aid of a phenomenological model based on the local temperature field and degree of superheat. Following their formation, the growth rate of the bubble is computed with the aid of the OCASIMAT phase-change algorithm. Simultaneously to internal boiling, the fuel droplet is also subjected to aerodynamic-induced deformation due to the surrounding air flow. Thus, the performed simulations quantify the relative time scales of the aerodynamic-induced and the emulsion-induced breakup mechanisms. Initially, a benchmark case demonstrates the detailed mechanisms taking place, concluding that droplet fragmentation occurs only at a part of the fuel-gas interface, resembling characteristics similar to puffing. Next, a parametric study examining the effect of droplet Weber number is performed for both W/HFO emulsion and neat HFO droplets. It is observed that puffing process can speed up the breakup of the droplet relative to aerodynamic breakup for the specific range of conditions examined. As a next step, this model is further applied to a wide range of pressure, temperature, water droplet surface depth and Weber number. The obtained results from CFD model predictions are used to calibrate the parameters of a fitting model estimating the initiation breakup time of the W/HFO droplet emulsion with a single embedded water droplet. The model assumes that the breakup time can be split in two distinct temporal stages. The first one is defined by the time needed for the

embedded water droplet to heat up and reach a predefined superheat temperature and a vapor bubble to form; while the succeeding stage accounts for the time period of vapor bubble growth, leading eventually to emulsion droplet break up. It is found that the fitting parameters are $\pm 10\%$ accurate in the examined range of conditions.

Thesis Contribution

- 1. Development of CFD methodology able to predict simultaneously the water vapor formation and growth inside the HFO droplet and the aerodynamic-induced deformation:** The incompressible form of the laminar N-S equations are solved for all phases present (HFO, water liquid/vapor and air) simultaneously with the energy conservation equation and three sets of transport equations utilised for simulating the HFO/air, HFO/water and water liquid-vapor interfaces forming during the droplet heating and breakup. This methodology is the first of their kind to be reported in literature and have been published in [1]
- 2. Physical models:** Moreover, and unlike previous studies, the vapor nucleation sites are not predefined, but they are predicted as part of the solution, based on the local liquid temperature. The examined properties are similar to that of a highly viscous Heavy Fuel Oil (HFO), which is typically used in large marine Diesel engines. As aforementioned, homogeneous nucleation occurs when a tiny vapor nucleus is generated inside a uniform liquid. Emulsion experiments have shown that the probability of vapor nucleation is related to the temperature of the liquid, while the vapor nuclei are generated close to the water interface [2, 3]. Since it is difficult to resolve the vapor nucleation phenomenon, a mechanistic algorithm that accounts for the initial formation of a small vapor bubble and takes into account the aforementioned experimental findings, has been developed and implemented into the CFD code. The growth of the vapor bubble is simulated with a phase-change model derived by [4]; the corresponding algorithm is incorporated in the CFD solution.
- 3. Estimation of the breakup time of W/HFO emulsion droplets under a wide range of pressure and temperature conditions realized in marine Diesel engines:** The CFD model has been applied to a wide range of conditions; namely

We and $p - T$ values ($40 < We < 200$, $10 < p < 140$ bar, $600 < T < 2000$ K). From the numerical simulations, two distinct timescales are estimated; the heating time until water boiling initiation and the bubble growth time starting from vapor bubble generation until HFO droplet breakup. Those results are used to derive a simple fitting model that is capable of predicting emulsion breakup initiation time. The latter is suitable for implementation to widely used fuel spray simulation codes utilizing the Eulerian-Lagrangian approach for resolving the development of sprays consisting of multi-million droplets. Such cases have not been reported before in the relevant literature; the relevant results have been published in [5].

- 4. New physical findings:** For low We numbers ($We < 50$), predictions suggest that the emulsion-induced breakup initiation time is at least 5 times faster compared to the time required for the aerodynamic-induced breakup under the same $P - T$ conditions and for the specific HFO physical properties. Moreover, the breakup initiation time was found to increase with the surface depth of the embedded water droplets at least for the examined range of δ ($0 - 0.15$), while its minimum values are obtained for high $p - T$ values.

Nomenclature

Roman symbols

Symbol	Description	Unit
a	Thermal diffusivity	m^2s^{-1}
A	Interfacial surface area	m^2
β	Scriven bubble growth factor	-
c_p	isobaric heat capacity	$\text{J kg}^{-1} \text{K}^{-1}$
d	Distance	m
D	Diameter	m
E	Energy	J
f	Physical variable	-
g	Correction factor	-
h_{lv}	heat of vaporization	J kg^{-1}
Ja	Jakob number ($\rho_w c_{p,w} \Delta T_s / \rho_v h_{lv}$)	-
k	thermal conductivity	$\text{W m}^{-1} \text{K}^{-1}$
m	mass	kg
Oh	Ohnesorge number ($\mu_f / \sqrt{\rho_f \sigma D_f}$)	-
p	pressure	Pa
Pe_f	Fuel Peclet number ($D_f u_f / a$)	-
R	radius	m
Re	Reynolds number ($\rho_g u_g D_f / \mu_g$)	-
St	Stefan number ($c_{p,w} \Delta T_s / h_{lv}$)	-
t	Time	s
T	temperature	K
u	Velocity	ms^{-1}
V	Volume	m^3
We	Weber number ($\rho_g u_g^2 D_f / \sigma$)	-

Greek symbols

Symbol	Description	Unit
α	Volume fraction	-
ΔT_s	Superheat degree	K
ε	Density ratio	-
μ	Dynamic viscosity	Pa s
ρ	density	kg m ⁻³
σ	Surface tension	N m ⁻¹

Superscripts and Subscripts

Symbol	Description
*	Non-dimensional
∞	far-field quantity
0	initial value
b	bubble
br	breakup
c	critical
CFD	values provided by CFD
dr	water sub-droplet
g	gas
i	interface
l	liquid
m	mass-averaged
oil	Oil phase/droplet
q	phase number
s	surface
sat	saturated
sh	Shear
v	Vapor
w	water

Abbreviations

Symbol	Description
CFD	Computational Fluid Dynamics
CpR	Cells per Radius
DNS	Direct Numerical Simulation
EV	Electric vehicles
FIE	Fuel Injection Equipment
FV	Finite Volume
HFO	Heavy Fuel Oil
IC	Internal Combustion
LS	Level-Set
NS	Navier-Stokes
SGS	Sub-Grid-Scale
VOF	Volume of Fluid
CLSVOF	Coupled Level-Set VOF
CSS	Continuum Surface Stress
UDF	User-Defined Function

Chapter 1

Introduction

1.1 Background and Motivation

Over the next two decades and despite the increasing fraction of electric vehicles (EVs) (they are expected to reach 60% in passenger car and light duty vehicles and up to 15% for heavy duty over the next two decades [6, 7]), it is expected that the usage of liquid fossil fuel will get increased by 25% globally, while the demand of liquid fuels just for heavy-duty vehicles will increase more than 50% [8]. The latter projections are the outcome of an increasing global energy demand (it is projected to be more than double by 2050) due to increasing global energy needs, urbanisation and population growth [9]. Internal combustion (IC) engines are massively used as a source of power, especially for transportation, due to their relatively high power output, the highest thermodynamic and highest well-to-wheel efficiency and finally low fuel cost [10]; however, electrification in this transport/power sector is expected to be a long-term process. Combustion products from IC engines, especially, NO_x and particulate matter (PM), are known to be harmful to both the environment and directly to human health when inhaled. According to [11], anthropogenic emissions contribute more than 90% to the climate change while Diesel engines are responsible for $\sim 2/3$ of the total liquid fossil fuel utilization globally. Besides the environmental impact, lung cancer, asthma and cardiovascular diseases are linked to such emissions. The aforementioned concerns have triggered many research efforts investigating mechanisms for reducing the in-cylinder formed pollutants in heavy duty and marine Diesel engines [12, 13]; among them, water in fuel emulsion is known to offer significant simultaneous reduction in NO_x and PM emissions. Reduction in NO_x is succeeded with the vaporization of the liquid water which in turns decreases the peak flame temperature during the combustion [14, 15]. On the other hand, reduction in PM emissions is related to i) the presence of water which reduces the soot formation and

enhance their burnout due to the increased concentration of oxidation species [16], ii) enhanced fuel-air mixing and secondary atomization due to micro-explosion process [17, 18].

Despite the potential benefit of using emulsified fuel, the advantage of the latter compared to its base fuel is not precisely known. This lack of understanding lies in the complex behavior of the emulsion fuel when it is injected in internal combustion engine, where the following multi-phase processes occur (**Figure 1-1**). First, cavitation phenomena are possible to arise inside the nozzle which may affect the atomization of the fuel liquid. Inside the combustion chamber, primary atomization initially occurs, where the emulsion fuel ligaments are disintegrated into droplets due to their interaction with the ambient air. Next, the emulsion fuel droplets are both subjected to aerodynamic deformation and heating with the hot surrounding air, resulting in their further breakdown (secondary atomization) which in turns causes fast fuel evaporation and improved air-fuel mixing. A detailed description of the breakup process will be provided in a following subsection.

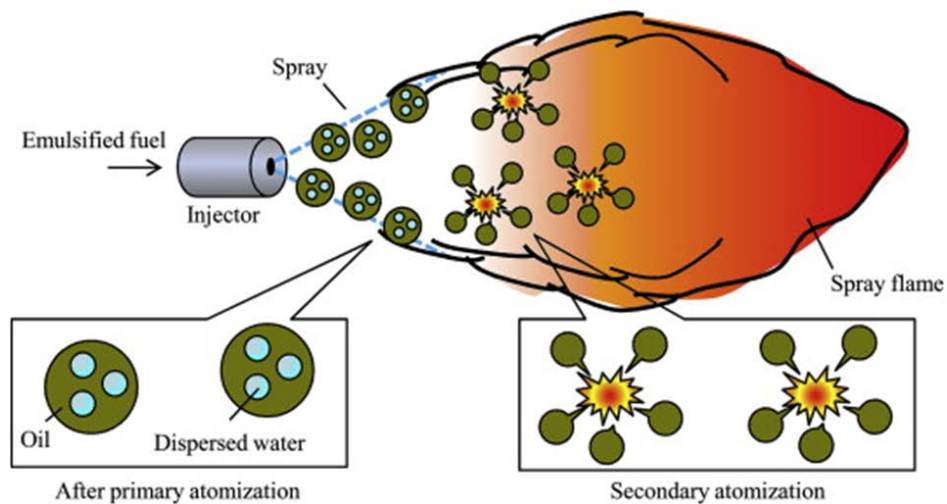


Figure 1-1: Schematic diagram of emulsion fuel spray.

The process from emulsion fuel injection up to breakup and combustion occurs in different time and length scales, thus it is impossible to get resolved by direct numerical simulations (DNS). The current work focuses on the breakup of an emulsion fuel droplet and its influencing parameters; this is a crucial step for the understanding of emulsion fuel spray behavior.

1.1.1 Addition of water in combustion process

Besides water in fuel emulsion, water can be introduced to the engine by in-cylinder injection (direct) and fumigation (water injection into the intake air) [19] (**Figure 1-2**). The main advantage of the former method is the capability to control the injection of large quantities of water without the need to derate the engine and affecting its reliability. This method has found to achieve NO_x reductions similar to those in emulsion systems, the reduction in PM emissions is much lower though. Moreover, direct water injection systems demand significant modifications for different types of engines, which has high additional cost [20]. On the other hand, fumigation is the simplest method of water addition. The fact that it offers limited control on the injection parameters results in lower NO_x reductions (10% for 20% water inside the fuel [21]) compared to the other methods. If the fumigated water does not completely evaporate in the intake air it comes in direct contact with fuel injection system and the piston cylinder which may cause oil contamination and corrosion issues.

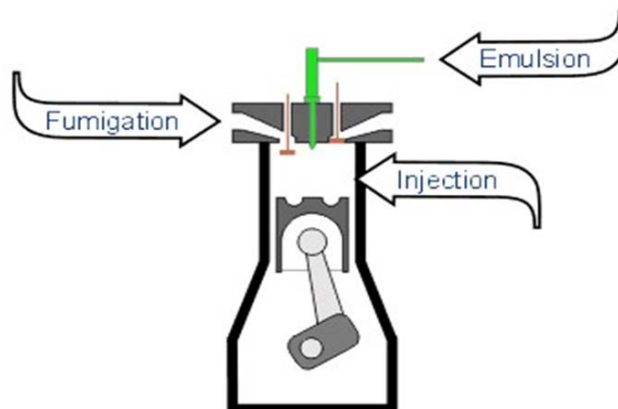


Figure 1-2: Water addition methods.

Finally, logistics of water supply is also a significant factor. Emulsion products can remain stable for a number of days or weeks, allowing vehicles to get fueled in place of regular fuel [22]. Considering the aforementioned, it seems that the most promising and cost-effective approach to utilise water for reduction of emissions is considered to be the water in oil emulsion method [23, 24].

1.1.2 Breakup of water in fuel emulsion

Emulsion is a system that consists of two immiscible liquids one of which is dispersed into the other. In the water/fuel emulsion, water is dispersed in the form of fine droplets inside the fuel liquid. Emulsion is generated by means of mechanical agitation in the presence of surface active agents, called surfactants or emulsifiers. The latter are needed in order to avoid the coalescence of the water sub-droplets. Surfactants can be easily burnt with no soot and free of sulfur and nitrogen, while they are not expected to have an impact on the physical and chemical properties of the fuel used. When an emulsified droplet is located inside a combustion chamber, heat is transferred from the hot ambient air to the emulsified droplet. The host (parent) droplet has higher boiling point than the corresponding one of the water sub-droplet; the water sub-droplet becomes superheated and eventually boils. The water droplet is contained in a uniform substance (oil droplet) free of nucleation sites and for that reason it is capable of exceeding its boiling point and experiences a metastable regime. At some point though, as the droplet heats up and the local temperature exceeds the boiling point of water, homogeneous nucleation occurs (in contrast to heterogeneous boiling which occurs when a fluid is in contact with solid surfaces) and water starts to boil [25]. Vapor generation leads to expansion and deformation of the surrounding oil droplet and eventually leads to its fragmentation. The process during which complete breakup of the oil droplet occurs is defined as micro-explosion, while if just a portion of the oil droplet is ruptured, the process is termed as puffing. A schematic representation of the micro-explosion process is illustrated in **Figure 1-3**. The aforementioned breakup regimes have been widely discussed in the literature, see selectively [24, 26, 27].

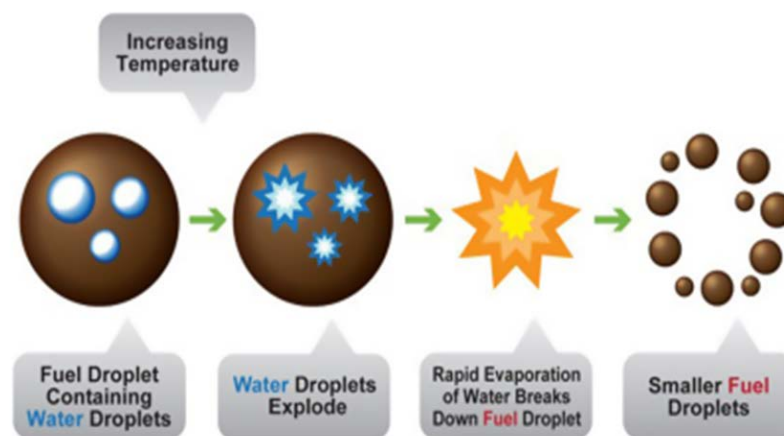


Figure 1-3: Micro-explosion of water in fuel emulsion droplet.

1.2 Literature review

An extensive literature review, on the current topic, is presented in order not only to record past works but also to find and pinpoint existing gaps and possible advancements.

1.2.1 Boiling heat transfer-Vapor bubble growth

A significant physical process that drives puffing or micro-explosion of emulsion droplets is the boiling of their embedded water droplets. Some important questions are the duration of the boiling process, the vapor behavior inside the water droplet and the effect of the boiling water sub-droplet on the surrounding fuel bulk. To answer those questions, it's important to grasp first the behavior of a single superheated water droplet.

The study of growing bubbles started with the simpler consideration of a stationary vapor bubble growing inside an infinite superheated liquid pool. The factors that influence the growth rates of those bubbles have been extensively studied over the last 50 years. In general, density fluctuations and disturbances are always present in liquids and are responsible for the formation of bubble nuclei. Nano or sub- μm vapor bubble nuclei collapse and disappear due to Laplace pressure in an accelerated manner; however, some of them may pass a critical radius ($R_0 = 2\sigma/\Delta P_0$) and continue to grow. The aforementioned expression must be couched in terms of the probability that a bubble with R_0 will occur at the time where a critical pressure difference ΔP_0 is applied. According to [28], liquids are able to withstand pressure differences of $3 \cdot 10^4$ to $3 \cdot 10^5$ bar, which correspond to a critical bubble radius comparable to the intermolecular distance (10^{-10}m). Since the vapor bubble has passed its critical radius, it continues growing in three different phases. The first growth phase is surface tension dominated where the pressure difference is balanced by the surface tension, while the bubble has the same temperature as the surrounding liquid. That regime diminishes quickly as the bubble size increases. Next, the bubble growth is limited by the inertia of the surrounding liquid and the bubble radius is a linear function of time. The bubble continues expanding, while its surface temperature decreases due to evaporation. The internal bubble pressure decreases until the driving force due to pressure difference is negligible. The final phase of growth is "diffusion" controlled, where bubble surface temperature will reach the bulk

saturation temperature, and the growth is limited by heat diffusion. At this regime, the growth rate of bubble decreases substantially; the bubble radius R increases with \sqrt{t} instead of t . The pressure and temperature field at each growing phase is illustrated in **Figure 1-4** derived by [29].

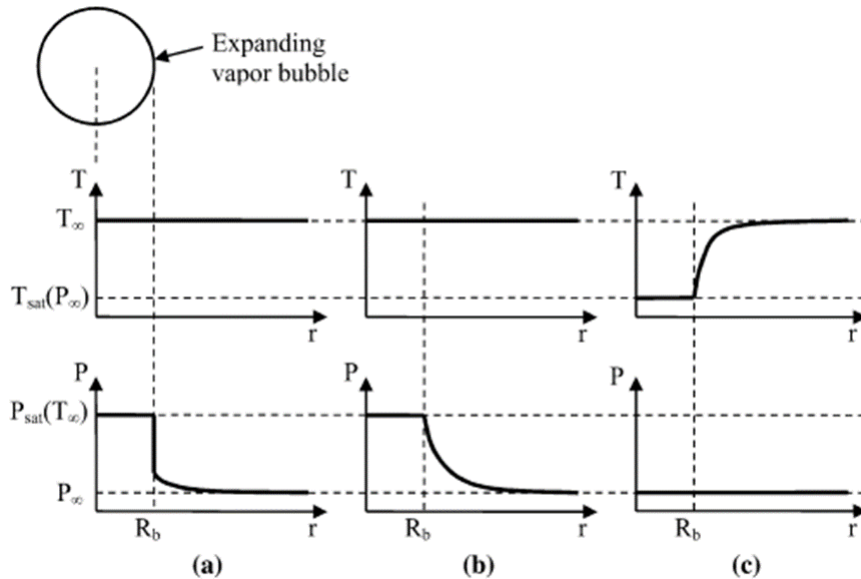


Figure 1-4: Pressure and temperature field inside and outside of the vapor bubble for surface tension (a), inertia (b) and heat diffusion (c) growth phases.

The aforementioned regimes can be dominant at different times and under different conditions and affect the vapor bubble behavior. The latter can be modelled during all those stages only with numerical simulations. In the open literature there is a significant amount of numerical studies dealing with vapor bubble growth. One of the first was by [30], who applied the heatflows model for estimating the interfacial mass transfer rate, while they employed VoF method for liquid-vapor interface tracking. Similar studies have been carried out by [31] and [32] who employed Level Set (LS) and Front Tracking (FT) methods, respectively. The same model was employed in the work of [33], who employed interpolation methods to compute accurately the temperature gradient at the interface. A different approach was followed by [34, 35], who employed a kinetic theory model which depends on a thermal accommodation coefficient defined by experiments. All these studies are validated against analytical solutions just for a small range of boiling conditions (St, ϕ). Those solutions have been developed in the past and predict accurately vapor bubble growth in either inertial or diffusive regime. The most significant of them are summarized next

1.2.1.1 Rayleigh model

The bubble growth model derived by [36] is based on the consideration of increasing pressure in bubble interior due to inertial forces imposed on the bubble interface by the surrounding liquid. The kinetic energy of the latter equalized with the pressure work by the expanding bubble provides a second-order differential equation that predicts bubble size with time and reads

$$R\ddot{R} + \frac{3}{2}\dot{R}^2 = \frac{\Delta p(t)}{\rho_l} \quad (1-1)$$

$\Delta p(t)$ stands for the pressure difference between the liquid on the bubble interface and the far-field pressure. By substituting the Clausius-Clayperon relationship which relates saturation pressure with temperature, and after some handling in Eq. 1-1 the bubble radius reads

$$R(t) = \sqrt{\frac{2\rho_v h_{lv} \theta_0}{3\rho_l T}} t \quad (1-2)$$

Here, θ_0 is the interface superheat which is assumed to be constant and equal to bulk superheat. This assumption is valid only for the inertial-dominated regime.

1.2.1.2 Foster and Zuber model

In the model of [37], a transient heat conduction equation in the liquid boundary alongside with heat and mass balance at the bubble interface are employed to obtain a second order differential equation of radius in time.

$$\rho_l \left(R\ddot{R} + \frac{3}{2}\dot{R}^2 \right) = \frac{2\sigma}{R_0} \left(1 - \frac{C_1}{(\pi a)^{1/2} Ja} \right) - \frac{2\sigma}{R} \quad (1-3)$$

Here, C_1 is a constant that depends on various assumption on the heating mode. The solution to Eq. 1-3 yields

$$R(t) = Ja(\pi a t)^{1/2} \quad (1-4)$$

1.2.1.3 Plesset and Zwick model

Similar to the model of [37], Plesset and Zwick [38] applied a perturbation theory solution to heat diffusion equation across the bubble's boundary layer. From the asymptotic growth assumption, the equation of bubble radius with time reads

$$R(t) = Ja \left(\frac{12at}{\pi} \right)^{1/2} \quad (1-5)$$

1.2.1.4 Scriven model

The Scriven [39] analytical solution considers a transient heat conduction equation inside the thermal boundary layer of the bubble. The solution accounts for the convection arising due to different liquid-vapor densities and also the diffusion effects as in the previous models. A similarity solution is obtained here which reads

$$R(t) = 2\beta\sqrt{a_l t} \quad (1-6)$$

More details about the constant β will be provided later in the text.

1.2.1.5 Mikic model

In the work of [40], a solution is obtained that combines the works of [36] and [41] and manages to predict successfully the bubble growth rate in both inertial and diffusion dominated regimes.

$$\frac{dR^+}{dt^+} = \sqrt{t^+ + 1} - \sqrt{t^+} \quad \text{with} \quad R^+ = \frac{AR}{B^2}, \quad t^+ = \frac{A^2 t}{B^2} \quad (1-7)$$

where the constants A and B read

$$A = \sqrt{\frac{2h_{lv}\rho_v(T_\infty - T_{sat})}{3\rho_l T_{sat}}}, \quad B = Ja \sqrt{\frac{12h_{lv}}{\pi}} \quad (1-8)$$

In the inertial regime ($t^+ \ll 1$), Eq. 1-7 reduces to Rayleigh solution while for the heat diffusion regime ($t^+ \ll 1$) it simplifies to Plesset-Zwick relation.

1.2.2 Emulsion fuel droplet breakup (Puffing/Micro-explosion)

1.2.2.1 Single emulsion droplet experiments

Despite the potential benefit of using emulsified fuels, the detailed physical mechanisms that occur during micro-explosion and puffing are not clear. In the experimental work of [42], homogeneous explosive boiling of a vapor bubble inside a superheated water droplet has been studied and the size of the vapor bubble during its growth was measured. In a similar experiment by [43], it was observed that during explosive boiling, liquid particles were torn from the liquid-air interface, alongside with bubble oscillations. So far, the majority of experiments on emulsion droplets has focused on the combustion characteristics after the puffing/micro-explosion induced secondary atomisation [44-46]; In the work of [44], the combustion characteristics of a water in Diesel emulsion, and a conventional Diesel fuel were investigated. Optical methods were employed to study spray development and combustion. Breakup time, droplets penetration and vapor penetration were measured with high speed shadowgraphs. Overall, enhanced atomization was observed for the water in Diesel emulsions compared to that of base fuel. In a similar experiment of [45], the benefits of emulsified fuels over the neat ones were investigated. Spray characteristics such as spray penetration and distribution were measured. In such experiments though, the overall dynamics of a single droplet cannot be revealed.

In single droplet experiments, a relative large droplet ($O(1\text{ mm})$) compared to those realized in engines has been investigated. In the work of [47] it was found that the water volume fraction and the quantity of surfactant may influence the tendency towards micro-explosion. The latter can also be affected by the size distribution of the dispersed water sub-droplets [48]. In the work of [49], the suspended droplet technique was employed to investigate a stationary emulsion droplet (water in hexadecane) subjected to heating under microgravity. It was observed that the embedded water sub-droplets tend to coalesce prior to micro-explosion, in some cases. Thermocapillary migration of the embedded water droplets and subsequent phase separation has also been observed in the work of [50, 51]. The occurrence of micro-explosion was measured in the experiment of [52]. It was found that the former is highly related to a number of parameters, namely, the dispersed water size, the heating temperature and the thermophysical properties of the fluids examined. In the recent experiment of [53], high speed backlight imaging was used to study the dynamics of puffing and micro-explosion

in Diesel fueled emulsions. The latter were placed into a high temperature environment (500° C) and two types of micro-explosion were observed, which differ mainly to the amount of vapor expulsion and as a result to the intensity of breakup. Significant factors that may affect the emulsion breakup outcome were found to be the water volume fraction [54], the quantity of surfactant [55] and the size distribution [56] of the water sub-droplets. In the works of [57, 58] the breakup outcome of a water-fuel droplet subjected to conductive, convective and radiation heating was investigated. In the recent work of [59] characterization of breakup of an emulsion droplet was reported while the characterization of size, temperature and location of embedded water droplets was investigated by [60] during micro explosions. Finally, in the work of [61], a phenomenological description of the vaporization process during emulsion droplet heating is reported. Besides the droplets employed in the aforementioned studies are relatively large, they remain stationary and they are not subjected to aerodynamic deformation as those droplets met in fuel sprays

Recently, single droplet experiments having sizes similar to those realised in CI engines (O (10 μm)), were performed by [62, 63]. In the experiment of [63], a high speed video camera coupled with a shadow imaging technique was used to visualize secondary atomization of emulsified fuel spray. The breakup regime mostly observed was puffing (**Figure 1-5**) while micro-explosion rarely observed due to the small amount of the dispersed water and the low progression of coalescence. Puffing-induced secondary atomization was found capable to provide fine droplets while its timescale measured equal to $\sim 10 \mu\text{s}$. However, in both experiments, the physical processes taking place inside the emulsion and during the growth rate of the boiling water have not been revealed.

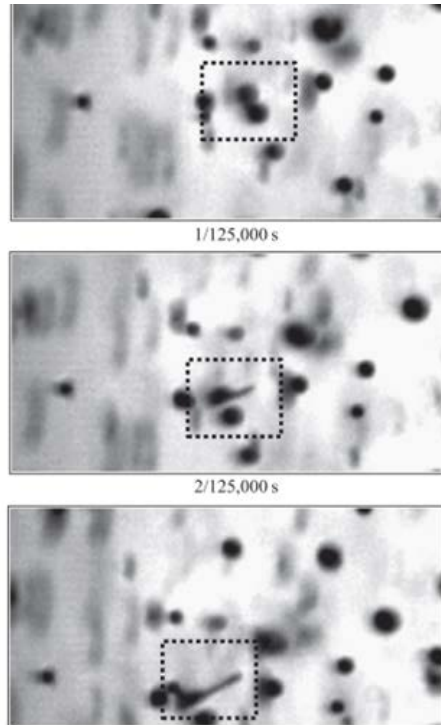


Figure 1-5: Puffing of a spray emulsion droplet with diameter $d = 50 \mu\text{m}$

1.2.2.2 Theoretical models

The development of micro-explosion models could shed light on the phenomenon. One of the first relevant mathematical models is that of [64], which predicts vapor bubble growth, produced by homogeneous nucleation, within a liquid water droplet. Besides the simplifications considered, the results of the model are in good agreement with that derived by the experiment of [65]. However, puffing/micro-explosion phenomenon was not taken into account. A similar approach was followed by [66], who employed Rayleigh's model to predict vapor bubble growth in the centre of a liquid water droplet; however, the assumptions made in that model may not be suitable for engine fuel spray conditions. Secondary droplet size distribution is predicted in the models of [67, 68].

Simplified mathematical models which can be useful for engineering applications have recently been suggested [69-73]. In the model of [69], the number and the average diameter of child droplets is predicted after emulsion droplet breakup. The model derived by [72] assumes that a single spherical water droplet is located at the center of a spherical fuel droplet. An analytical solution is obtained by solving the heat conduction equation, and predicts the time instant that the water droplet interface reaches boiling temperature; this is considered to be the time to puffing or micro-explosion. The model

is helpful for engineering application but it cannot provide details of the physical processes during deformation and breakup of emulsion droplet.

Finally, advanced computational fluid dynamics (CFD) models proposed recently by [26, 27] gave insight on the underlying physics of micro-explosion and puffing. In the work of [26], simulations of a static emulsion droplet have been performed where the latter is considered to be preheated in the boiling temperature of its embedded water sub-droplet. Besides the predefined temperature, the location and size of the vapor bubble were also predefined. Convective heating of emulsion droplets has been studied in [27]; the model predictions indicated that the boiling of the embedded water sub-droplet highly depends on the liquid Peclet number and the internal circulation inside the parent droplet. Weber (We) and Ohnesorge (Oh) numbers (i.e it is controlled by inertia, surface tension and viscous forces) are the most significant ones, while Reynolds number and the liquid to air density (ε) and viscosity (N) ratios [74] play a secondary role.

1.2.3 Aerodynamic breakup of neat fuel droplet

Similar to neat fuel droplets, emulsion fuel droplets that are met in spray conditions are subjected to aerodynamic forcing. In a fuel spray, the relative velocity between the air stream and the fuel droplet generates aerodynamic forces that are responsible for the deformation of the latter. Aerodynamic-induced deformation is balanced by forces induced by fuel properties such as viscosity and surface tension. Secondary droplet breakup due to aerodynamic forcing is mainly characterized by the Weber (We) and Ohnesorge (Oh) numbers (i.e it is controlled by inertia, surface tension and viscous forces), while Reynolds number (Re) and the liquid to air density (ε) and viscosity (N) ratios [74] play a secondary role

$$\begin{aligned}
 We &= \frac{\rho_g u_g^2 D_0}{\sigma} & Oh &= \frac{\mu_l}{\sqrt{\rho_{oil} \sigma D_{oil}}} & Re &= \frac{\rho_g u_g D_0}{\mu_g} \\
 \varepsilon &= \frac{\rho_l}{\rho_g} & N &= \frac{\mu_l}{\mu_g}
 \end{aligned} \tag{1-9}$$

Breakup results in droplet fragmentation into several tiny droplets and requires a finite time for this to be completed, of the order of the shear breakup timescale [75] which reads

$$t_{sh} = \frac{D_0\sqrt{\varepsilon}}{u_g} \quad (1-10)$$

1.3 Thesis outline

Chapter 2: The mathematical description of the emulsion droplet breakup model is presented alongside with that of the models that account for vapor bubble generation and growth.

Chapter 3: Model performance on predicting accurately vapor bubble growth and droplet oscillation. Model validation for the simple case of stationary emulsion droplet breakup.

Chapter 4: Examined cases and results of 2-D axisymmetric simulations of HFO emulsions, realized in fuel sprays, are presented.

Chapter 5: A mathematical description of a fitting model, that predicts emulsion fuel droplet breakup time is provided, alongside with a discussion on the results

Chapter 6: The main conclusions of the current thesis are presented along with suggestions for future work.

Chapter 2

Numerical models

2.1 Mathematical description of the model equations

Mathematical description of multiphase phenomena is far from trivial since a number of effects and interactions between the different fluid phases have to be taken into account. In the current study where DNS of emulsion droplet breakup is attempted, the direct tracking of the involved interfaces is essential. Such a process demands additional computational effort (which depends on the tracking method used), while the computational grid needs to be finer in the interface regions. The mathematical formulation of interface tracking is based on two assumptions [76]. Each interface has a finite thickness, which is the transition region of the corresponding fluid properties. Such an assumption is correct as long as the length scale of the interface is such that continuum hypothesis holds. Following the aforementioned assumption, the second principle is that the intermolecular forces that determine the interface dynamics are modeled in the

continuum scale as capillary effects. The interface tracking formulation is split in two different categories, namely the n-fluid formulation and the single fluid formulation. In the former approach a set of flow equations is solved for each different fluid in the corresponding sub-domain, while in single-fluid formulation a single set of flow equations is solved throughout the entire domain. In the latter category, the most known methods for identifying the interface between different fluid phases are the Front Tracking (FT) method, the Level-Set (LS) method and the Volume of Fluid (VoF) method. The VoF algorithm is described more extensively, as it is the one implemented in the current emulsion breakup model.

2.1.1 Fluid flow and Volume of Fluid

As it was mentioned before, the VoF method [77] solves a single set of momentum equations while it identifies each fluid phase by a volume fraction denoted by α . Specifically, in the emulsion model three phases initially exist (Air, Oil, Water) and at some point during the simulation an additional phase is solved due to sudden appearance of vapor. The volume fraction α is defined as the percentage of volume covered by each phase in the computational cell with respect to the total volume of the cell. In each cell the sum of the volume fractions of all phases must be equal to unity. Mathematically, when volume fraction of phase q inside a cell is unity, the cell is completely covered by the material of phase q , while when the volume fraction is equal to zero, the cell is empty of phase q .

$$\alpha_q = \frac{\text{cell volume occupied by fluid } q}{\text{total volume of cell}} \quad (2-1)$$

Finally, when the volume fraction of q^{th} fluid is between 0 and 1, the cell contains the interface between the q^{th} fluid and one or more other fluids. As the computational cell can be occupied by all involved fluids, the following equation is valid

$$\sum_{q=1}^N \alpha_q = 1 \quad (2-2)$$

Where N is the number of the involved fluid phases.

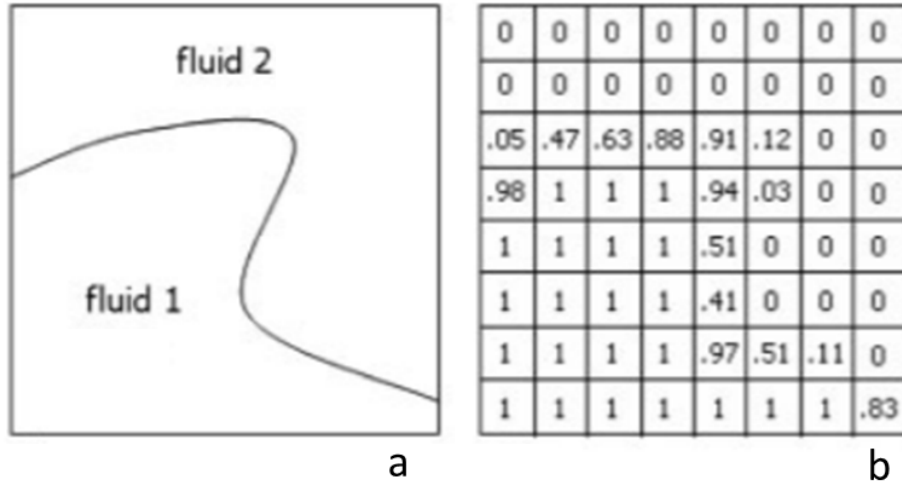


Figure 2-1: An interface between two fluids (a) and the corresponding volume fractions (b).
Derived by [78]

Upon the volume fraction value of phase q , variables and properties represent volume-averaged values of phase q . For instance, the physical variable f within a computational cell is computed as follows:

$$f = \sum_{q=1}^N a_q f_q \quad (2-3)$$

The advection equation for the volume fraction is defined as:

$$\frac{\partial a_q}{\partial t} + \nabla \cdot (\vec{u}_q a_q) = \frac{\dot{m}_{pq}}{\rho} \nabla a_q \quad (2-4)$$

The term in the right hand side (RHS) stands for any additional volumetric source term. Since a single momentum equation is solved throughout the entire domain, the computed velocity field is shared among all the involved phases. The momentum equation is dependent on the properties of density ρ and dynamic viscosity μ , which are computed according to Eq. 2-3 and it is written in the form

$$\frac{\partial(\rho \vec{u})}{\partial t} + \nabla \cdot (\rho \vec{u} \otimes \vec{u} - \vec{T}) = \rho \vec{g} - \vec{f}_\sigma \quad (2-5)$$

In the second term of the left hand side (LHS), \vec{T} stands for the stress tensor.

Surface tension term denoted as \vec{f}_σ is taken from [79] and for the case that only two phases are present inside a computational cell, the relation reads

$$\vec{f}_\sigma = \sigma_{pq} \frac{\rho \kappa_p \nabla a_p}{\frac{1}{2}(\rho_p + \rho_q)} \quad (2-6)$$

The two different fluid phases are denoted by p and q and k is the curvature of the free surface which is approximated as the divergence of the unit normal \hat{n} and reads

$$\kappa_p = \nabla \cdot \hat{n} \quad (2-7)$$

$$\hat{n} = \frac{\nabla a_p}{|\nabla a_q|} \quad (2-8)$$

The energy equation, which is also shared among the contributing phases, is presented in Eq. 2-9, where energy E is a mass-averaged variable between each additional phase.

$$\frac{\partial(\rho E)}{\partial t} + \nabla \cdot (\vec{u}(\rho E + p)) = \nabla \cdot (k \nabla T) + S_h \quad (2-9)$$

$$E = \frac{\sum_{q=1}^n \alpha_q \rho_q E_q}{\sum_{q=1}^n \alpha_q \rho_q} \quad (2-10)$$

In those equations above, density ρ and thermal conductivity denoted by k , are shared among the phases. Finally, S_h contains contributions from any volumetric heat sources existed in the model.

The equations described above are in a general form, while their solution is performed with the commercial software of ANSYS FLUENT [80]. The selected solution methods and numerical settings are presented in the following sections.

2.2 Vapor bubble formation model

Boiling of dispersed water droplets inside the fuel bulk is a key mechanism that drives puffing or micro-explosion of emulsion droplets. Since the current CFD methodology aims to simulate the phenomenon from emulsion heating up to secondary droplet fragmentation, the formation of vapor should be part of the numerical solution. As

nucleation theories aiming to resolve formation of vapor nuclei inside the bulk of the water are out of scope in the current thesis, a conceptual approach for vapor bubble formation is developed and implemented in the model.

The criteria, under which a vapor bubble is generated, are the following. First, the formation site, which is a computational cell (**Figure 2-2** ; left panel), should be located at a specific distance (d_i) from the oil-water interface [43]. This distance has a finite length preventing contact of the bubble with the oil-water interface (**Figure 2-2**; Right panel). In case that vapor, water and oil phases coincide in a computational cell, numerical issues arise. A relevant parametric study with bubble's surface depth is presented in subsection 4.2.2.4, proving that the obtained results are not sensitive to this numerical selection. Next, the superheat degree (ΔT_s) of vapor generation is also an input parameter of the model. The algorithm checks if the selected superheat degree has been reached in the aforementioned computational cell. Different superheat values from 5 to 25 K have been examined but the results seem not to be sensitive (subsection 4.2.2.4). Once the aforementioned criteria are fulfilled in a computational cell, a bubble is formed at the center of the computational cell. As discussed in the literature, the vapor bubble should reach a critical size ($R_0 = 2\sigma/\Delta P_0$) in order to start growing from a microscopic to a finite size. The first growth phase is inertia controlled, which ends quickly in order the diffusion controlled growth to follow. The transition to the diffusive regime is characterized by a critical bubble radius [40], which depends on fluid properties and liquid superheat; the relationship reads

$$R_c = 2\sigma T_{sat}/h_{lv}\rho_v\Delta T_s \quad (2-11)$$

In the examined cases of the current study the latter was computed to be 0.11 μm . As it's computationally expensive to resolve such a length scale, the vapor bubble is initiated with a finite radius size ($R_{b,0} = 0.25 \mu\text{m}$). It should be noted that the effect of the initial bubble radius has been checked by performing numerical experiments, pointing out that the breakup process is identical and only the early development of the bubble differs; similar behavior has been observed also in the work of [26]. Since the initial bubble starts growing due to heat diffusion, as it is larger than R_c , a bulk saturation temperature value is imposed at its interface, while its internal pressure is defined by the surface tension term ($2\sigma/R_{b,0}$).

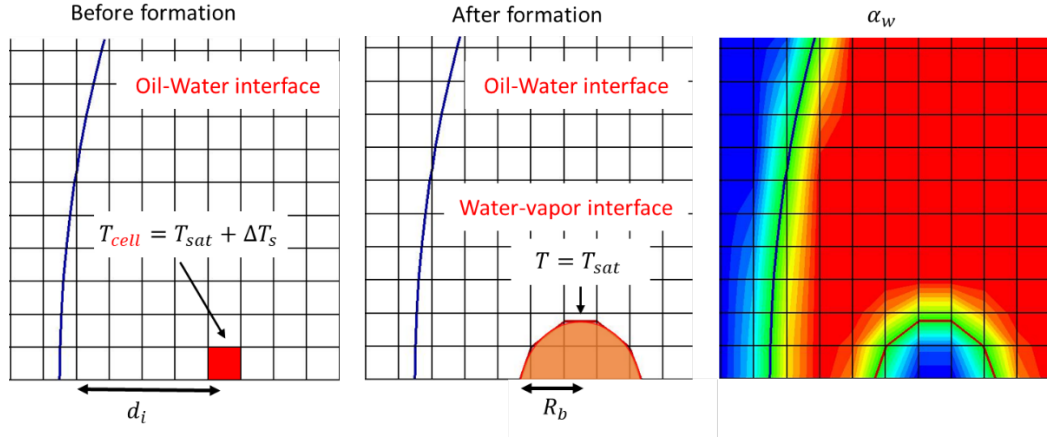


Figure 2-2: Configuration of vapor bubble formation

Summarizing, the criteria for bubble creation in a computational cell are the following:

- i) $T_{cell} \geq T_{sat} + \Delta T_s$, ii) d_i to be the smallest possible, without vapor water and oil coexisting in a computational cell (in the current resolution d_i is equal to $\sim 0.5 \mu\text{m}$).

2.3 Phase change model-OCASIMAT algorithm

Right after vapor bubble formation, the vapor bubble starts growing inside the water droplet due to interfacial heat and mass transfer. A method termed as OCASIMAT [4] is implemented in the CFD model and calculates the growth rate of the vapor bubble. A VoF equation for vapor volume fraction (α_v) tracks the vapor-water interface while the mass flux \dot{m}_{pq} in Eq. 2-4 recasts

$$\dot{m}_{lv} = \frac{(k_l \nabla T_l - k_v \nabla T_v) \cdot \vec{n}}{h_{lv}} \quad (2-12)$$

The above formulation stands for the case where mass transfer rate depends on the temperature gradient on both sides of the interface, since both sides could transfer heat to the interface or remove heat from the interface. In the examined case though, the vapor temperature remains saturated thus the temperature gradient at the vapor side can be neglected. Finally, eq. 2-12 recasts

$$\dot{m}_{lv} = \frac{k_l \nabla T_l \cdot \vec{n}}{h_{lv}} \quad (2-13)$$

where ∇T_l stands for the temperature gradient at the interface. The challenging task is the accurate calculation of the latter which results in proper estimation of the mass transfer rate. Moreover, a proper interface temperature value has to be imposed on the interface. The OCASIMAT algorithm determines the temperature gradient at the interface as follows.

- (1) The mixture cells where both water and vapor phases coexist are identified
- (2) The closest point from the mixture cell center on the interface (a) is located. The distance between those points is denoted as d_1 .
- (3) Identify the neighbor cell (G-cell) which is defined as the nearest cell to the interface in the normal direction.

- (4) The distance from G-cell center to point b normal to the interface is computed

A schematic representation of a mixture cell and the aforementioned procedure is illustrated in **Figure 2-3**.

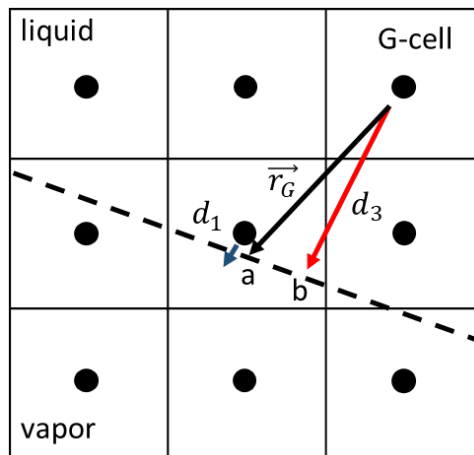


Figure 2-3: OCASIMAT one cell algorithm for the evaluation of temperature gradient at the interface

The aforementioned procedure provides the calculation of temperature gradients at points *a* and *b* of the interface

$$\nabla T_a = \frac{T_M - T_{sat}}{d_1} \quad (2-14)$$

$$\nabla T_b = \frac{T_G - T_{sat}}{d_3} \quad (2-15)$$

The temperature value at the mixture cell center, that needs to be fixed, is denoted with T_M , while the value at the neighbor cell, as defined by the CFD solution, is T_G . The temperature at the interface is considered to be the saturated one T_{sat} and its value depends on the fluid properties. For the estimation of mass transfer rate, temperature gradient ∇T_b is used which is replaced in Eq. 2-12. The correction at the mixture cell temperature is succeeded by assuming a linear temperature profile between the interface point a and G-cell center. This is considered a valid assumption as long as the grid is dense. By equalizing Eq. 2-14 with Eq. 2-15, the fixed temperature T_M reads

$$T_M = T_{sat} + d_1 \frac{(T_G - T_{sat})}{d_3} \quad (2-16)$$

That value should be introduced in the source term S_h of energy equation (Eq. 2-9) at the mixture cells. Normally, assignment of a value is allowed only at the boundary points. In order to overcome this obstacle and impose the temperature value of eq. 2-16 at the mixture cell, the large coefficient method introduced by [81] is used. The source term at the mixture cells reads

$$S_h = CT_M - CT_{i,j} \quad (2-17)$$

where a value equal to 10^{30} is imposed at the coefficient C . The latter is large enough that makes all the coefficients in the discretized energy equation negligible. Consequently, $T_{i,j}$ which is the temperature value at the mixture cell center predicted by the CFD solution becomes equal to T_M .

2.4 Local grid refinement

In order to save computational cost and the same time maintain high resolution at the area of interest, an adaptive local refinement method has been employed. The method has been derived by [82] and it has been expanded in the current work in order to be suitable for a multi-VoF code. According to the original technique, the mesh is dynamically refined at a prescribed distance from the interface. Numerically, the implementation of this technique is achieved by the following steps

- (i) Looping over all cells of the computational domain
- (ii) Identifying the iso-surface where volume fraction is 0.5

(iii) Looping over the cells as many times as the isovalue cells in order to find their distance from the interface.

As a last step, the cells that lie within the user-specified distance from the interface are marked for refinement. The distance should be relatively far from the interface, so that the VoF gradients and curvature always lie in the region with the smallest cells. The local refinement technique is repeated after a number of time-steps; that number is specified by the user so that the interface never exits the finest level of refinement cells. The modified model has the capability to perform refinement with respect to different variables simultaneously. Each time the algorithm performs the local grid refinement with respect to a variable, only the marked cells for refinement will be stored in a temporary memory location. The local grid refinement with respect to the rest of the chosen variables follows and the marked cells are stored every time. Finally, the superposition of the marked cells for refinement for each variable indicates the total local grid refinement. The performance of the modified algorithm is evaluated for an indicative case of two colliding droplets, where each droplet is tracked by a different VoF variable. thus refinement should be performed with respect to both of those. shows that local refinement is performed successfully.

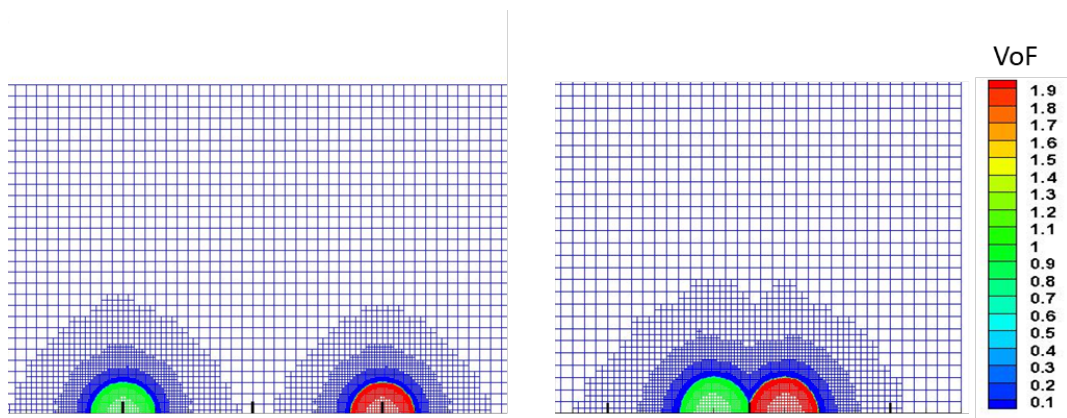


Figure 2-4: VoF values indicating the initial location (a) and collision (b) of two droplets

Chapter 3

Preliminary computational studies-Model validation

To the best of our knowledge, suitable data from single emulsion droplet experiments where droplet size is similar size to that realized in fuel sprays, are not available for comparison. The figures provided (**Figure 1-5**) in the work of [62, 63] could be used for qualitative comparison but they are rather unclear. Therefore, the model's first principles are validated against analytical solutions. The OCASIMAT phase change model is compared against Scriven [39] analytical solution. Air-oil interface of the emulsion droplet is expected to oscillate, thus nonlinear droplet oscillation is tested in a simple configuration and validated against numerical data derived by [83]. Besides the validation of the aforementioned key features, results of stationary emulsion droplet breakup are qualitatively compared against that of [26].

3.1 Vapor bubble growth inside an infinite liquid pool

3.1.1 Theoretical solution

Growth of a spherical bubble studies the parameters related to bubble interface curvature, namely the interface curvature, surface tension effects and mass transfer (**Figure 3-1**). In bubble growth, during a time period the mass of liquid evaporated into vapor is calculated by the mass flux (from liquid to vapor phase) and the surface area (A_s) of the bubble interface.

$$m = \dot{m}A_s dt \quad (3-1)$$

At the same time, the corresponding vapor mass (m) pushes the surface area of the bubble interface towards the liquid side thus the bubble increases.

$$m = \rho_v A_s dr \quad (3-2)$$

Combining the aforementioned equations and integrating in space and time, considering that bubble starts growing from an initial finite size R_0 , the theoretical expression for the bubble radius as function of time is derived and reads

$$R(t) = R_0 + \frac{\dot{m}}{\rho_v} t \quad (3-3)$$

For a bubble growing in non-adiabatic conditions, the mass flux depends on the temperature gradient at the interface which varies in time.

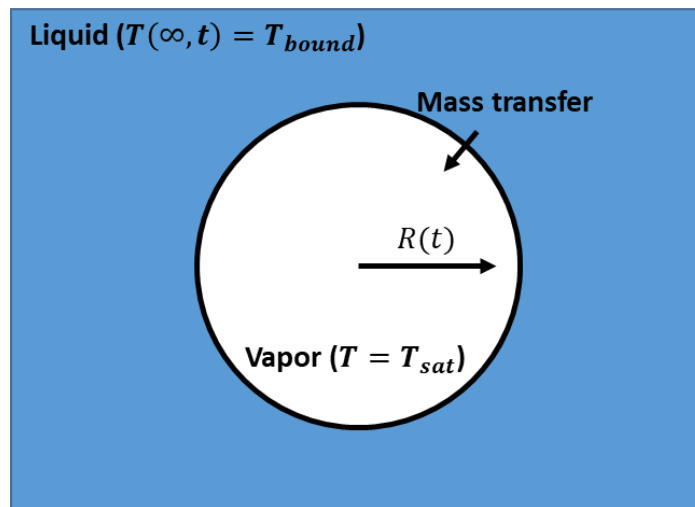


Figure 3-1: Schematic representation of spherical bubble growth

Scriven [39] predicted theoretically the growth of a spherical bubble in a uniform superheated liquid. The advection-diffusion equation is solved in spherical coordinates and a similarity variable is used. The model assumes that vapor phase remains saturated at a constant temperature value during bubble growth. Initially a small bubble exists inside a liquid pool, where its interface is saturated while liquid temperature is uniform and higher than the saturated one ($T(r, 0) = T_{bound}$). As time progresses and bubble increases, a thermal boundary layer (TBL) appears in the liquid side due to thermal interaction between the liquid and the bubble interface. The size of the thermal layer increases with time implying that the temperature gradient and subsequently the mass flux at the interface decrease. This is highlighted in Scriven's relationship (Eq. 1-6), which assumes that bubble radius increases with \sqrt{t} . The growth rate constant β in Eq. 1-6 is a dimensionless and its value depends on the superheat degree (ΔT_s) and the thermophysical properties of the material examined as shown in the following expression.

$$\beta = \sqrt{\frac{3}{\pi}} \left\{ \frac{\Delta T_s}{\left(\frac{\rho_v}{\rho_l} \right) \left[\frac{h_{lv}}{c_{p,l}} + \left(\frac{c_{p,l} - c_{p,v}}{c_{p,l}} \right) \Delta T_s \right]} \right\} \quad (3-4)$$

In β growth rate lies the non-dimensional Stefan number (St) which is defined as the ratio of sensible heat to latent heat of vaporization and reads

$$St = \frac{c_{p,l} \Delta T_s}{h_{lv}} \quad (3-5)$$

This number alongside with the liquid-vapor density ratio ($\varphi = \rho_l / \rho_v$) control the mass transfer rate during phase change from liquid to vapor phase.

Finally, the temperature distribution at the liquid side ($r > R$) and thus inside the TBL is obtained by the following relationship.

$$T(r, t) = T_{bound} - 2\beta^2 \left(\left(\frac{\rho_v}{\rho_l} \right) \left[\frac{h_{lv}}{c_{p,l}} + \left(\frac{c_{p,l} - c_{p,v}}{c_{p,l}} \right) \Delta T_s \right] \right) A_{int} \quad (3-6)$$

$$A_{int} = \int_{1-\frac{R}{r}}^1 e^{\left(-\beta^2 \left((1-\zeta)^{-2} - 2 \left(1 - \frac{\rho_v}{\rho_l} \right) \zeta - 1 \right) \right) d\zeta}$$

3.1.2 CFD simulations

3.1.2.1 Computational setup and examined conditions

Spherical bubble growth inside a superheated liquid pool is investigated with the aid of numerical simulations, and the OCASIMAT phase change algorithm is evaluated for this simple configuration. The flow equations are solved in an axisymmetric domain, where in the left vertical axis, symmetry boundary condition is imposed. All the rest boundaries are open, where velocity 1st gradient is set to zero.

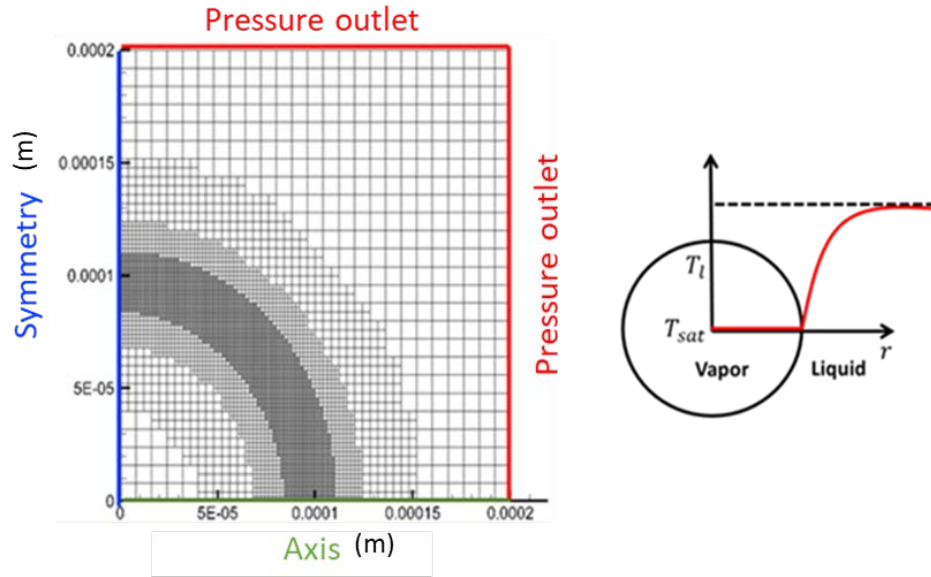


Figure 3-2: Computational mesh refined locally alongside with boundary conditions (Left panel). Schematic illustration of thermal boundary layer (Right panel).

The domain extends up to a distance of $2R_0$, which is the initial bubble radius size, in both vertical and horizontal directions; the same configuration has been employed in past studies [4, 33, 35, 84]. The adaptive local refinement method described in subsection 2.4 is implemented in order to save computational cost and maintain a sharp interface. In the specific case, mesh refinement is repeated every ten computational time-steps. From the Mikic relationship [40], it was computed that the transition to the diffusion controlled growth, in the current case, occurs when the bubble radius is equal to $6 \mu\text{m}$. Here, the simulation starts from an initial bubble radius R_0 equal to $100 \mu\text{m}$, where heat diffusion regime is already dominant. The temperature distribution $T(r, t)$ inside the thermal film, computed by Eq. 3-6 at the time instance where $R = R_0$, is initialized in the simulation. In the default simulation, the fluid properties examined here are that of water at atmospheric pressure, while the superheat degree is equal to 5 K. The latter value corresponds to an St number equal to 0.01. Both water and vapor properties are summarized in **Table 3.1** alongside with initial conditions of the simulation.

Property	Units	Water	
		Liquid	Vapor
Density ρ	kg m ⁻³	958	0.597
Specific heat capacity c_p	J kg ⁻¹ K ⁻¹	4220	2030
Thermal conductivity κ	W m ⁻¹ K ⁻¹	0.679	0.025
Dynamic viscosity μ	Pa s	277 10 ⁻⁶	1.3 10 ⁻⁵
Heat of vaporization h_{lv}	J kg ⁻¹	2.257 10 ⁶	
Surface tension σ	N m ⁻¹	0.059	
Saturation temperature T_{sat}	K	373	
Conditions			
Pressure p	bar	1.013	
Superheat dT_s	K	5	

Table 3.1: Initial conditions and material properties of the default numerical simulation

3.1.2.2 Results

Results derived from the default simulation are initially presented. The bubble evolution alongside with the temperature distribution on both phases at three different time instances are illustrated in **Figure 3-3**. A first glimpse shows that vapor phase remains saturated at 373 K, while the temperature at the liquid phase varies from the saturation temperature up to the superheated one (378 K). As the time progresses, the radius of the vapor bubble increases and the interface remains sharp (black line). The thermal boundary layer moves along with the interface due to convective transport while its thickness increases due to diffusive transport. At $t = 75 \mu\text{s}$, a slight deformation of the thermal boundary is observed near the boundaries; this is due to the fact that secondary effects of errors in normal vectors arise and as a results liquid velocity increases on these regions.

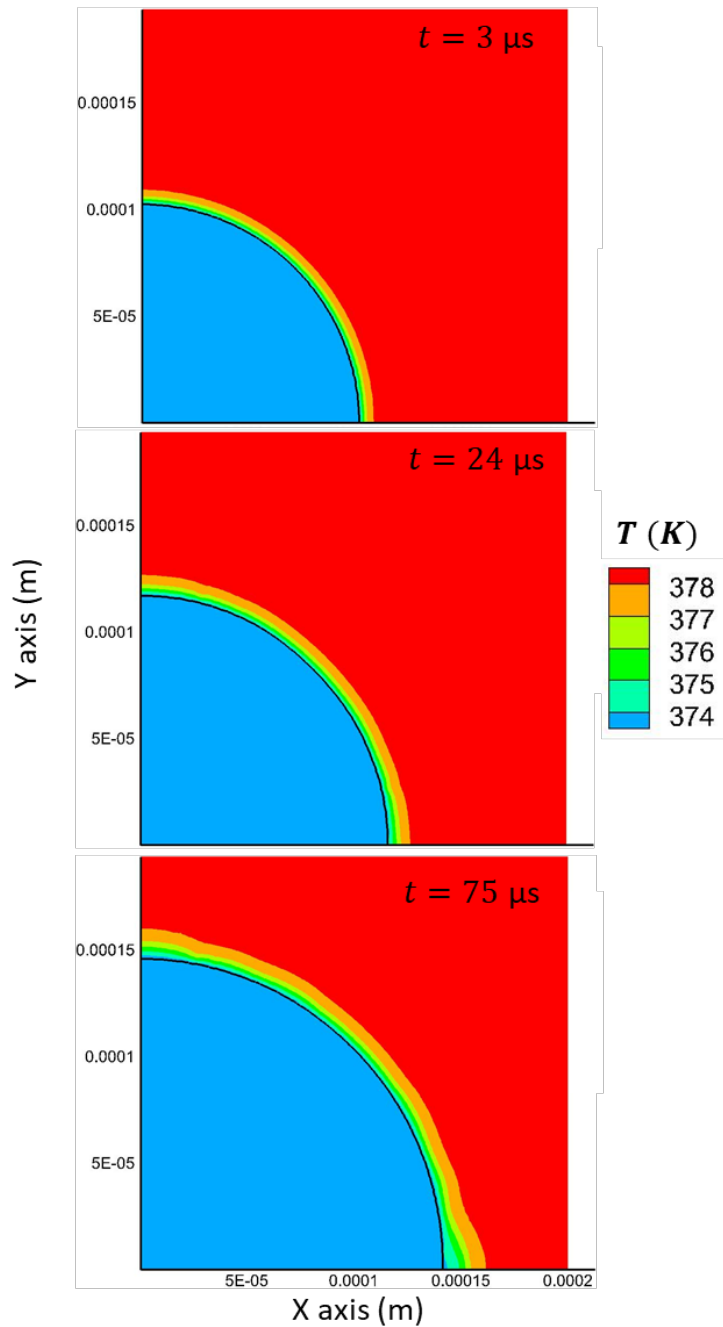


Figure 3-3: Temperature distribution during bubble growth at three time instances.

As already stated, high resolution is required in order to capture the boundary layer near the interface. A mesh independence study has been performed in order to retrieve the adequate mesh resolution that the boundary layer needs to get resolved and the results are compared against Scriven's analytical solution. For the CFD model to be in agreement with analytical solution, it was found out that the base grid resolution should be 10 CpR with 4 levels of refinement, corresponding to 160 CpR at the beginning of the

simulation. Results in **Figure 3-4** clearly indicate that the accuracy of the simulation improves with smaller mesh size. Specifically, for mesh size equal to $1\ \mu\text{m}$ (blue solid line), where the initial thickness of the boundary layer is computed equal to $12\ \mu\text{m}$, it is observed that the model results are in perfect agreement with that of the theoretical solution.

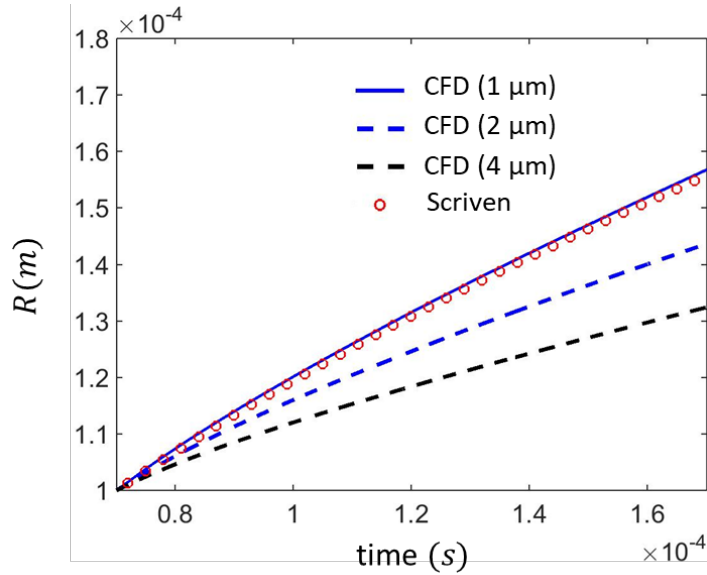


Figure 3-4: Prediction of the bubble growth rate for different grid resolutions

Next, a number of parametric cases was performed, in order to examine the model performance for different values of St number and density ratio. In order to estimate the declination of the CFD methodology from theory, a bubble growth constant (β_{CFD}) was derived for each parametric case and compared against the corresponding constant b of the analytical solution. The nondimensional error is expressed as $\beta - \beta_{CFD} / \beta_{CFD}$ and it seems significant for high Stefan numbers. The error decreases up to a point if mesh resolution becomes higher. In general, the emulsion droplets are examined for conditions where density ratio is low, due to high pressure (black rectangular shape); in this range of density ratio and for St up to 0.03, the computed error is not significant.

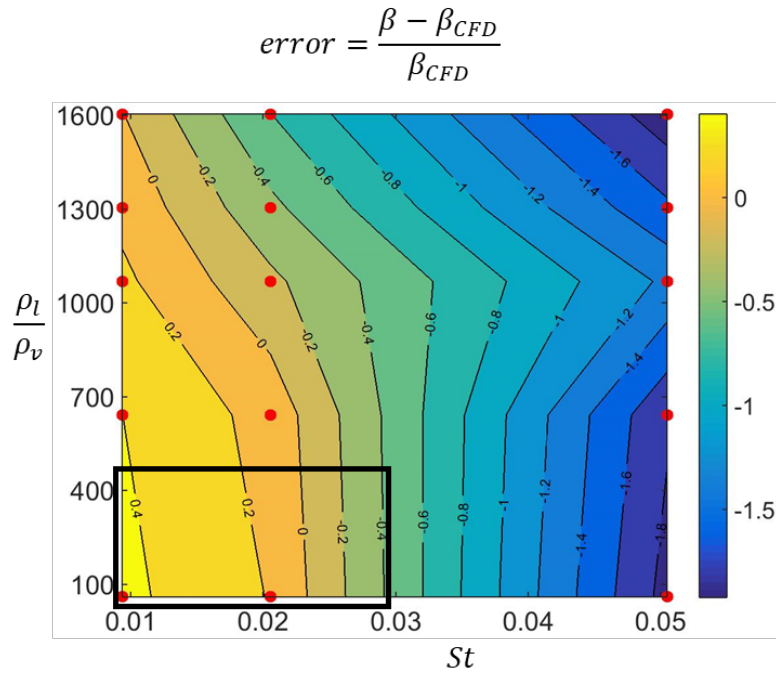


Figure 3-5: Map indicating the error between the predictions of CFD and analytical solution

3.2 Nonlinear droplet oscillation

The current CFD code performance, on reproducing air-liquid interface oscillations in large amplitude, is evaluated against the corresponding results derived by the numerical model of [83]. The initial shape of the droplet is a prolate spheroid, where the ratio of semi-major axis length to that of semi-minor is equal to 3. The volume of the spheroid is $V = 4\pi ab^2/3$, and from that expression the equivalent radius of a sphere with the same volume can be derived. The latter is equal to $r = 3^{1/3}b$ (290 μm). Liquid density and viscosity are set equal to 700 kg/m^3 and $635 \cdot 10^{-6}$ Pa s, respectively. Flow equations alongside with VoF equation are solved in a 2-D planar domain. The base grid spacing is 42 μm . In order to achieve a minimum grid spacing equal to 10 μm (similar to that in [26]), 2 levels of refinement are applied. During the simulation, the droplet oscillations are damped by surface tension force and the droplet tends to recover its spherical shape. Liquid (blue) and air (red) volume fraction are illustrated in the left panel of **Figure 3-6**. The results show good agreement with that derived by [83] (Right panel).

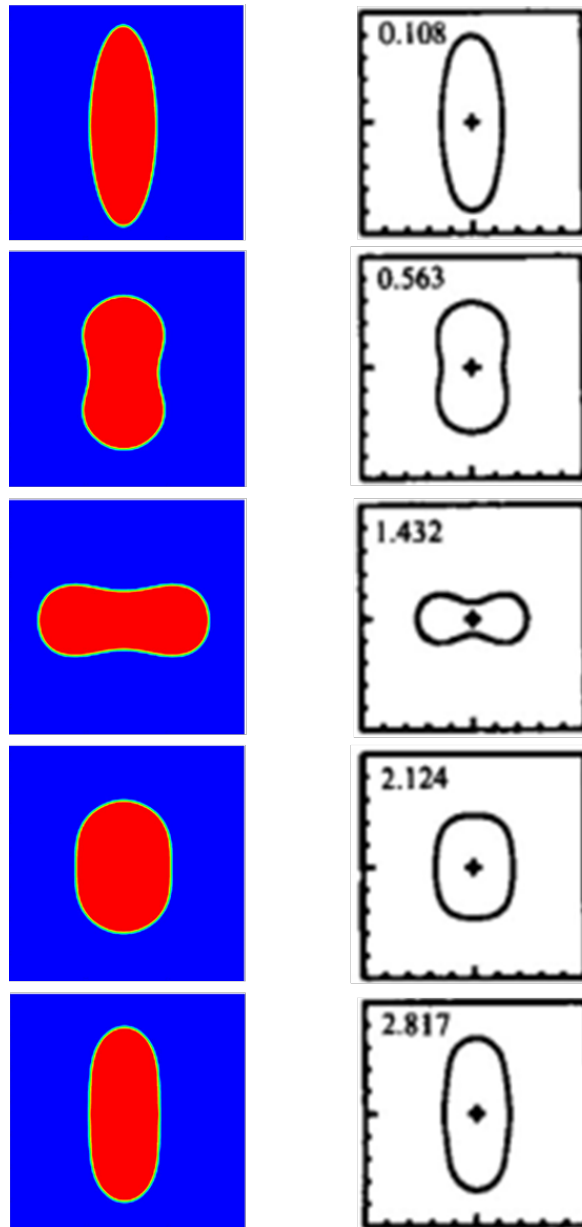


Figure 3-6: Nonlinear droplet oscillations predicted by the current code (Left panel) and the numerical model of [83] (Right panel).

3.3 Breakup of stationary emulsion droplet

The current code is employed in order to simulate the breakup of a stationary emulsion droplet; results of the simulation are compared with that of [26]. Since the emulsion droplet is stationary, the temperature distribution and the bubble location are predefined in the simulation.

3.3.1 Computational setup and examined conditions

A schematic illustration of the examined configuration (left panel) alongside with the computational mesh (right panel) are illustrated in **Figure 3-7**. Equations are solved in a 2-D planar domain where all the boundaries are open and velocity gradient is set to zero. The domain size is $8.4 R_{oil} * 8.4 R_{oil}$; therefore the base grid spacing is $1.36 \mu\text{m}$. In order to achieve a minimum grid spacing equal to $0.17 \mu\text{m}$ (similar to that in [26]), 4 levels of refinement are applied. The parent droplet radius (R_{oil}) is equal to $15 \mu\text{m}$, while the water sub-droplet radius (R_w) is $10.5 \mu\text{m}$. The latter is located at a surface depth (d_w/R_{oil}) equal to 0.12, eccentric to the parent droplet's center. The size of the bubble radius (R_b) is $2.1 \mu\text{m}$ and it is located eccentric to the water-sub droplet center. Inclination angle for both water sub-droplet and vapor bubble is zero. The liquid properties of the oil phase are similar to those of hexadecane. The liquid densities are $\rho_{oil} = 770 \text{ kg/m}^3$ and $\rho_w = 850 \text{ kg/m}^3$. The liquid heat capacities are $c_{p oil} = 2220 \text{ J/kg K}$ and $c_{p w} = 4200 \text{ J/kg K}$. Thermal conductivities are set equal to 0.13 and 0.68 W/m K for oil and water, respectively. The liquid viscosities are $1.6\text{e-}4 \text{ kg/m s}$ for both oil and water. The latent heat of vaporisation of water is $h_l = 2257 \text{ kJ/kg}$. Surface tension between the water vapor and water is set 0.0475 N/m , while that between water and oil is equal to 0.02 N/m . The ambient air pressure is 30 bar, where the corresponding saturation temperature of water is 503 K. Air and oil temperature are predefined and equal to 553 K. Air properties are set constant since no temperature or pressure variation occurs during emulsion droplet breakup. The former are derived by the NIST database [85], for the aforementioned ambient pressure and temperature.

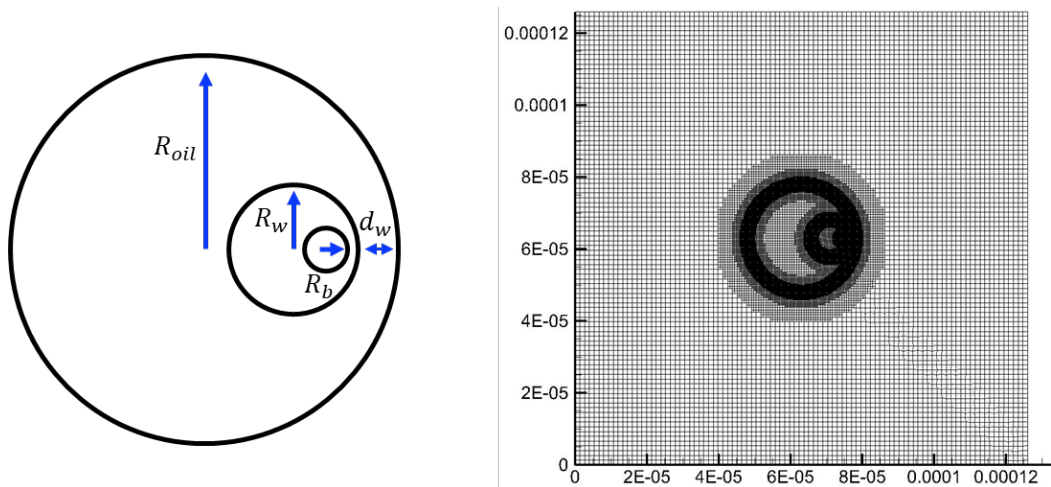


Figure 3-7: Schematic illustration of the stationary emulsion droplet (Left panel) alongside with the computational mesh (right panel)

3.3.2 Results

Density contours of **Figure 3-8** (shows temporal evolution of the breakup phenomenon predicted by the current CFD methodology. Air and water vapor densities are indicated with blue color while oil and water are indicated with yellow and red, respectively. Initially the water vapor bubble starts growing due to boiling of water ($t = 0.4 \mu\text{s}$) and pushes the oil-water interface towards oil-air interface. This breakup stage is known as puffing. Next, the ejected vapor breaks the water-oil interface ($t = 1.4 \mu\text{s}$). Two locations, where interface between both vapor water and oil exists, are observed; these locations start regressing and the water sub-droplet deforms to a non-spherical shape. Finally, oil-air interface ruptures and vapor ejects in the ambient air ($t = 2.5 \mu\text{s}$). Species volume fraction contours of **Figure 3-8** (Left panel) illustrates the temporal evolution of stationary emulsified breakup produced by the model of [26]. Both models show similar behavior especially at the first time instance where puffing occurs. After puffing, it seems that intense oscillations are generated at the water-water vapor boundary and vapor tends to cover the water sub-droplet. The intensity of these oscillations is not produced in the current code. At the final breakup stage, a more “violent” fragmentation of the oil-air boundary is observed, and the parent oil droplet strongly deforms. In both models, the embedded water droplet deforms almost identically.

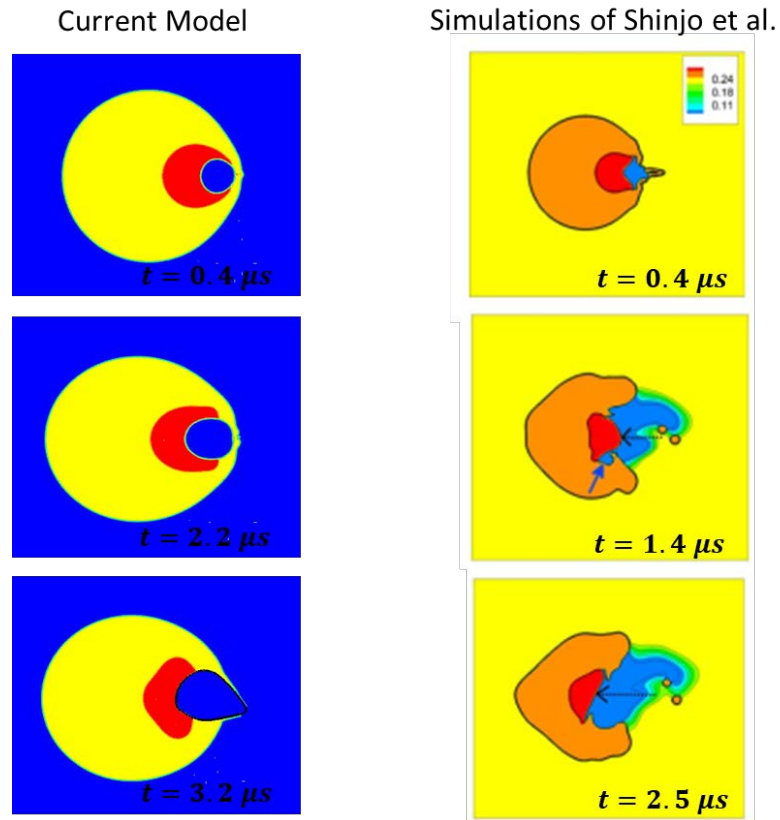


Figure 3-8: Stationary emulsion droplet breakup at $t = 0.4$, $t = 2.2$ and $t = 3.2 \mu s$, predicted by the current CFD methodology (Right panel) and that of [26] (Left panel).

Chapter 4

Computational study of emulsion droplet breakup

4.1 Convective heating of emulsion droplets

In order to develop a model that investigates emulsion droplet breakup under spray conditions, it should be examined first how an emulsion droplet gets heated in presence of an air stream. As it has been mentioned before, in a stationary emulsion droplet configuration, a predefined temperature profile was imposed in each fluid, while a vapor bubble was initially located close to the water-oil boundary. In fuel spray conditions, modeling parameters such as, 1) time instance of vapor generation, 2) site of vapor generation, 3) temperature distribution, should be predicted by the model rather than being imposed as initial conditions.

4.1.1 Computational setup and examined conditions

Convective heating of an emulsion droplet, neglecting boiling of the superheated water, is examined for two different cases. In both cases, properties of *n*-dodecane ($C_{12}H_{26}$) are used for the oil, taken from [85]. For droplet temperature and pressure equal to 300 K and 10 bar, physical properties of *n*-dodecane are the following. Density is $\rho_n = 746.5 \text{ kg/m}^3$, heat capacity $c_{p,n} = 2216 \text{ J/kg K}$, viscosity $\mu_n = 0.001364 \text{ kg/m s}$, and thermal conductivity $k_n = 0.1359 \text{ W/m K}$. The corresponding properties of water are $\rho_w = 997.85 \text{ kg/m}^3$, heat capacity $c_{p,w} = 4172 \text{ J/kg K}$, viscosity $\mu_w = 8.5e - 4 \text{ kg/m s}$, and thermal conductivity $k_w = 0.611 \text{ W/m K}$. Latent heat of vaporisation is equal to 2257 kJ/kg, while surface tension of water and *n*-dodecane are set equal to 0.07 and 0.024 N/m, respectively. In the first case, one embedded water droplet is located inside the parent oil droplet, while in the second case 3 water sub-droplets are embedded in different positions. Equations are solved in a 2-D planar domain, which is schematically shown in **Figure 4-1**, where velocity inlet boundary condition is imposed in the left side; all the rest boundaries are open. Initial velocity of the air stream is equal to 10 m/s. For

the aforementioned properties and conditions, Weber and Reynolds non-dimensional numbers are $We = 0.46$ and $Re = 30$, implying that the droplet will remain spherical. Oil droplet radius is equal to $15\ \mu\text{m}$, while that of water droplets is $1.4\ \mu\text{m}$ for each case examined. The desired mesh resolution is 120 CpR, which is achieved with 3 levels of local refinement. The ambient temperature is set equal to $900\ \text{K}$, which is a realistic value for spray combustion conditions.

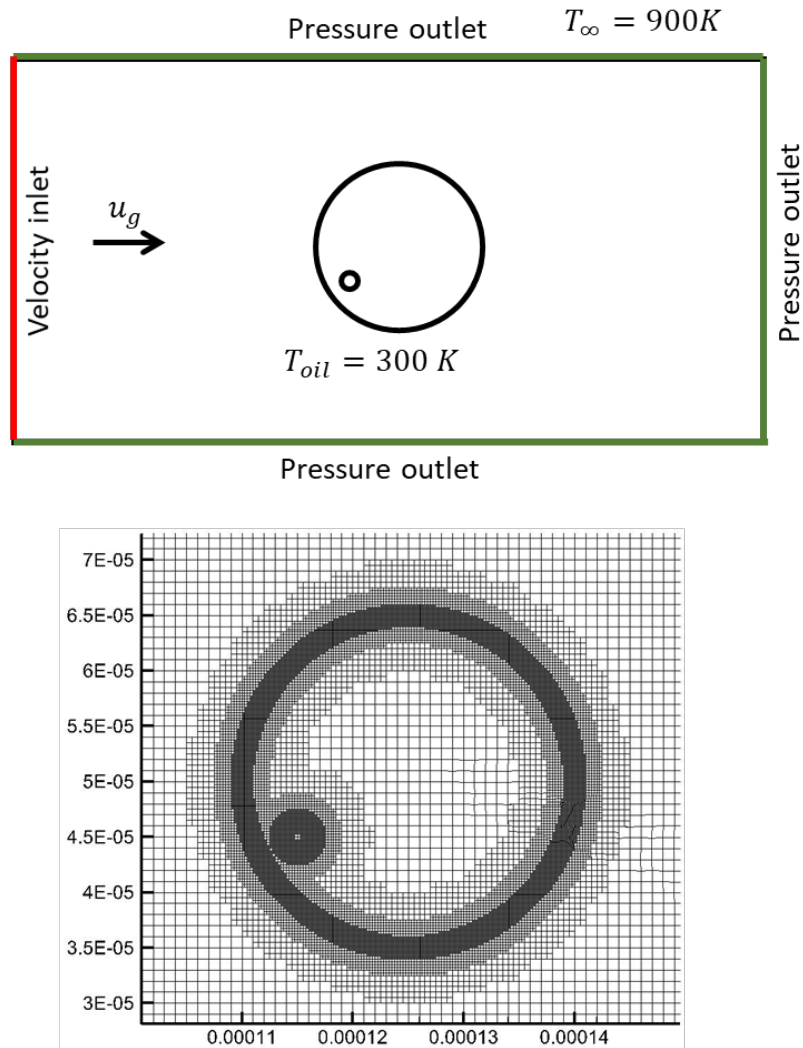


Figure 4-1: Upper panel: Computational 2-D planar domain of an emulsion droplet with one embedded water sub-droplet, initially located upstream. Lower panel: Computational mesh with 3 levels of refinement at the liquid-air interfaces

4.1.2 Results

In the first case, a single water sub-droplet is located upstream inside the parent oil droplet. The latter gets heated because of the hot convective air, which induces an internal flow inside the droplet. The intensity of this secondary flow defines the

temperature distribution of the emulsion droplet. Left panel of **Figure 4-2** shows the temporal evolution of temperature distribution inside and outside of the emulsion droplet. Right after the beginning of the simulation ($t = 0.001\mu\text{s}$), heating occurs due to diffusion. In the next time instance ($t = 88 \mu\text{s}$), it is clear that temperature distribution follows the streamlines formed in the air phase and this trend holds until the last time instance of the simulation ($t = 130 \mu\text{s}$). The effect of liquid flow on temperature distribution inside the droplet, depends on the liquid Peclet number ($Pe_L = Du_s/a$) which expresses the ratio of the advective heat transport to diffusive heat transport. Liquid surface velocity (u_s) is theoretically estimated by [86] and the relationship reads.

$$u_s = \frac{1}{32} u_g \left(\frac{\mu_g}{\mu_l} \right) \cdot Re \cdot C_F \quad (4-1)$$

where $C_F = 12.69Re^{-2/3}$. In case of high Pe_L , temperature profile follows the internal streamlines; in the present case Pe_L is equal to 365 which is a transition from the diffusive to convective regime. Inside the droplet (**Figure 4-2**, right panel-zoom area) two recirculation areas have been formed. These areas are present during the rest of the simulation. A significant feature is that the embedded water droplet (pointed out by red arrow) follows the internal streamlines. The latter drive the sub-droplet towards the downstream side along the oil-air interface.

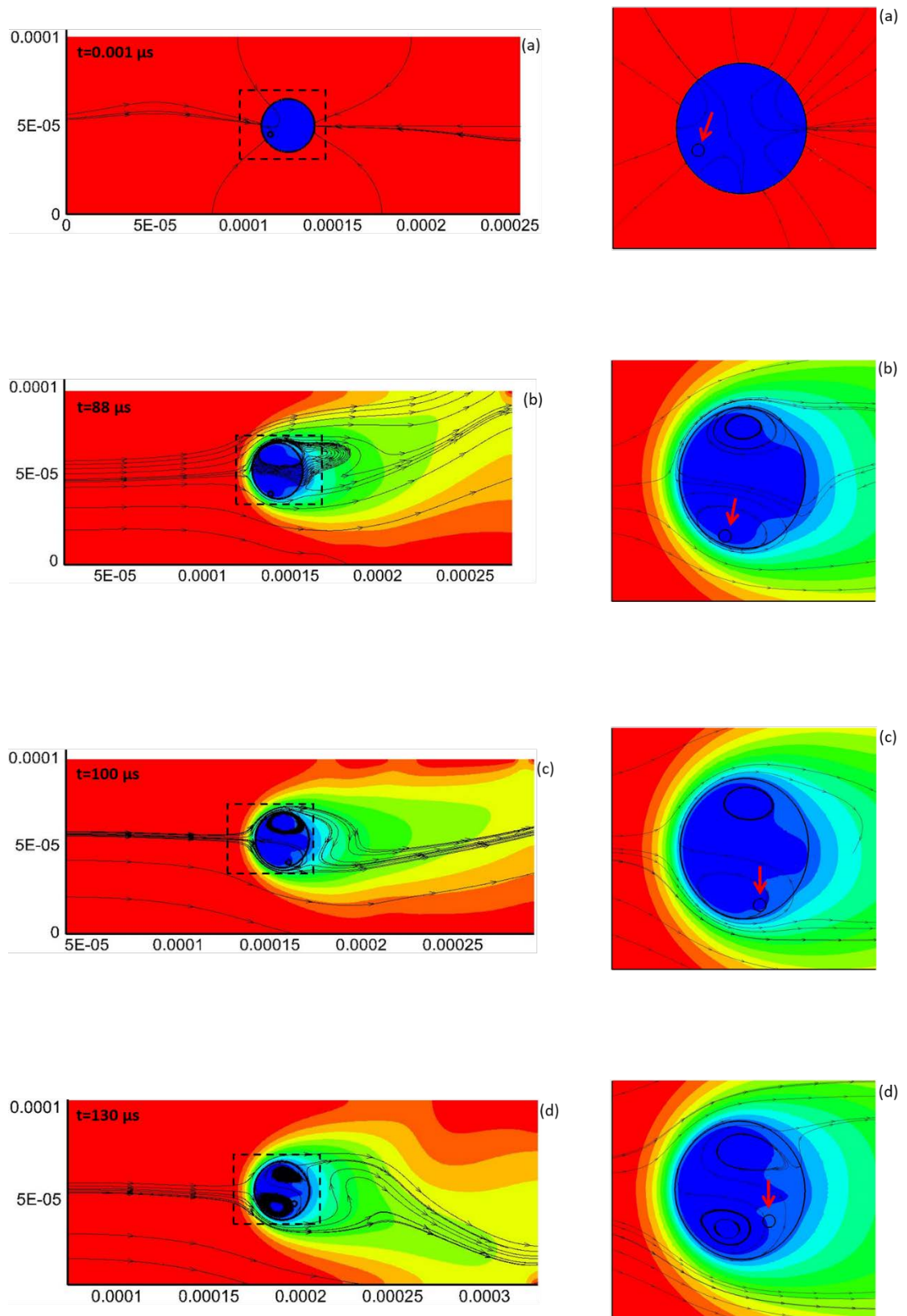


Figure 4-2: Convective heating of an emulsion droplet with one embedded water sub-droplet located upstream. The airflow is from the left to the right

In the second case examined, two additional water sub-droplets are initially located in the downstream and shoulder region. The main aim of this simulation is to investigate the interaction between the droplets and their trajectories. VoF isolines in **Figure 4-3** show that the water sub-droplet initially located in the shoulder region has a small circulating trajectory, while the sub-droplet, initially located in the downstream side, moves towards the upstream side. Here it seems that the symmetrical internal circulation, observed in the previous case, breaks due to the presence of the additional sub-droplets. However, it is clear again that each sub-droplet's trajectory coincides with the internal streamlines.

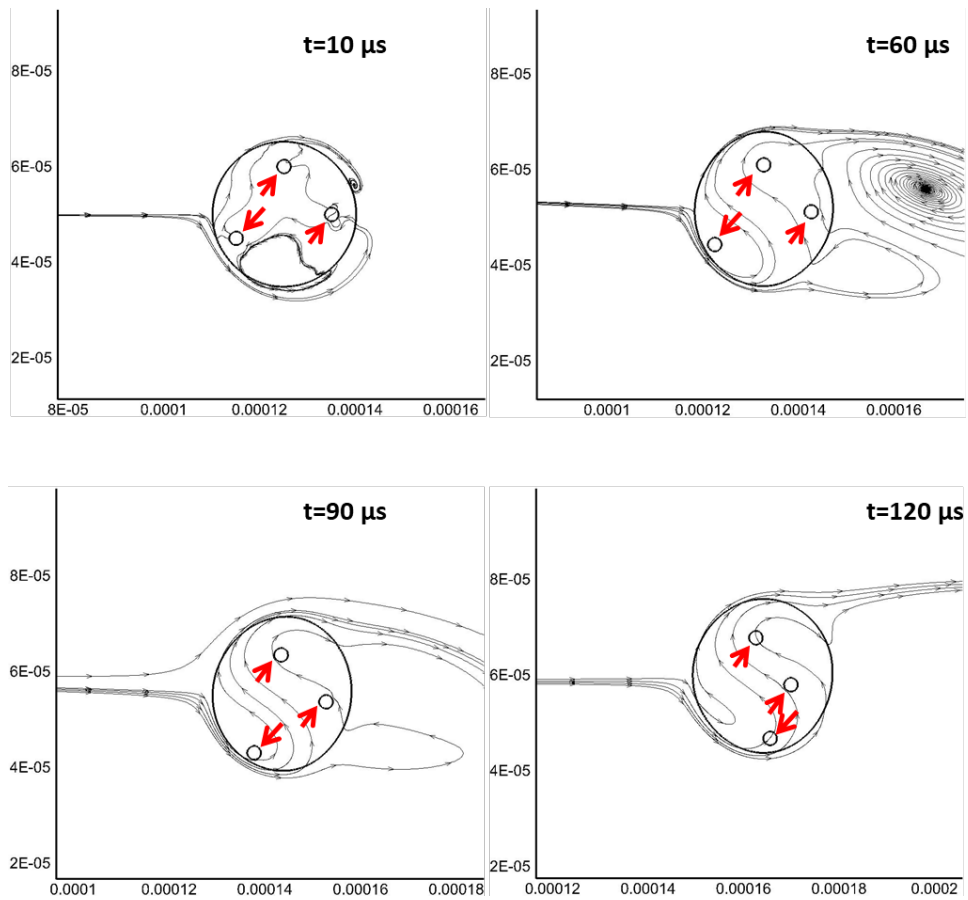


Figure 4-3: Time sequence of the three water sub-droplets moving inside an oil droplet. The air flow is from the left to the right.

4.2 Emulsion breakup subjected to aerodynamic forcing

4.2.1 Computational setup and examined conditions

The initial conditions in the numerical domain reflect typical conditions of a HFO droplet inside the combustion chamber of marine Diesel engines [87]. Equations are solved in an axisymmetric domain where the left vertical axis is a velocity inlet boundary that imposes the velocity of the stream flow, while the rest boundaries are open where velocity gradient is set to zero. The domain extends up to a distance of $5D_d$ in the vertical direction and $10D_d$ in the horizontal one (**Figure 4-4**). Initially, 2 VoF equations are solved with an implicit VOF solver, while an additional VoF equation is solved after vapor is formed. For the spatial discretization of VoF equation, the Compressive scheme is used [88], while momentum equation is spatially discretized with a second order scheme, where quantities at cell faces are computed using a multidimensional linear reconstruction approach [89]. The energy equation is spatially discretised with a first order upwind scheme. The local grid refinement technique [82] enhances the accuracy of the computations at the interface region, while achieving low computational cost compared to a simulation with a uniform grid of the same density. Base grid resolution is such that, with 6 levels of refinement, the initial vapor bubble resolution is ~ 2 CpR, while the resolution corresponding to the outer droplet is 200 CpR. Since an axisymmetric configuration is employed, the initial vapor bubbles are imposed to be located on the axis of symmetry in order to have a spherical shape. The algorithm responsible for vapor formation, as described in subsection 2.2, can be further modified in order to account for the formation of more than one initial bubbles in the proximity of the water droplets' interface. In such a case, the initial bubbles that are not located on the axis of symmetry are expected to have a torus shape instead of a spherical one. Such a vapor formation could exist inside a realistic emulsion droplet configuration, but its growth, due to temperature differences, would not be predicted by the phase change algorithm of the current model.

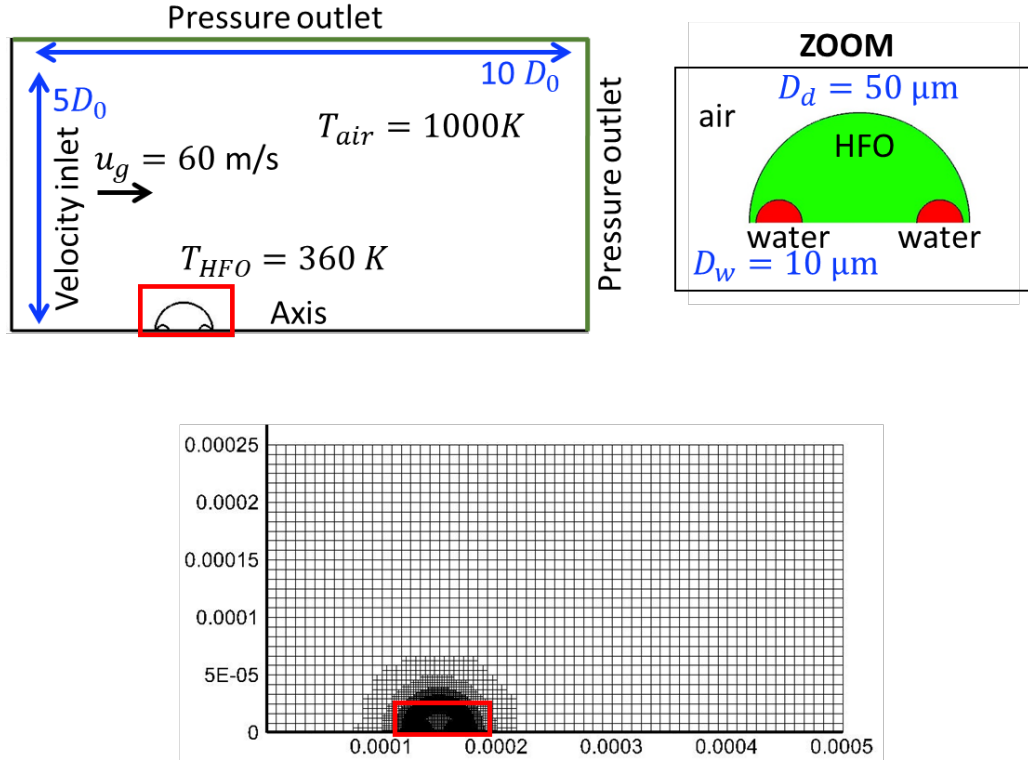


Figure 4-4: Computational axisymmetric domain, with zoom at levels of local refinement around the HFO-air and HFO-water interfaces.

In all the examined cases, the water in HFO (W/HFO) emulsion droplet contains two water sub-droplets which are located in the front and the back of the oil droplet in order to capture the interface rupturing; this may occur in both sides depending on the local temperature. The emulsion droplet is placed at ambient pressure $p = 30$ bar and temperature $T_g = 1000$ K. The droplet's injection temperature is 360 K while the boiling temperatures of HFO and water are 660 K and 506 K, respectively. The physical properties of HFO are representative of those used in marine engines. Liquid density, dynamic viscosity and surface tension can be found in the work of [90], while thermal conductivity and heat capacity are computed by empirical relationships provided by [91]; these were assumed constant without any temperature dependence. The initial HFO droplet diameter is $D_{HFO} = 50 \mu\text{m}$, which is typical droplet size in sprays [92], while the diameter of the embedded water droplets was selected equal to $D_w = 10 \mu\text{m}$. That size has been also investigated in past studies [26, 93, 94]. At this point, it should be mentioned that it's rather complicated to relate the sub-droplet size with the corresponding water content of the emulsion, since emulsions may contain different amount of water sub-droplets but the same water content; in both cases it is expected a different puffing/micro-explosion outcome. The superheat degree, which is an input parameter to the model, has been

selected equal to $\Delta T_s = 10$. The latter value corresponds to a St number equal to 0.02. For the aforementioned St number and the computed water-water vapor density ratio ($\rho_w/\rho_v = 60$), the OCASIMAT algorithm predicts with high accuracy the bubble growth rate; according to **Figure 3-5**, the error is less than 0.2. The examined We numbers in the cases range from 40 to 190, which correspond to droplet velocities in the range of 10-100 m/s. The latter is a typical velocity range in HFO fueled engines [92]. The Oh number is calculated equal to 0.9, implying that viscous phenomena are important. The thermophysical properties and non-dimensional numbers are summarized in the following tables.

	Units	Water Liquid	Water Vapor	HFO	Air
T	K	360	506	360	1000
ρ	kg m ⁻³	968	15	907	10.3
c_p	J kg ⁻¹ K ⁻¹	4195	3612	2020	1143
κ	W m ⁻¹ K ⁻¹	0.675	0.047	0.127	0.068
μ	kg m ⁻¹ s ⁻¹	3.2 10 ⁻⁴	1.69 10 ⁻⁵	0.032	4.3 10 ⁻⁵
h_{lv}	J kg ⁻¹	1.794 10 ⁶			

Table 4.1: Thermophysical properties (computed by [91]). The pressure was assumed constant at 30bar.

Non-dimensional number		
We_g	$\rho_g u_{rel}^2 D_{HFO} / \sigma$	70
Pe_{HFO}	$D_{HFO} u_{oil} / \alpha_{oil}$	200
Re_g	$\rho_g D_{HFO} u_{rel} / \mu_g$	720
Oh_{HFO}	$\mu_{HFO} / \sqrt{\rho_{HFO} \sigma D_{HFO}}$	0.9
St_w	$c_{pl,w} \Delta T_s / h_{lv}$	2.3 10 ⁻²

Table 4.2: Non-dimensional numbers

4.2.2 Results

4.2.2.1 W/HFO emulsion droplet breakup

Here, W/HFO emulsion droplet breakup is examined for a reference case where the initial velocity of the air stream is $u_g = 60$ m/s resulting in a We number equal to 70. The temporal evolution of the emulsion droplet is illustrated in **Figure 4-5**. Each panel is split at the middle, showing different quantities above and below the axis of symmetry. The upper part shows the temperature field alongside with the streamlines, while in the lower part the contributing phases are illustrated. The time (t^*) is non-dimensionalised with the shear timescale t_{sh} . One can see that at the initial stage, steep temperature gradients are formed near the droplet interface. At $t^* = 0.06$, a temperature distribution is formed in the surrounding air phase; the emulsion droplet is subjected to convective heating and the inner temperature profile tends to follow the streamlines; the inner droplet temperature has not increased much though. At the next time instance ($t^* = 0.64$), the same features in the air phase are observed but the temperature of the front water sub-droplet has locally reached the superheat degree for the onset of bubble formation. The criteria for the vapor generation have been fulfilled and the appearance of a vapor bubble is observed (zoom at **Figure 4-5 b**). The vapor bubble starts growing due to the temperature difference at its interface. The growth rate of the bubble formed in the upstream droplet, is shown in ... in terms of the dimensionless equivalent bubble radius (this was obtained from the bubble volume). In the horizontal axis, the time instance of bubble formation has shifted to zero. As seen, the bubble radius grows in time according to \sqrt{t} as predicted by the Scriven's theory, while the growth constant β was computed higher compared to the theoretical one which is attributed to deviations from Scriven's theory, i.e. bubble growth inside a droplet instead of a pool, spherical asymmetry, shape deformation and bubble motion. Fragmentation of the HFO-air boundary occurs at $t^* = 1.01$ and vapor is injected in the ambient air; in the present work, this is considered as the breakup initiation time; small HFO fragments (indicated by red arrow) are observed (zoom at **Figure 4-5 c**). This feature is observed clearly at $t^* = 1.12$ (vapor phase indicated by red colour). The corresponding vapor bubble growth and breakup process occurs also, with a temporal delay, in the downstream region of the parent droplet. These results indicate that the breakup regime in this case is puffing, since partial breakup of the W/HFO droplet occurs. The droplet deformation due to aerodynamic forces plays a minor role

here, since the combination of We and Oh numbers examined corresponds to a relative slow deformation process.

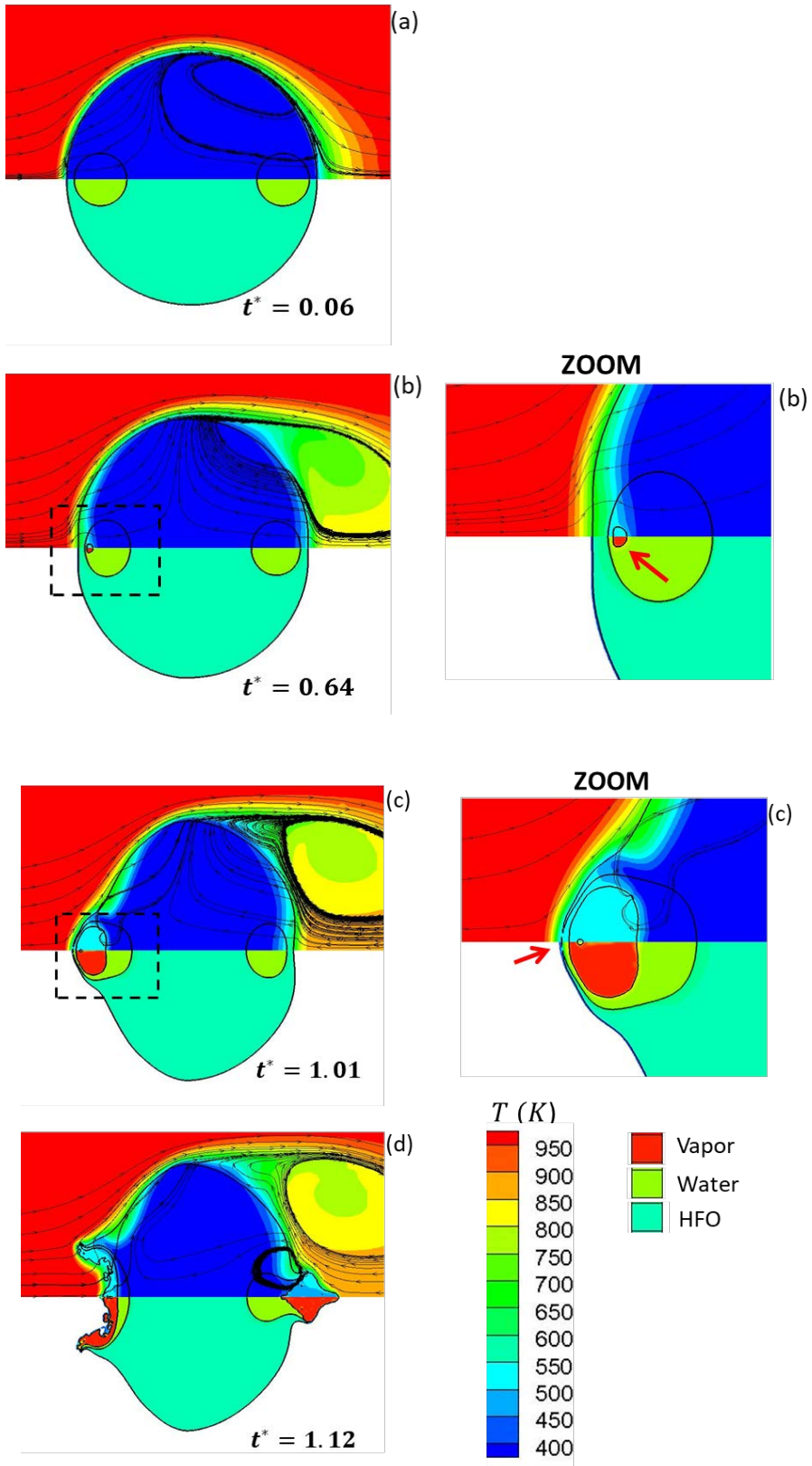


Figure 4-5: Temporal evolution of emulsion droplet breakup. Upper part: Temperature profile. Lower part: HFO, water and vapor phases indicated by ciel, green and red respectively.

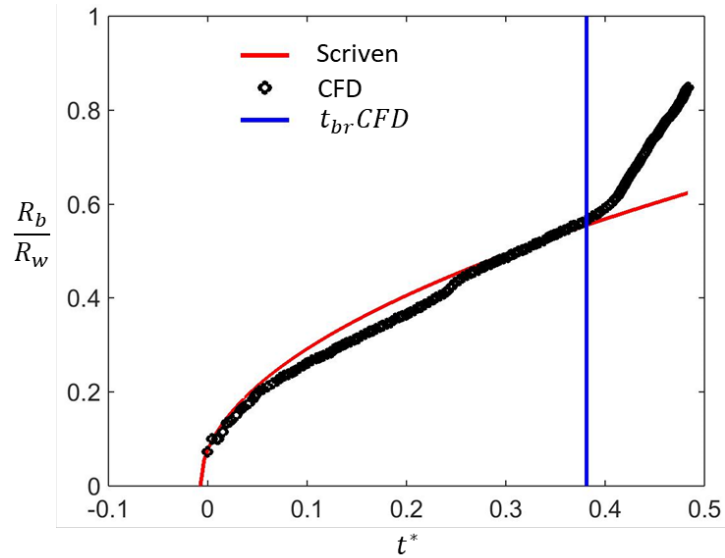


Figure 4-6: Nondimensional vapor bubble radius predicted by Scriven solution (red solid line) and CFD simulation (black scatter) for the front bubble with $We = 70$ and a corresponding breakup initiation time (vertical blue line)

4.2.2.2 Parametric study with Weber number

Having identified the physical phenomena occurring during the coupled thermal and aerodynamic loading of the droplet, the effect of We number on the breakup initiation time of the W/HFO emulsion droplet is examined in detail. For the examined range of We numbers, simulations are also performed for neat HFO droplets in order to predict their breakup initiation time due to aerodynamic forces and compare it against those when puffing/micro-explosion is accounted for. For the default Weber number ($We = 70$) case, the temporal evolution of the neat HFO droplet (right panel) is illustrated in **Figure 4-7**, alongside with those of the benchmark W/HFO emulsion cases (left panel). The neat HFO droplet breaks under aerodynamic forces at $t^* = 10.5$, which is an order of magnitude longer compared to the breakup initiation time of W/HFO emulsion. This clearly reveals the advantage of using emulsified droplets in viscous fuels.

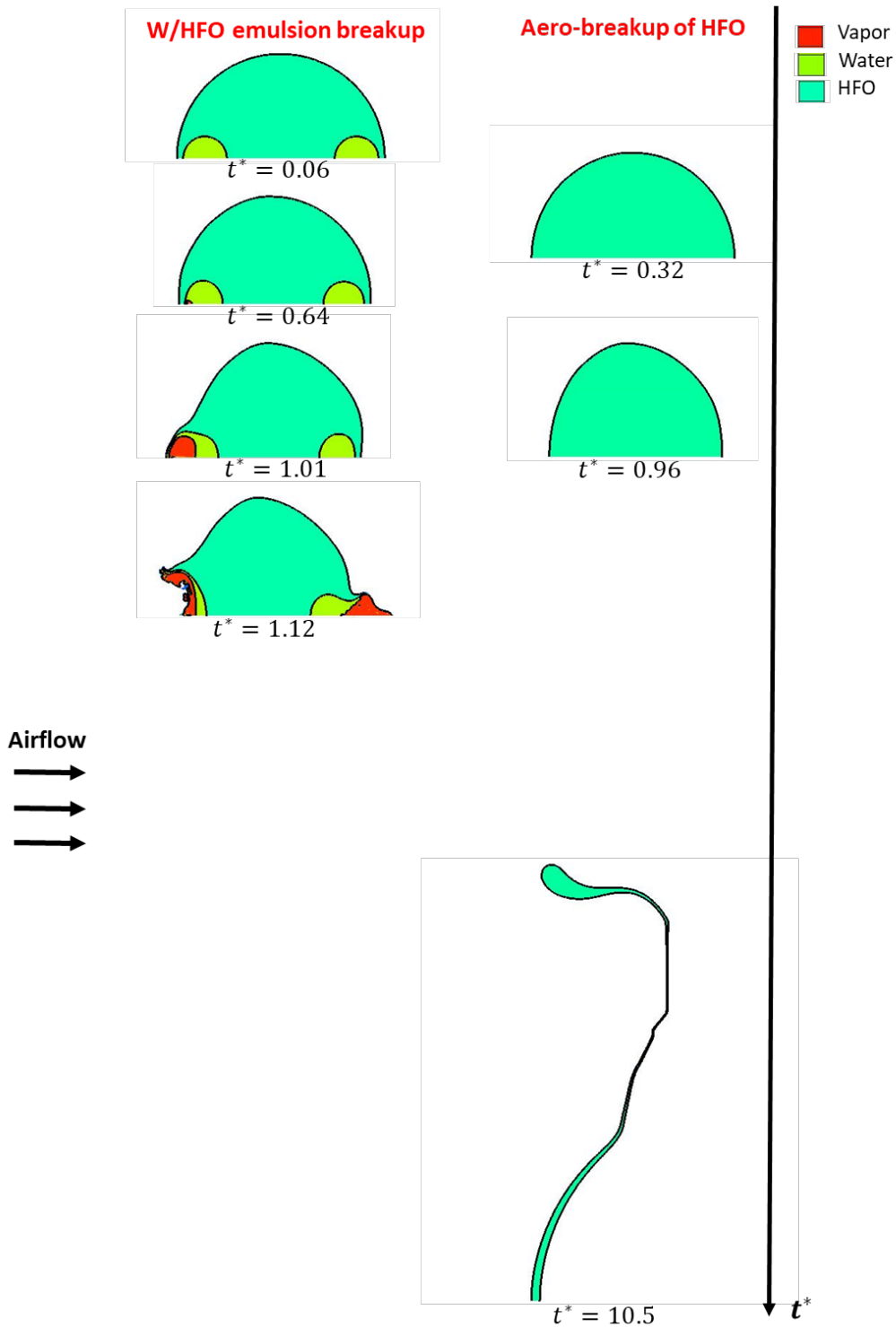


Figure 4-7: Temporal evolution of W/HFO emulsion droplet (Left panel) and neat HFO droplet (Right panel) for We number equal to 70.

In the upper panel of **Figure 4-8**, the dependence of the breakup initiation time on the We number is illustrated. For the case of aerodynamic droplet breakup (blue scatter), the breakup initiation time decreases strongly with increasing We number, which is in

accordance with several past studies [87, 95]. Regarding the breakup of emulsified droplets (black scatter), lower panel of **Figure 4-8** shows a weak decreasing dependence on We number. In each We number correspond two black scatters which stand for breakup initiation time of the upstream and downstream side of the emulsion droplet. It is observed that the difference between the two time instances decreases as We number increases. Overall, it is quite important to mention that the emulsion breakup occurs 4-10 times faster than the aerodynamic breakup. The latter trend indicates that puffing/micro-explosion process can speed up the breakup of the droplet relative to the mechanism of the aerodynamic breakup, at least for the range of conditions ($Oh \approx 1, We < 200$).

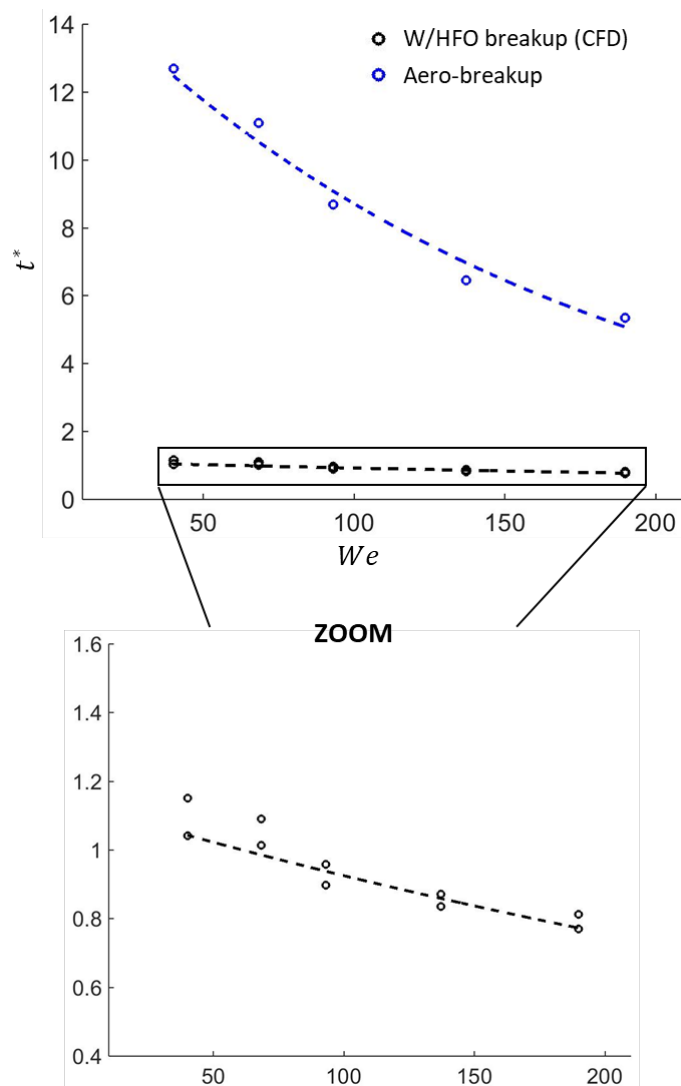


Figure 4-8: Breakup time of W/HFO emulsion droplet for a range of We numbers (black scatter). Aerodynamic breakup of neat HFO droplet for the corresponding range of We numbers (blue solid line).

4.2.2.3 Droplet deformation

Besides the breakup initiation time, one of the most important magnitudes determining the combustion efficiency is the breakup extent of the droplet. In **Figure 4-9**, it is observed that the W/HFO emulsion droplet is slightly deformed after its breakup initiation time compared to its initial spherical shape. It is expected that if a larger amount of water sub-droplets was located in the parent droplet, simultaneous (and/or successive) boiling will occur in each sub-droplet and the deformation will be significant. This aspect is indicated in **Figure 4-9**, where the dimensionless surface area of the W/HFO emulsion droplet and the neat HFO droplet are illustrated; the surface area of the latter has significantly increased up to the breakup initiation time. On the right panel, a focus on the breakup initiation time of the W/HFO emulsion shows a slight increase in its surface area. It is clear though that the surface area of the W/HFO emulsion increases between the successive explosion of the downstream and upstream water sub-droplet.

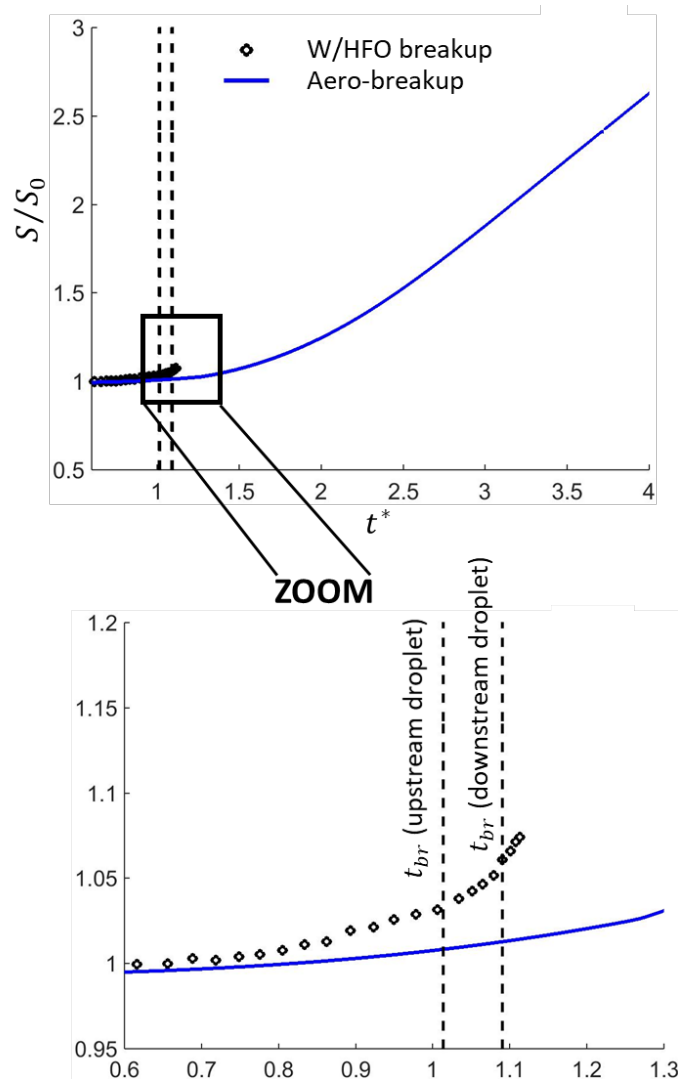


Figure 4-9: Temporal evolution of the dimensionless surface area of the W/HFO emulsion (scatter) and the neat HFO droplet (blue line)

4.2.2.4 Effect of bubble surface depth and superheat degree on W/HFO emulsion breakup

In subsection 2.2 a mechanistic model that is responsible for bubble formation inside the embedded water sub-droplet was presented. The criteria under which a vapor bubble is generated in a computational cell, are that the latter should reach a superheat degree (ΔT_s) and have a specific distance (d_i) from the water-HFO interface. Both of these are input parameters of the model. A parametric study with d_i and ΔT_s is performed, for the reference case of $We = 70$, in order to investigate their sensitivity on emulsion breakup time. The results are compared against the parametric study of breakup time with We number (**Figure 4-8**). Horizontal axis of **Figure 4-10** indicates the aforementioned parameters $\lambda = \langle d_i, \Delta T_s, We \rangle$, which are normalised with the examined values of the reference case. Results show that breakup initiation time slightly increases with d_i (blue scatter), which is expected since the heat wave needs to penetrate deeper inside the water sub-droplet and subsequently the bubble is formed at a later time instance. Regarding the effect of superheat degree, it seems that breakup initiation time slightly changes (red scatter) without having a clear trend with ΔT_s . Finally, it is observed that both parameters are much less sensitive to breakup initiation time compared to the effect of We number (black scatter); when the latter increases five times, the breakup initiation time becomes approximately an order of magnitude lower.

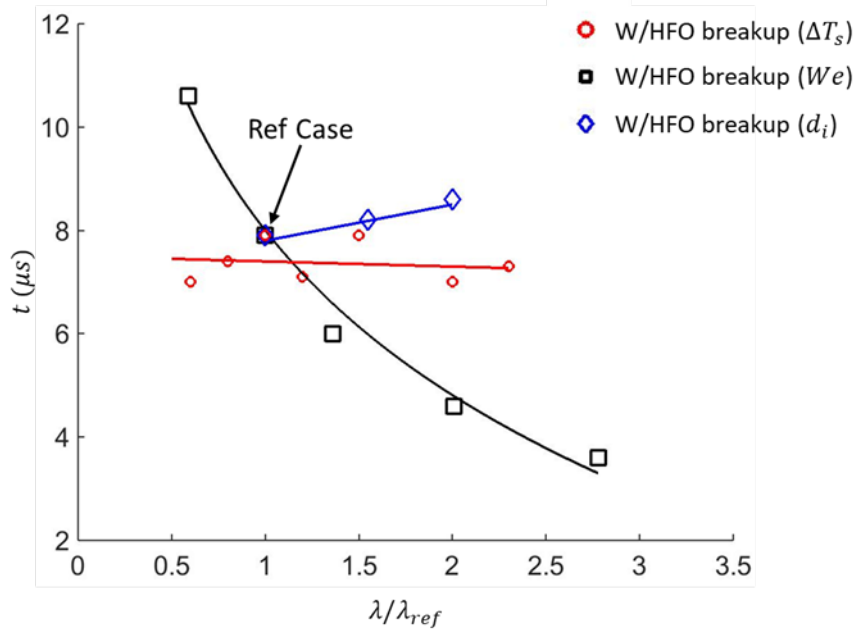


Figure 4-10: Breakup initiation time of W/HFO emulsion with superheat degree (red scatter), bubble surface depth (blue scatter) and We number (black scatter)

4.3 Conclusions

Convective heating of emulsified droplets was numerically investigated without considering boiling of the water sub-droplet. It was found out that temperature distribution highly depends on liquid Peclet number (Pe_L). Next, the overall behavior of a W/HFO emulsion droplet was simulated starting from droplet heating up to breakup instance. A benchmark case was presented where a W/HFO emulsion droplet is injected, with an initial velocity $u_g = 60$ m/s, at ambient pressure $p = 30$ bar and temperature $T_g = 1000$ K. Two water sub-droplets were located inside the parent droplet in the downstream and upstream side. It was observed that the atomization of the emulsion droplet is puffing-induced. Finally, numerical simulations of W/HFO emulsion droplet breakup for a range of We numbers that are typical in Diesel engines, were performed. The diameter of HFO droplet and Oh number were the same for each parametric case and they were equal to $50 \mu m$ and 0.9 , respectively. Additionally, aerodynamic breakup of a neat HFO droplet, with the same properties and initial conditions, was simulated for comparison purposes. It was revealed that for the viscous fuel examined ($Oh > 1$) puffing/micro-explosion speeds up the droplet breakup by almost an order of magnitude relative to the aerodynamic breakup. This is more evident for relatively low We numbers, while increasing the We number results in faster breakup.

Chapter 5

A simple model for breakup time prediction of emulsion droplets

In the previous chapter, the combined effect of thermal (due to micro-explosion) and aerodynamic secondary droplet breakup processes, were investigated, with the aid of CFD simulations. The whole process, starting from droplet heating up to vapor expansion and droplet fragmentation, was simulated in order to predict the corresponding time needed for the process to occur. In the current section, the CFD methodology is initially employed to examine a wide range of conditions, namely We and $p - T$ values ($40 < We < 200$, $10 < p < 140$ bar, $600 < T < 2000$ K) including also those typically realised in marine engines during the main injection phase ($p \sim 120$ bar, $T \sim 900$ K). The emulsion droplet diameter and air stream velocity range, correspond to the aforementioned We range, are $50 \mu\text{m}$ and $40 < u_g < 100$ m/s, respectively. From the numerical simulations, two distinct timescales are estimated: the heating time until the water boiling initiation and the vapor bubble growth time until fuel droplet break up. These results are subsequently used to derive a fitting model predicting the W/HFO emulsion breakup initiation time. The numerical methods used, scope and rationale for suggesting the proposed correlations for this wide range of conditions, that has been documented in a number of relevant previous works of the authors [96-100] is to overcome the restrictions imposed by the enormous computational time required by CFD simulations while they further resolve the limitation of mesh resolution realized when small water droplet sizes ($1 \mu\text{m}$) are located at the proximity of the HFO-air interface. In the works of [96, 99, 100] the aerodynamic induced breakup of a single droplet and droplets in tandem was investigated while in [97, 98] heat transfer and evaporation of a single fuel droplet was simulated. The fitting model can reproduce breakup time predictions faster and without the restrictions imposed by the mesh resolution of the CFD model; such a limitation is the simulation of realistic water droplet sizes ($1 \mu\text{m}$) located at the proximity of the HFO-air interface

5.1 Examined conditions

The CFD methodology is employed to examine a configuration where a single spherical water sub-droplet ($D_w = 10 \mu\text{m}$) is located inside a fuel droplet ($D_f = 50 \mu\text{m}$) as shown in **Figure 5-1**; note that the figure is not in scale.

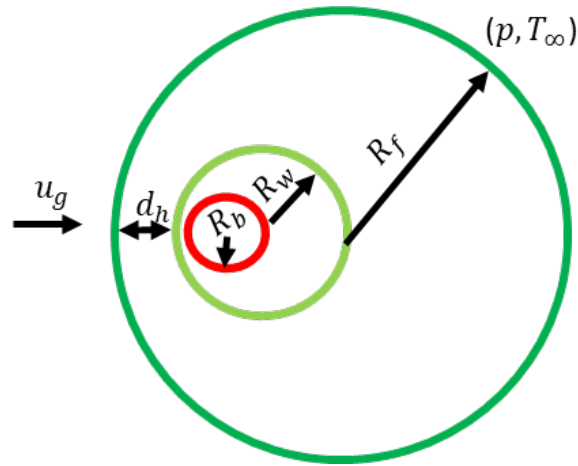


Figure 5-1: Schematic illustration of the emulsion droplet

The emulsion droplet is initially placed at ambient air with pressure p and temperature T_∞ (range of values is illustrated in **Table 5.1**), while the initial fuel temperature is T_0 (360 K). Evaporation of the parent fuel droplet is ignored, since its timescale is much longer compared to that of emulsion breakup [26]. The examined properties are similar to that of a highly viscous HFO, while the preheating temperature of the fuel and the ambient conditions examined ($p = 90 \text{ bar}$, $T = 900 \text{ K}$) are typically met in large marine Diesel engines. Since a 2-D axisymmetric domain is adopted, the embedded water droplet can only be located on the axis of symmetry. Fuel density, dynamic viscosity and surface tension can be found in the work of [90], while thermal conductivity and heat capacity are computed by empirical relationships provided in [91]; these properties were assumed constant at (p, T_0) without accounting for their slight change due to droplet heating, while the surrounding air properties were computed at (p, T_∞) . A couple of parametric runs has been performed for increased ambient pressure equal to 100 and 120 bar, respectively. In those cases, the properties of ambient air, water and water vapor have been computed from NIST database while properties of HFO are assumed to be constant and vary only with the initial ambient temperature. In order to investigate emulsion breakup in even higher pressure conditions, real fluid properties of the fuel could be introduced in the model which vary with respect to both pressure and

temperature. Model predictions have been obtained as function of the water droplet location inside the parent droplet, We and $p - T$ conditions, summarized in **Table 5.1**; in all simulations performed, one parameter is changed each time. For the cases 1 to 4, where the air temperature is varied, the corresponding change in the air properties is compensated by a corresponding change in the air stream velocity in order to keep the We number constant. In cases 5 to 7, the effect of the dimensionless distance δ of the water sub-droplet from the from the HFO-air interface ($\delta = d_h/R_f$) is examined; δ approaching 0 indicates that the water droplet approaches this interface. The effect of water content is not examined here. In practice, a wide range of water droplet sizes will appear in emulsion droplets; such cases require a 3-D approximation which is impossible to resolve since enormous CPU resources are required. Finally, it is pointed out that the effect of Nusselt, Peclet, Prandtl, Biot and Stanton numbers, which are relevant in heat transport processes, has also not been examined. This is justified as the variation of the HFO physical properties in the examined range of temperatures is not significant, while at the same time, the study of lighter fuels is out of scope in the present work, as water emulsions are not utilised in practice. On the contrary, the variation of the We number is relevant since it controls the aerodynamic-induced deformation of the parent droplet.

	T_∞	p_∞	We	d_h/R_{oil}
ref	1000	30	68	0.06
Case 1	700	30	68	0.06
Case 2	800	30	68	0.06
Case 3	1200	30	68	0.06
Case 4	1400	30	68	0.06
Case 5	1000	30	68	0.02
Case 6	1000	30	68	0.05
Case 7	1000	30	68	0.15
Case 8	1000	30	40	0.06
Case 9	1000	30	92	0.06
Case 10	1000	30	136	0.06
Case 11	1000	30	188	0.06
Case 12	1000	10	68	0.06

Case 13	1000	50	68	0.06
Case 14	1000	100	68	0.06
Case 15	1000	120	68	0.06

Table 5.1: Operating conditions for the examined cases. For all cases $Oh \sim 0.9$

5.2 Mathematical description

The correlations of this model are based on the assumption that the emulsion-induced breakup time can be split into two distinct time periods (Eq. 5-1): (i) the time period t_h of water droplet heating from its initial temperature T_0 up to a superheated one $T'_{sat} = T_{sat} + \Delta T_s$ where the formation of a tiny water-vapor bubble is realized; (ii) the subsequent time period t_{grow} during which the water-vapor bubble grows up until the HFO-air interface eventually breaks up.

$$t_{br} = t_h + t_{grow} \quad (5-1)$$

The time period t_h depends mostly on a heat convection time t_{conv} inside the fuel phase, as shown in Eq. 5-2. This assumption is valid since the fuel Peclet number ($Pe_f = D_f u_f / a$) is in the range 3000-7000. The characteristic velocity magnitude u_f is computed as reported in [101, 102] and it is based on the air-fuel density ratio and the air stream velocity. While t_{conv} forms the basis for the estimation of t_h , three empirical coefficients (f_{We} , f_T and f_δ) have been considered to quantify the influence of We ($0 - 200$), air temperature ($600 < T_\infty < 2000$) and location δ ($0 - 0.15$) of the water droplet from the HFO-air interface. The derivation of these coefficients, shown in Appendix A, is based on the superposition principle without accounting for any interdependencies between the parameters examined; the validity of this assumption is discussed in sub-section 5.3.4.

$$t_h = C \cdot t_{conv} \cdot f_T \cdot f_\delta \cdot f_{We}, \quad C = 3.6$$

$$u_f = u_g \sqrt{\frac{\rho_g}{\rho_f}} \quad (5-2)$$

$$f_T = \left(\frac{T_{sat} - T_0}{T_\infty - T_0} \right)^{0.4}$$

$$f_\delta = 1 + 8.9 \cdot \delta$$

$$f_{We} = We^{-0.22}$$

It can be observed that the heating time decreases with increasing air temperatures and We . Moreover, a preheated water droplet at the saturation temperature will have zero heating time (i.e. vapor will form instantly); on the contrary, for a water sub-droplet approaching the HFO-air interface ($\delta = 0$), the bubble will not form instantly and a finite time is needed to reach the required superheated temperature.

Turning now to t_{grow} , the Scriven's solution [39] initially serves as the basis for its derivation (see Appendix A for further details); the values of the coefficients g_{br} , g_p , g_T and g_{We} , accounting for the influence of pressure ($10 < p < 140$ bar), air temperature ($600 < T_\infty < 2000$) and We ($0 - 200$), have been determined after calibration with the corresponding CFD results. Note here that for small We and $p - T$ values, the corresponding coefficients tend to unity ($g_p g_T g_{We} = 1$), indicating that Scriven's theory is valid for those conditions without imposing any modifications. The relationship for t_{grow} alongside with that for the implemented correction factors reads:

$$t_{grow} = \left(\frac{R_w^2}{a_w \beta^2} \right) \cdot \left(\frac{g_{br}}{g_p g_T g_{We}} \right)^2$$

$$\beta = \sqrt{\frac{12}{\pi}} \left\{ \frac{\Delta T_s}{\left(\frac{\rho_g}{\rho_w} \right) \left[\frac{h_{lv}}{c_{p,w}} + \left(\frac{c_{p,w} - c_{p,g}}{c_{p,w}} \right) \Delta T_s \right]} \right\}$$

$$g_{br} = 0.5 + 30 \cdot We^{-1.5} \tag{5-3}$$

$$g_p = 1 + 0.36 \cdot \left(\frac{p}{p_{ref}} \right)^{2.21}$$

$$g_T = 1 + 0.28 \cdot \left(\frac{T_\infty - T_0}{T_{\infty,ref}} \right)^{-0.7}$$

$$g_{We} = 1 + 0.008 \cdot We^{0.9}$$

5.3 Discussion

5.3.1 Overall performance

Predictions for the breakup time obtained from the above correlations are shown in **Figure 5-2** along with those predicted from the CFD simulations for the conditions of

Table 5.1. The 45° line is also illustrated (black solid line); ideally all CFD simulation points should lie on this line together with the corresponding predictions of the fitting model in the case it was in perfect agreement with CFD. In addition, the lines corresponding to the maximum $\pm 10\%$ deviation between the fitting model predictions and the corresponding CFD results (black dashed lines) are also indicated.

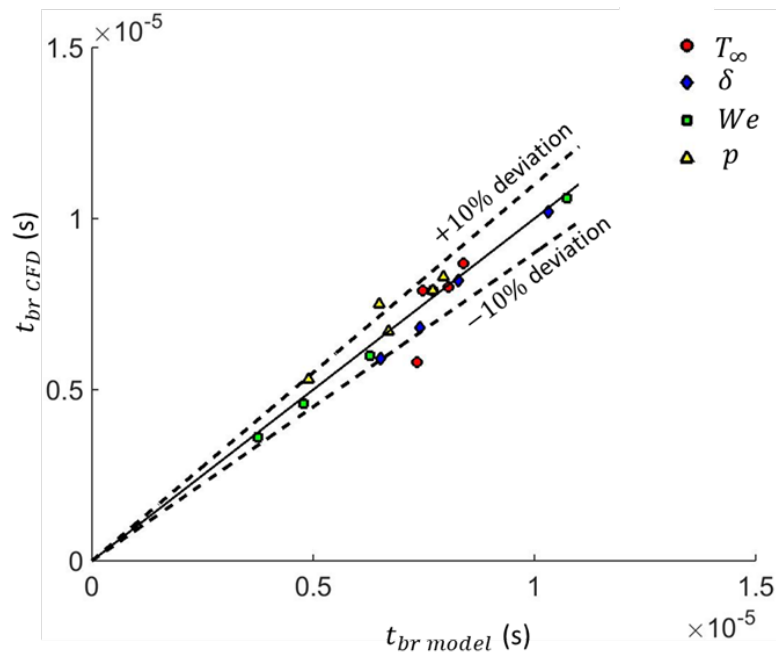


Figure 5-2: Emulsion breakup time as predicted by Eq. 5-1 (black solid line) alongside with $\pm 10\%$ deviation lines (black dashed lines) and the CFD simulations (scatter symbols)

5.3.2 Parametric study with We and $p - T$ conditions

The aerodynamic-induced breakup of a neat fuel droplet is typically characterized by the Weber (We) and Ohnesorge (Oh) numbers; the Reynolds number and the fuel-to-air density (ϵ) and viscosity (N) ratios [74]. The shear breakup timescale $t_{sh} = D\sqrt{\epsilon}/u_g$ is

indicative of the time needed for breakup to be completed [75], while the breakup initiation time can be predicted by the relationship proposed in [87] (among others):

$$t_{aero} = \frac{t_{sh} \cdot 8.95 \cdot We^{-0.352} Re^{-0.086}}{1 + (\rho_f/\rho_g)^{-0.5}} \cdot (1 + 2.36 \cdot Oh^{0.93}) \quad (5-4)$$

This relationship is employed in order to compute the aerodynamic-induced breakup time of a neat HFO droplet and compare it with the emulsion-induced breakup time (Eq. 5-1), for the range of We numbers tested. The upper panel of **Figure 5-3** shows that t_{aero} (black dashed line) decreases strongly with increasing We , which is in accordance with several past studies [87, 95], while a weak decreasing dependence of the emulsion breakup on We is observed (black solid line). The difference between t_{br} and t_{aero} decreases as We increases; however it is important to mention that emulsion breakup occurs 3-5 times faster than the aerodynamic breakup for the conditions examined. This difference is in agreement with the results of [1]. The relative duration of heating (t_h ; red dashed line) and growth (t_{grow} ; blue dash-dot line) times, for the range of We numbers examined, is also shown in **Figure 5-3**. The heating time decreases exponentially as We increases due to the increase of convection, while bubble growth time slightly changes. Moreover, it is observed that for low We numbers ($We < 50$), the total emulsion breakup time (black solid line) depends more on t_h compared to t_{grow} , while the latter becomes more significant as the We increases. However, the relative duration of the aforementioned times is a strong function of the emulsion configuration considered. In emulsion droplet realised in fuel sprays, the embedded water droplets could be smaller and located closer to the HFO-air interface (see following subsection). In such a configuration, the duration of the aforementioned times may be quite different. In the lower panel of **Figure 5-3**, the aforementioned time predictions are presented again (t^*) but non-dimensionalised with the shear timescale t_{sh} . The latter varies with air stream velocity u and thus with We , so different curves are illustrated compared to that in the upper panel.

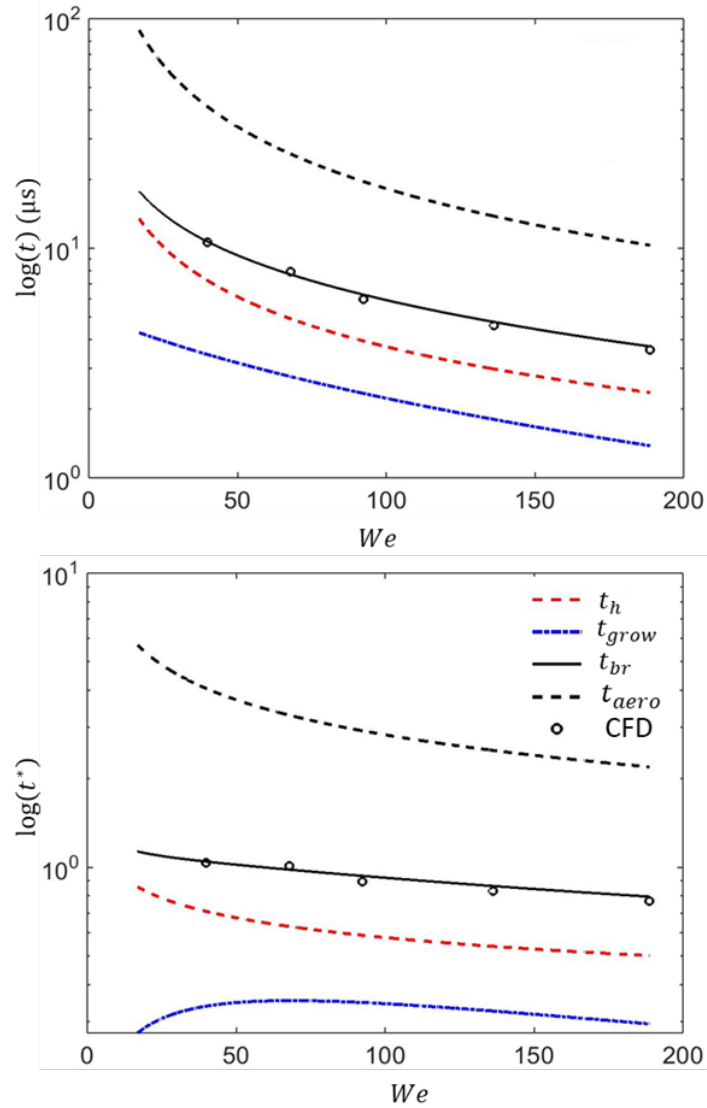


Figure 5-3: Dimensional (upper panel) and non-dimensional (lower panel) breakup time (black solid line) of an emulsion droplet alongside with heating (red dashed line) and bubble growth (blue dash-dot line) times predicted by the semi analytical model and CFD simulations (black scatter symbols) against We . Black dashed line indicates breakup initiation time of a neat HFO droplet

Next, the fitting model is used to investigate the effect of ambient conditions on emulsion breakup time. The latter is computed for a wide range of temperature and pressure values encountered in marine diesel engines. **Figure 5-5c** shows on the $p - T$ diagram the breakup time; We and δ are constant and equal to that of ref case (

Table 5.1). It is clear that the breakup time decreases as T_∞ increases while there is no clear pattern with pressure. The heating time, shown on **Figure 5-5a**, is shorter with increasing temperature (T_∞) and longer with increasing pressure. When the latter decreases, the embedded water droplet can reach faster its saturation temperature (T_{sat}); this trend is expressed through the f_T coefficient in Eq. 5-2 (Appendix A). Finally,

the bubble growth time t_{grow} , shown in **Figure 5-5b**, slightly increases with temperature while it varies non-monotonically with pressure in the examined range of 30-50 bar. The latter trend occurs because the variation in pressure affects, is a function of the inverse trends expressed by the coefficient g_p (see Appendix A) and the growth constant β in Eq. 5-3. Overall, minimum values of emulsion breakup time are predicted for maximum $p - T$ values, while its magnitude is determined mainly by the heating time period (**Figure 5-5b**) which is an order of magnitude higher ($\sim 10^{-6}$ s) compared to the bubble growth time ($\sim 10^{-7}$ s).

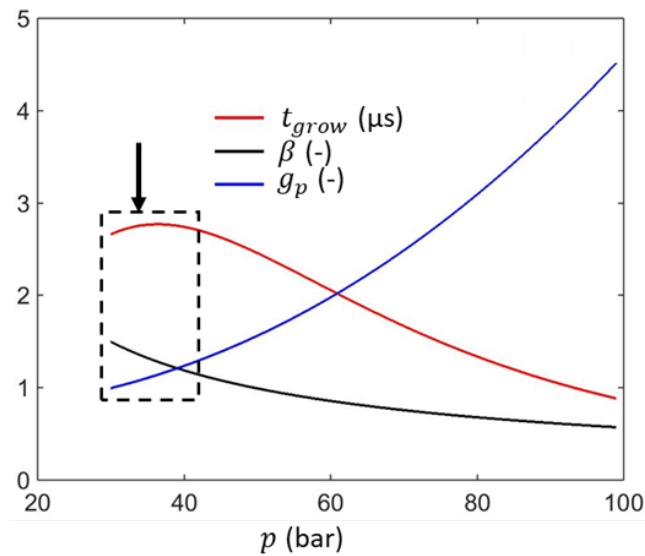


Figure 5-4: Dependence of t_{grow} (red line), β (black line) and g_p (blue line) on pressure ($T_{\infty} = 1000$ K).

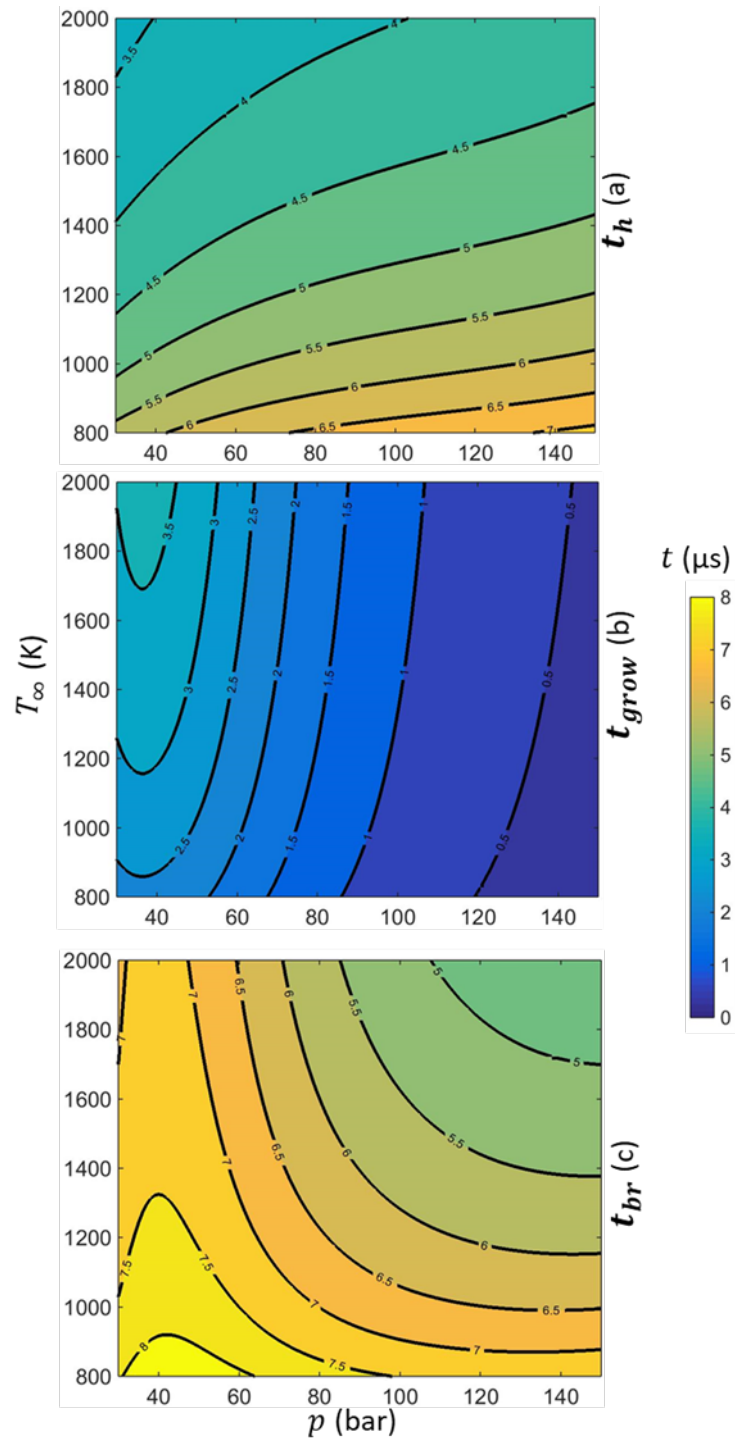


Figure 5-5: Breakup time maps for various pressure and temperature values (shown in vertical and horizontal axis respectively). The isolines correspond to different breakup times ($We = 68, \delta = 0.06, D_w/D_{oil} = 0.2$)

5.3.3 Extrapolation to emulsion configurations not studied with CFD

In actual emulsion droplet configurations, several water micro-droplets will be dispersed inside the host fuel droplet. Some of them will be quite close to the fuel-air interface and thus, will be the first to be subjected to water-vapor formation and growth. The minimum surface depth value investigated here with CFD simulations is $0.02R_f$, while the size of the embedded droplet used is $0.2R_f$, corresponding to $0.5\mu\text{m}$ and $5\mu\text{m}$, respectively. However, these length scales can be at least an order of magnitude smaller in reality.

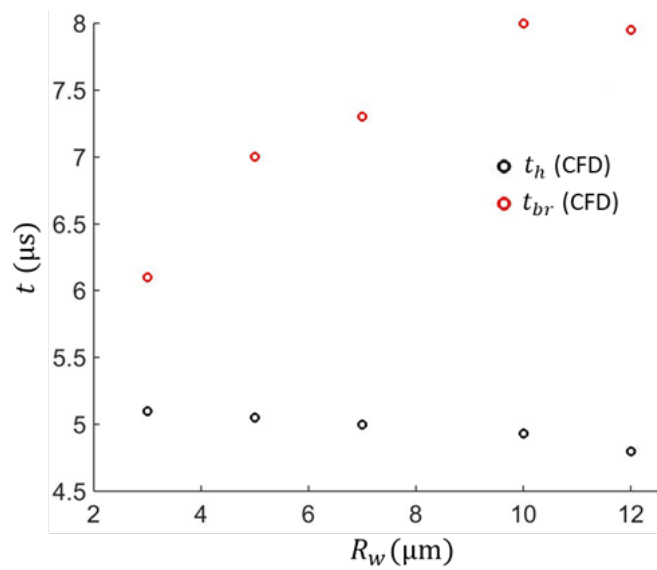


Figure 5-6: Heating (black scatter symbol) and breakup (red scatter symbol) time of an emulsion droplet against the radius of the water droplet.

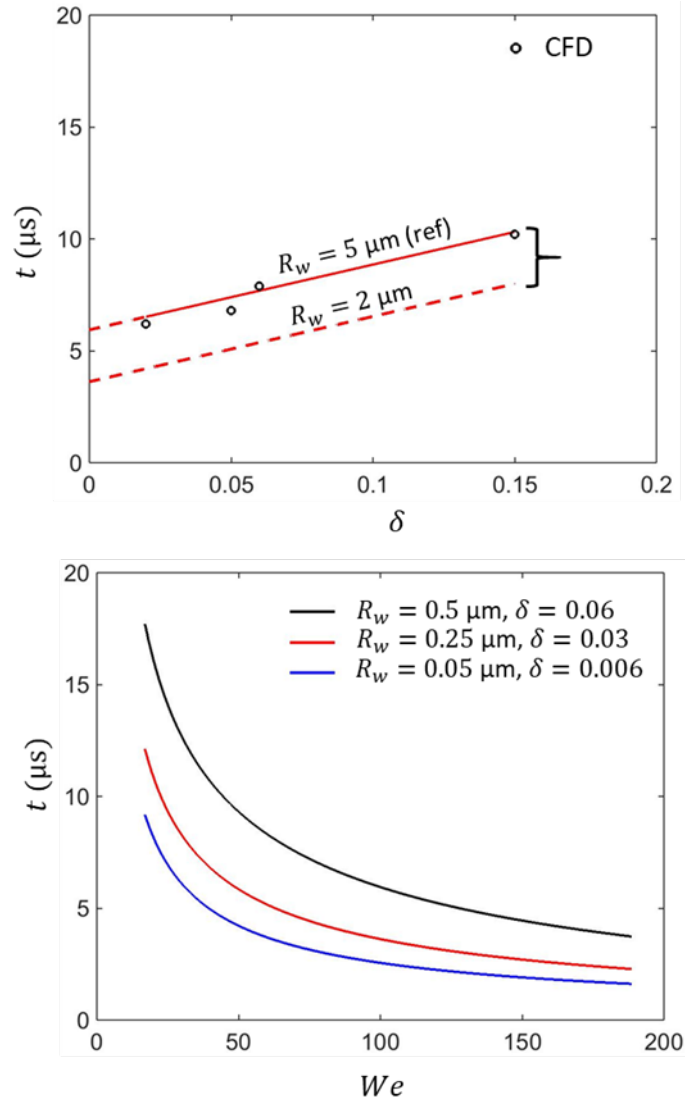


Figure 5-7: Upper panel: Emulsion breakup initiation time against water droplet surface depth for two different water droplet sizes and ref $We = 68$. Lower panel: Emulsion breakup initiation time against We for three sets of water droplet surface depth and size.

Numerical simulations obtained for the minimum surface depth and various water sub-droplet sizes (**Figure 5-6**) indicate that the heating time (t_h) remains unaffected (which can be expected), while the bubble growth time (t_{grow}) seems to follow the R_w^2 law indicated by Eq. 5-3. In the upper panel of **Figure 5-7**, the solid lines refer to the CFD model range, while the dashed ones refer to those extrapolated with the fitting model (for δ values up to 0.15). Overall, it is observed that the breakup time increases with δ in a linear way, at least for the sizes examined; this is expected since as δ increases, the heat flux has to travel a larger distance and thus, the breakup process is decelerated. This pattern is in agreement with recent CFD and analytical model results [26, 69, 71]. Moreover, it seems that for smaller water droplet sizes, the breakup time slightly

decreases, while its gradient with δ remains constant. In the lower panel of **Figure 5-7**, emulsion breakup time is predicted against We for three different sets of water droplet sizes and surface depths. The difference in predicted t_{br} between the examined configurations diminishes as We increases.

5.3.4 Model performance for multiple parameter variation

As already mentioned, for the development of the current fitting model and the estimation of the coefficients incorporated in Eq. 5-2 and Eq. 5-3, only one parameter was changing at a time. In an effort to identify differences that may arise from the simultaneous change of more than one variable, four additional CFD simulations have been performed. The varying parameters are summarized in the following Table 2; the rest are kept the same to that of the reference case.

	T_∞	p_∞	We	d_n/R_{oil}
Case 1	800	30	50	0.06
Case 2	800	30	215	0.06
Case 3	1500	30	215	0.06
Case 4	1500	30	50	0.06

Table 5.2: Operating conditions for the examined cases

The results obtained for these four cases for the breakup time are shown in **Figure 5-8** together with the corresponding predictions from the fitting model; the $\pm 10\%$ deviation lines are also indicated. Model predictions seem to be in acceptable agreement with the CFD results, suggesting that the predictions of the fitting model can be trusted over the examined range of conditions even for simultaneous variation of the influential parameters considered.

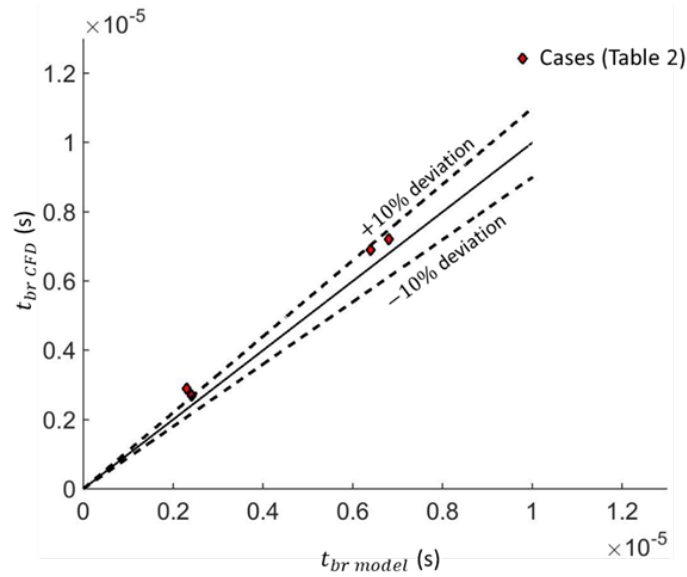


Figure 5-8: Emulsion breakup time as predicted by Eq. 5-1 (black solid line) alongside with $\pm 10\%$ deviation lines (black dashed lines) and the CFD simulations (scatter symbols)

5.4 Conclusions

Breakup of water in fuel emulsion droplets, subjected to an air flow stream, is investigated with the aid of a fitting model. The latter is capable of predicting the breakup initiation time for emulsion configurations where the parent fuel droplet contains a single water sub-droplet. The fuel properties examined correspond to those of a HFO used in marine Diesel engines. Results of the fitting model indicate that emulsion breakup is promoted by high We numbers and high $p - T$ conditions. Moreover, the effect of surface depth on breakup initiation time was investigated for emulsion droplets where the embedded water droplet is at the proximity of the fuel-air interface. It was predicted that emulsion breakup initiation time increases linearly with surface depth of the water droplet (at least for small depths); the effect of the latter becomes less significant as We increases.

Chapter 6

Conclusions and future work

6.1 Conclusions

The goal of the current thesis was to investigate the overall behavior of an emulsion droplet realised in fuel spray conditions. In those conditions, the emulsion droplet, after injected in the hot ambient air, is subjected to convective heating and aerodynamic-induced deformation and at some point the inner water droplets start boiling and the fuel-air interface eventually disintegrates leading to droplet break-up. In the numerical model, flow and energy conservation equations were solved alongside with multiple VoF equations for tracking all the liquid-liquid and liquid-air interfaces. Vapor formation inside the embedded water droplet was predicted with an algorithm that scans the internal liquid temperature field and forms a vapor bubble at a certain degree of superheat, typically found near the water-HFO interface. Next, the vapor bubbles starts growing and its vaporization rate was computed with OCASIMAT phase-change algorithm that was implemented as part of the CFD solution. Since there are no suitable experimental data for comparison, the CFD model performance was evaluated for simulating key processes of emulsion breakup phenomenon and the corresponding results are compared against analytic solutions. The OCASIMAT algorithm was evaluated, for the simple configuration of a vapor bubble growing inside an infinite superheated liquid pool, against Scriven's analytic solution. Results of the latter found to be in very good agreement with that of the CFD model for St values up to 0.03.

A benchmark case was initially simulated where a W/HFO emulsion droplet is injected, with an initial velocity $u_g = 60$ m/s, at ambient pressure $p = 30$ bar and temperature $T_g = 1000$ K. The HFO droplet consists of two water sub-droplets located in its downstream and upstream side. A single vapor bubble formatted and started expanding in each water sub-droplet after the latter reached saturation conditions. Fragmentation of the HFO-air interface occurred and vapor was injected in the ambient air. Results indicated that breakup characteristics are that of puffing. Next, a parametric study, with We number values that are typical in marine Diesel engines, was performed. The size of the emulsion droplet and the Oh number were the same for each parametric case.

Moreover, aerodynamic breakup of neat HFO droplets, under the same flow and temperature conditions and the same physical properties, was simulated. Comparing the corresponding cases, it was concluded that puffing-induced secondary atomization of emulsion droplets occurs much faster than the aerodynamic-induced one of neat HFO droplets, for the range of conditions examined ($Oh > 1$, $We < 200$).

Next, a fitting model predicting the breakup initiation time of W/HFO droplets for $p - T$ conditions realised in marine Diesel engines and subjected to a air flow stream has been presented; it's influence has been considered through the variation of the Weber number. The breakup initiation time has been expressed as the sum of two distinct time periods: (i) the time needed for the water sub-droplet to raise its temperature from T_0 to T'_{sat} and thus, for water vapor to form; this is mainly controlled by heat convection inside the parent fuel droplet; and (ii) the time period required for the formed water-vapor bubble to grow until the parent fuel droplet eventually breaks; this timescale is based on Scriven's analytical solution that predicts the growth of a water-vapor bubble inside an infinite water liquid pool. Calibration of the empirical coefficients of the derived model has been achieved via numerous CFD simulations obtained over the examined range of conditions. The obtained results have been found in acceptable agreement over the examined range of We numbers, $p - T$ conditions and surface depth of the water droplet inside the parent droplet. For low We numbers ($We < 50$), results indicate that emulsion fuel breakup time occurs 5 times faster compared to aerodynamic breakup of a base fuel; this difference diminishes as We increases. In this We range, it is also observed that duration of heating time period is longer compared to that of vapor bubble growth. Emulsion breakup initiation time was found to increase linearly with the surface depth of the water droplet for the examined range of δ ($0 - 0.15$). Regarding the effect of ambient pressure and temperature on emulsion breakup time, it was observed that minimum values were obtained for high $p - T$ values.

6.2 Future work

6.2.1 Case-specific work

The main points that further work is needed, adopting the current CFD methodology, are summarized next:

- In all the simulated cases, the CFD equations are solved in an axisymmetric domain which limits the number of the embedded water droplets in the examined configurations. Although an emulsion droplet with two embedded droplets is representative for the breakup outcome, 3-D simulation are necessary for the simulation of more than two droplets water sub-droplets which will be initially located inside the bulk of the parent droplet. Such a case may exhibit also micro-explosion induced breakup, while the migrating sub-droplets could possible experience coalescence (but this depends on the corresponding breakup timescale).
- In the emulsion simulations, it is observed that after the vapor injection at the ambient air there is phase separation between the vapor and gas phases. This occurs because different phases are mathematically treated as interpenetrating continua. Since, in the current study mainly focus on the breakup time of the emulsion droplet, this approach is reasonable. However, a more sophisticated approach would be the treatment of gas/vapor as a single volume phase and the solution of species equation. This would also define the fuel-air mixing after the emulsion breakup.
- The base fuel examined in all simulated cases is that of HFO. Different emulsion fuels should also be simulated in order to examine if they can enhance secondary breakup. For instance, potential benefits of water in Diesel emulsion droplets could be examined. Moreover, different additives besides water could also be tested. Use of alcohol in Diesel fuel emulsions have been tested in the past [103, 104] and specifically, experiments with fuel-ethanol emulsion mixtures, focusing on engine performance [105-107], have shown further reduction in PM emissions. The latter occurs since ethanol is oxygenated and thus enhances the oxidation of carbon [108]. Boiling point and superheat limit of ethanol is quite lower than that of water and substantially lower than that of HFO which makes the current methodology suitable for the study of HFO-ethanol emulsion droplets. A suitable ethanol replacement to emulsion fuel mixtures has found to be butanol [109, 110] which has higher solubility and cetane number compared to that of ethanol. With respect to current model predictions where water is

used as an additive, it is expected that emulsion fuels with additives having lower boiling point than that of water (f.i. ethanol or butanol) will breakup faster.

- The developed fitting model provides fast prediction for breakup initiation time of W/HFO emulsion droplets for a specific range of conditions. In order to provide more solid correlations that could be useful for implementation in emulsion spray codes, the range of conditions examined alongside with the fuel properties should be expanded.
- In the current work evaporation of the fuel droplet in the ambient air is not taken into account; emulsion breakup timescale computed by the CFD model is much lower compared to evaporation timescale, thus the latter mechanism is neglected. However, for high $p - T$ values close to supercritical conditions, simultaneous breakup and evaporation of the fuel droplet may occur. In order to account for this mutual effect, a high pressure evaporation model should be implemented in the CFD solution.

6.2.2 Further expansion and applications of the CFD methodology

Potential improvement of the CFD methodology and its employment for investigating other technological fields is discussed next.

- A mechanistic algorithm that accounts for vapor bubble formation has been incorporated in the CFD solution. The size of the generated bubble is predefined rather than determined by the homogeneous nucleation process. A more sophisticated model that reproduces more accurately the stochastic process of vapor bubble nucleation will provide more information regarding the first stages of bubble growth and thus the emulsion breakup outcome.
- Besides fuel technology, water in oil emulsions have high potential for cosmetic, pharmaceutical, agricultural, and food industries. For instance,

W/O emulsions can be used for the encapsulation of medicines while they are suitable for the delivery of hydrophilic compounds. The current CFD method could be a solid basis for the investigation of such applications.

Appendix A. Fitting model

Derivation of heating time period

The typical spray droplet velocity range (u_g) in HFO fueled engines is 10-100 m/s [92]; these conditions are characterized by $Pe \gg 1$, implying that the heating of the fuel droplet is convection dominated. The timescale τ_{conv} provides a rough estimation of the time needed for the fuel droplet to heat up along a distance R_{oil} and raise its temperature from T_0 to T_∞ . In the emulsion configuration examined (**Figure 5-1**), the embedded water

droplet is located at surface depth (d_h) while it will start boiling when its surface temperature becomes equal to $T'_{sat} = T_{sat} + \Delta T_s$. Moreover, the droplet is expected to deform, since it is subjected to the action of aerodynamic forces. The effect of those variables on the heating time period has been examined with CFD simulations; the corresponding coefficients f_T, f_d and f_{We} are illustrated in **Figure A-1**. It has also to be noted that the droplet heating time is also a function of the fuel thermal properties. Nevertheless, their effect is not included in the present study, since only one fuel was studied. Finally, the constant coefficients appearing in Eq. 5-2 were determined after fitting with CFD model results; the coefficient 3.6 is likely a function of Biot number, while the coefficient 8.9 appearing in f_δ is likely a function of fuel Peclet number.

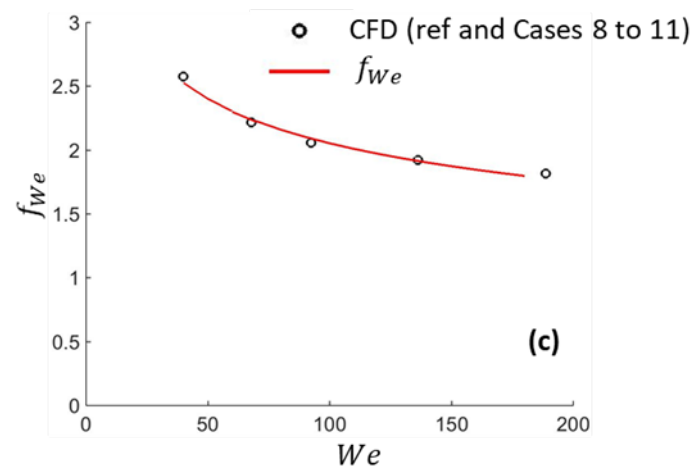
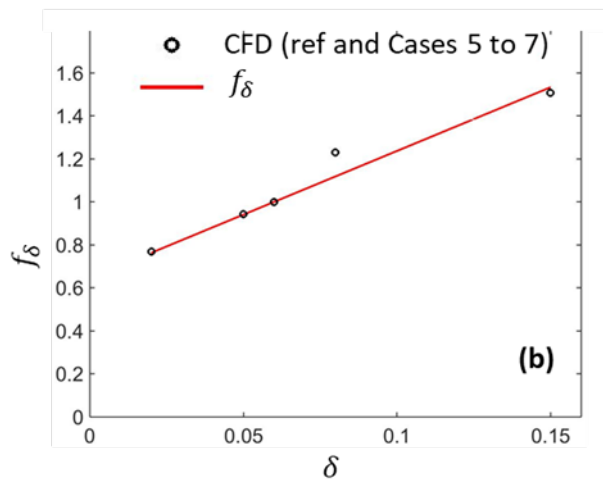
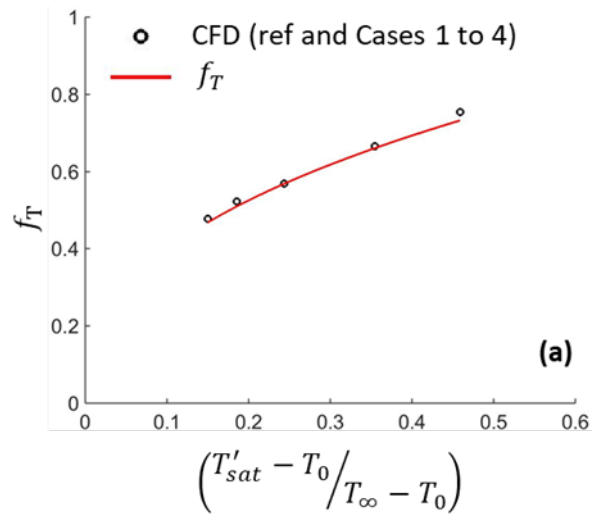


Figure A-1: Nondimensional heating time predicted by CFD simulations (black scatter symbols) against $(T'_{sat} - T_0)/(T_\infty - T_0)$ parameter (upper panel), nondimensional surface depth δ (middle panel) and nondimensional We (lower panel). Fitting functions for CFD model predictions are illustrated with red solid line.

Derivation of bubble growth time period

The derivation of the bubble growth time period t_{grow} (Eq. 5-3) starts from Scriven's analytical solution which refers to idealized conditions in which a static vapor bubble grows inside an infinite liquid pool. In the CFD cases examined, the bubble grows inside the water droplet with a much faster rate (**Figure A-2**) which was found to depend on We and $p - T$ conditions. Thus, the growth rate constant β has to be multiplied by a set of corresponding corrections factors and finally become $g_T g_P g_{We} \beta$; the performance of these factors is shown in **Figure A-3** (b, c, d).

Regarding the bubble size at the breakup instant $R_b(t_{grow})$, a careful examination of all the CFD cases presented in

Table 5.1 has shown that breakup time occurs when the bubble reaches approximately the half of the size of the host water droplet and depends slightly on We . The corresponding bubble size can be expressed as $g_{br} R_w$, where g_{br} is the dimensionless bubble size at the breakup instant; the variation of this factor is shown in **Figure A-3** (a). Combining the aforementioned comments with Scriven's equation, the latter reads $g_{br} R_w = g_T \cdot g_P \cdot g_{We} \cdot \beta \sqrt{a_w \cdot t_{grow}}$. After solving for t_{grow} , Eq. 5-3 is derived.

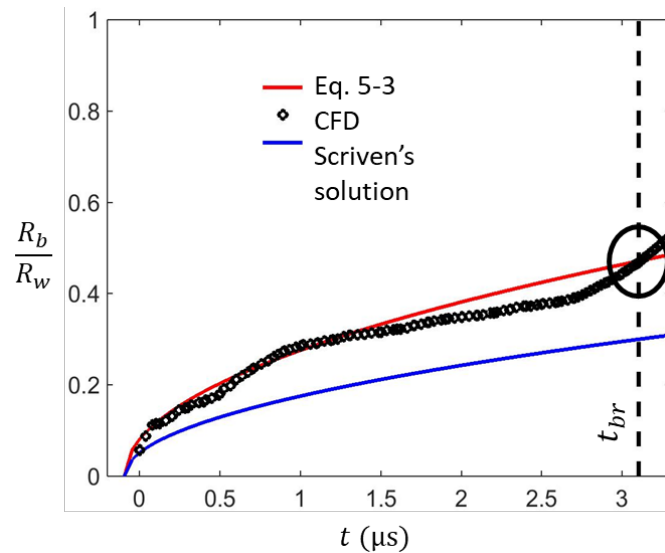


Figure A-2: Nondimensional bubble radius predicted by CFD model (black scatter symbols), Scriven solution (blue solid line) and the current analytical model (red solid line)

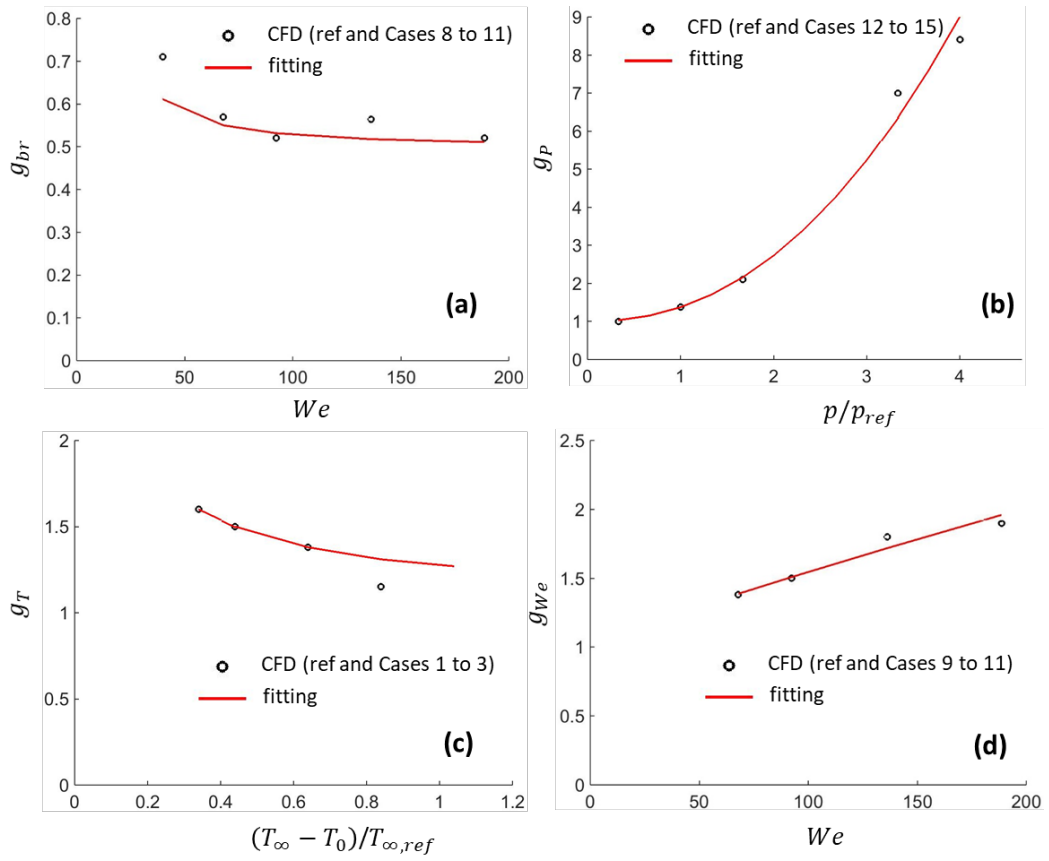


Figure A-3: Correction factors g_{br} (left upper panel), g_p (right upper panel), g_T (left lower panel) and g_{We} (right lower panel) calibrated from CFD model predictions (black scatter symbols)

Publications

During my 3-year research I had the opportunity to travel, participate and present my ongoing work in international conferences, while I was fortunate to publish my findings in well-respected international scientific journals. The list of my achievements is given below:

Conferences (oldest first)

1. S. Fostiropoulos, G. Strotos, N. Nikolopoulos and M. Gavaises, 2017, "Numerical investigation of W/O emulsion droplet breakup under realistic spray conditions", IICR 2019, Chania, Greece (poster and presentation).
2. S. Fostiropoulos, G. Strotos, N. Nikolopoulos and M. Gavaises, 2018, "A new numerical model for heat and mass transfer in explosive boiling conditions", FLOW 2018, Kozani, Greece (paper and presentation).
3. S. Fostiropoulos, I. Malgarinos, G. Strotos, N. Nikolopoulos, E. Kakaras, P. Koukouvinis and M. Gavaises, 2017, "Role of heat transfer in bubble dynamics neglecting phase change", ILASS Europe 2017, Valencia, Spain (paper and presentation).
4. S. Fostiropoulos, I. Malgarinos, G. Strotos, N. Nikolopoulos, E. Kakaras and M. Gavaises, 2017, " Role of heat transfer in bubble dynamics neglecting phase change ", IICR 2017, Chania, Greece (poster).

Journal papers

1. S. Fostiropoulos, G. Strotos, N. Nikolopoulos and M. Gavaises, 2020, "Numerical investigation of heavy fuel oil droplet breakup enhancement with water emulsions", Fuel, vol 278
2. S. Fostiropoulos, G. Strotos, N. Nikolopoulos and M. Gavaises, 2020, "Numerical investigation of heavy fuel oil droplet breakup enhancement with water emulsions", International Journal of Heat and Mass transfer

Bibliography

1. Fostiropoulos, S., G. Strotos, N. Nikolopoulos, and M. Gavaises, *Numerical investigation of heavy fuel oil droplet breakup enhancement with water emulsions*. Fuel, 2020. **278**: p. 118381 DOI: <https://doi.org/10.1016/j.fuel.2020.118381>.
2. Avedisian, C. and I. Glassman, *Superheating and boiling of water in hydrocarbons at high pressures*. International Journal of Heat and Mass Transfer, 1981. **24**: p. 695-706 DOI: [https://doi.org/10.1016/0017-9310\(81\)90013-2](https://doi.org/10.1016/0017-9310(81)90013-2).
3. Avedisian, C.T., *The homogeneous nucleation limits of liquids*. Journal of physical and chemical reference data, 1985. **14**: p. 695-729 DOI: <https://doi.org/10.1063/1.555734>.
4. Perez-Raya, I. and S.G. Kandlikar, *Discretization and implementation of a sharp interface model for interfacial heat and mass transfer during bubble growth*. International Journal of Heat and Mass Transfer, 2018. **116**: p. 30-49 DOI: <https://doi.org/10.1016/j.ijheatmasstransfer.2017.08.106>.
5. Fostiropoulos, S., G. Strotos, N. Nikolopoulos, and M. Gavaises, *A simple model for breakup time prediction of water-heavy fuel oil emulsion droplets*. International Journal of Heat and Mass Transfer, 2020. **Volume 164** DOI: <https://doi.org/10.1016/j.ijheatmasstransfer.2020.120581>.
6. Outlook, B.E., *2019 edition*. London, United Kingdom 2019, 2019.
7. The Outlook for Energy: A View to 2040. Exxon Mobil Corporation, 2019.
8. Reitz, R., H. Ogawa, R. Payri, T. Fansler, S. Kokjohn, Y. Moriyoshi, A. Agarwal, D. Arcoumanis, D. Assanis, and C. Bae, *IJER editorial: The future of the internal combustion engine*. 2020, SAGE Publications Sage UK: London, England.
9. IEA (2019), W.E.O., IEA, Paris <https://www.iea.org/reports/world-energy-outlook-2019>.
10. Kumar, M.S., J. Bellettre, and M. Tazerout, *The use of biofuel emulsions as fuel for diesel engines: a review*. 2009, SAGE Publications Sage UK: London, England.
11. Qin, D., Z. Chen, K. Averyt, H. Miller, S. Solomon, M. Manning, M. Marquis, and M. Tignor, *IPCC, 2007: Summary for Policymakers*. 2007.
12. Jegannathan, K.R., S. Abang, D. Poncelet, E.S. Chan, and P. Ravindra, *Production of biodiesel using immobilized lipase—a critical review*. Critical reviews in biotechnology, 2008. **28**: p. 253-264 DOI: <https://doi.org/10.1080/07388550802428392>.
13. Tan, T., J. Lu, K. Nie, L. Deng, and F. Wang, *Biodiesel production with immobilized lipase: a review*. Biotechnology advances, 2010. **28**: p. 628-634 DOI: <https://doi.org/10.1016/j.biotechadv.2010.05.012>.
14. Farfaletti, A., C. Astorga, G. Martini, U. Manfredi, A. Mueller, M. Rey, G. De Santi, A. Krasenbrink, and B.R. Larsen, *Effect of water/fuel emulsions and a cerium-based combustion improver additive on HD and LD diesel exhaust emissions*. Environmental science & technology, 2005. **39**: p. 6792-6799.
15. Samec, N., B. Kegl, and R.W. Dibble, *Numerical and experimental study of water/oil emulsified fuel combustion in a diesel engine*. Fuel, 2002. **81**: p. 2035-2044.
16. Suresh, V., K. Amirthagadeswaran, S. Vijayakumar, and B. Varun, *Emission characteristics of diesel engine using water-in-diesel emulsified fuel and its CFD analysis*. Int. J. Appl. Environ. Sci, 2014. **9**: p. 2739-2749.

17. Fu, W.B., L.Y. Hou, L. Wang, and F.H. Ma, *A unified model for the micro-explosion of emulsified droplets of oil and water*. Fuel Processing Technology, 2002. **79**: p. 107-119.
18. Nazha, M. and R. Crookes. *Effect of water content on pollutant formation in a burning spray of water-in-diesel fuel emulsion*. in *Symposium (International) on Combustion*. 1985. Elsevier.
19. Tauzia, X., A. Maiboom, and S.R. Shah, *Experimental study of inlet manifold water injection on combustion and emissions of an automotive direct injection diesel engine*. Energy, 2010. **35**: p. 3628-3639 DOI: <https://doi.org/10.1016/j.energy.2010.05.007>.
20. Kumar, M.S., J. Bellettre, and M. Tazerout, *Investigations on a CI engine using animal fat and its emulsions with water and methanol as fuel*. 2005, SAE Technical Paper.
21. Holtbecker, R. and M. Geist, *Exhaust emissions reduction technology for Sulzer marine diesel engines: general aspects*. Wartsila NSD Switzerland Ltd, Winterthur, 1998: p. 5-27.
22. Majewski, A., *Water in Diesel Combustion*. 2015.
23. Basha, J.S. and R. Anand, *An experimental study in a CI engine using nanoadditive blended water–diesel emulsion fuel*. International journal of green energy, 2011. **8**: p. 332-348 DOI: <https://doi.org/10.1080/15435075.2011.557844>.
24. Kadota, T. and H. Yamasaki, *Recent advances in the combustion of water fuel emulsion*. Progress in energy and combustion science, 2002. **28**: p. 385-404 DOI: [https://doi.org/10.1016/S0360-1285\(02\)00005-9](https://doi.org/10.1016/S0360-1285(02)00005-9).
25. Avedisian, C. and R. Andres, *Bubble nucleation in superheated liquid–liquid emulsions*. Journal of colloid and interface science, 1978. **64**: p. 438-453 DOI: [https://doi.org/10.1016/0021-9797\(78\)90386-7](https://doi.org/10.1016/0021-9797(78)90386-7).
26. Shinjo, J., J. Xia, L. Ganippa, and A. Megaritis, *Physics of puffing and microexplosion of emulsion fuel droplets*. Physics of Fluids (1994-present), 2014. **26**: p. 103302 DOI: <https://doi.org/10.1063/1.4897918>.
27. Shinjo, J., J. Xia, A. Megaritis, L. Ganippa, and R. Cracknell, *Modeling temperature distribution inside an emulsion fuel droplet under convective heating: a key to predicting microexplosion and puffing*. Atomization and Sprays, 2016. **26** DOI: 10.1615/AtomizSpr.2015013302.
28. Brennen, C.E., *Cavitation and bubble dynamics*. 2014: Cambridge University Press.
29. Roesle, M.L. and F. Kulacki, *Boiling of Dilute Emulsions □ Toward a New Modeling Framework*. Industrial & Engineering Chemistry Research, 2010. **49**: p. 5188-5196 DOI: <https://doi.org/10.1021/ie9013259>.
30. Welch, S.W.J. and J. Wilson, *A Volume of Fluid Based Method for Fluid Flows with Phase Change*. Journal of Computational Physics, 2000. **160**: p. 662-682 DOI: <http://dx.doi.org/10.1006/jcph.2000.6481>.
31. Son, G. and V.K. Dhir, *Numerical simulation of film boiling near critical pressures with a level set method*. Journal of Heat Transfer, 1998. **120**: p. 183-192 DOI: <https://doi.org/10.1115/1.2830042>.
32. Juric, D. and G. Tryggvason, *Computations of boiling flows*. International Journal of Multiphase Flow, 1998. **24**: p. 387-410 DOI: [https://doi.org/10.1016/S0301-9322\(97\)00050-5](https://doi.org/10.1016/S0301-9322(97)00050-5).
33. Sato, Y. and B. Ničeno, *A sharp-interface phase change model for a mass-conservative interface tracking method*. Journal of Computational Physics, 2013. **249**: p. 127-161 DOI: <https://doi.org/10.1016/j.jcp.2013.04.035>.

34. Kunkelmann, C. and P. Stephan, *CFD simulation of boiling flows using the volume-of-fluid method within OpenFOAM*. Numerical Heat Transfer, Part A: Applications, 2009. **56**: p. 631-646 DOI: <https://doi.org/10.1080/10407780903423908>.
35. Magnini, M., B. Pulvirenti, and J.R. Thome, *Numerical investigation of hydrodynamics and heat transfer of elongated bubbles during flow boiling in a microchannel*. International Journal of Heat and Mass Transfer, 2013. **59**: p. 451-471 DOI: <https://doi.org/10.1016/j.ijheatmasstransfer.2012.12.010>.
36. Rayleigh, L., VIII. *On the pressure developed in a liquid during the collapse of a spherical cavity*. The London, Edinburgh, and Dublin Philosophical Magazine and Journal of Science, 1917. **34**: p. 94-98 DOI: <https://doi.org/10.1080/14786440808635681>.
37. Forster, H. and N. Zuber, *Dynamics of vapor bubbles and boiling heat transfer*. AIChE Journal, 1955. **1**: p. 531-535 DOI: <https://doi.org/10.1002/aic.690010425>.
38. Plesset, M.S. and S. Zwick, *A nonsteady heat diffusion problem with spherical symmetry*. Journal of Applied Physics, 1952. **23**: p. 95-98 DOI: <https://doi.org/10.1063/1.1701985>.
39. Scriven, L., *On the dynamics of phase growth*. Chemical engineering science, 1959. **10**: p. 1-13 DOI: [https://doi.org/10.1016/0009-2509\(59\)80019-1](https://doi.org/10.1016/0009-2509(59)80019-1).
40. Mikic, B., W. Rohsenow, and P. Griffith, *On bubble growth rates*. International Journal of Heat and Mass Transfer, 1970. **13**: p. 657-666 DOI: [https://doi.org/10.1016/0017-9310\(70\)90040-2](https://doi.org/10.1016/0017-9310(70)90040-2).
41. Plesset, M. and S.A. Zwick, *The growth of vapor bubbles in superheated liquids*. Journal of Applied Physics, 1954. **25**: p. 493-500 DOI: <https://doi.org/10.1063/1.1721668>.
42. Shepherd, J.E. and B. Sturtevant, *Rapid evaporation at the superheat limit*. Journal of Fluid Mechanics, 2006. **121**: p. 379-402 DOI: 10.1017/S0022112082001955.
43. Frost, D., *Dynamics of explosive boiling of a droplet*. The Physics of fluids, 1988. **31**: p. 2554-2561 DOI: <https://doi.org/10.1063/1.866608>.
44. Ochoterena, R., A. Lif, M. Nydén, S. Andersson, and I. Denbratt, *Optical studies of spray development and combustion of water-in-diesel emulsion and microemulsion fuels*. Fuel, 2010. **89**: p. 122-132 DOI: <https://doi.org/10.1016/j.fuel.2009.06.039>.
45. Park, S., S. Woo, H. Kim, and K. Lee, *The characteristic of spray using diesel water emulsified fuel in a diesel engine*. Applied energy, 2016. **176**: p. 209-220 DOI: <https://doi.org/10.1016/j.apenergy.2016.05.069>.
46. Zhu, M., Z. Zhang, Y. Zhang, P. Liu, and D. Zhang, *An experimental investigation into the ignition and combustion characteristics of single droplets of biochar water slurry fuels in air*. Applied energy, 2017. **185**: p. 2160-2167 DOI: <https://doi.org/10.1016/j.apenergy.2015.11.087>.
47. Califano, V., R. Calabria, and P. Massoli, *Experimental evaluation of the effect of emulsion stability on micro-explosion phenomena for water-in-oil emulsions*. Fuel, 2014. **117**: p. 87-94 DOI: <https://doi.org/10.1016/j.fuel.2013.08.073>.
48. Mura, E., P. Massoli, C. Josset, K. Loubar, and J. Bellettre, *Study of the micro-explosion temperature of water in oil emulsion droplets during the Leidenfrost effect*. Experimental Thermal and Fluid Science, 2012. **43**: p. 63-70 DOI: <https://doi.org/10.1016/j.expthermflusci.2012.03.027>.
49. Segawa, D., H. Yamasaki, T. Kadota, H. Tanaka, H. Enomoto, and M. Tsue, *Water-coalescence in an oil-in-water emulsion droplet burning under microgravity*. Proceedings of the Combustion Institute, 2000. **28**: p. 985-990 DOI: [https://doi.org/10.1016/S0082-0784\(00\)80305-7](https://doi.org/10.1016/S0082-0784(00)80305-7).

50. Nas, S. and G. Tryggvason, *Thermocapillary interaction of two bubbles or drops*. International journal of multiphase flow, 2003. **29**: p. 1117-1135 DOI: [https://doi.org/10.1016/S0301-9322\(03\)00084-3](https://doi.org/10.1016/S0301-9322(03)00084-3).
51. Wozniak, G., R. Balasubramaniam, P. Hadland, and R. Subramanian, *Temperature fields in a liquid due to the thermocapillary motion of bubbles and drops*. Experiments in fluids, 2001. **31**: p. 84-89 DOI: <https://doi.org/10.1007/s003480000262>.
52. Moussa, O., D. Tarlet, P. Massoli, and J. Bellettre, *Parametric study of the micro-explosion occurrence of W/O emulsions*. International Journal of Thermal Sciences, 2018. **133**: p. 90-97 DOI: <https://doi.org/10.1016/j.ijthermalsci.2018.07.016>.
53. Avulapati, M.M., T. Megaritis, J. Xia, and L. Ganippa, *Experimental understanding on the dynamics of micro-explosion and puffing in ternary emulsion droplets*. Fuel, 2019. **239**: p. 1284-1292 DOI: <https://doi.org/10.1016/j.fuel.2018.11.112>.
54. Shen, S., K. Sun, Z. Che, T. Wang, M. Jia, and J. Cai, *An experimental investigation of the heating behaviors of droplets of emulsified fuels at high temperature*. Applied Thermal Engineering, 2019. **161**: p. 114059 DOI: <https://doi.org/10.1016/j.applthermaleng.2019.114059>.
55. Abdul Karim, Z., M.Y. Khan, and A.R.A. Aziz, *Evolution of Microexplosion Phenomenon in Parent–Child Droplets of Water in Biodiesel Emulsions Enhanced by Different Surfactant Dosages and Hydrophilic–Lipophilic Balance Values*. Journal of Energy Resources Technology, 2019. **141** DOI: <https://doi.org/10.1115/1.4043553>.
56. Moussa, O., D. Francelino, D. Tarlet, P. Massoli, and J. Bellettre, *Insight of a water in oil emulsion dropl under Leidenfrost heating using laser-induced fluorescence optical diagnostics*. Atomization and Sprays, 2019. **29** DOI: 10.1615/AtomizSpr.2019029233.
57. Antonov, D., M. Piskunov, P. Strizhak, D. Tarlet, and J. Bellettre, *Dispersed phase structure and micro-explosion behavior under different schemes of water-fuel droplets heating*. Fuel, 2020. **259**: p. 116241 DOI: <https://doi.org/10.1016/j.fuel.2019.116241>.
58. Antonov, D.V., M.V. Piskunov, and P.A. Strizhak, *Explosive disintegration of two-component drops under intense conductive, convective, and radiant heating*. Applied Thermal Engineering, 2019. **152**: p. 409-419 DOI: <https://doi.org/10.1016/j.applthermaleng.2019.02.099>.
59. Antonov, D., M. Piskunov, and P. Strizhak, *Breakup and explosion of droplets of two immiscible fluids and emulsions*. International Journal of Thermal Sciences, 2019. **142**: p. 30-41 DOI: <https://doi.org/10.1016/j.ijthermalsci.2019.04.011>.
60. Omar, M., T. Dominique, M. Patrizio, and B. Jérôme, *Investigation on the conditions leading to the micro-explosion of emulsified fuel droplet using two colors LIF method*. Experimental Thermal and Fluid Science, 2020: p. 110106 DOI: <https://doi.org/10.1016/j.expthermflusci.2020.110106>.
61. Rao, D.C.K. and S. Basu, *Phenomenology of disruptive breakup mechanism of a levitated evaporating emulsion droplet*. Experimental Thermal and Fluid Science, 2020. **115**: p. 110086 DOI: <https://doi.org/10.1016/j.expthermflusci.2020.110086>.
62. Fuchihata, M., T. Ida, and Y. Mizutani, *Observation of microexplosions in spray flames of light oil water emulsions. II. Influence of temporal and spatial resolution in high speed videography*. Nippon Kikai Gakkai Ronbunshu B Hen(Transactions of the Japan Society of Mechanical Engineers Part B)(Japan), 2003. **15**: p. 1503-1508.

63. Watanabe, H. and K. Okazaki, *Visualization of secondary atomization in emulsified-fuel spray flow by shadow imaging*. Proceedings of the Combustion Institute, 2013. **34**: p. 1651-1658 DOI: <https://doi.org/10.1016/j.proci.2012.07.005>.
64. Shusser, M. and D. Weihs, *Explosive boiling of a liquid droplet*. International journal of multiphase flow, 1999. **25**: p. 1561-1573 DOI: [https://doi.org/10.1016/S0301-9322\(98\)00078-0](https://doi.org/10.1016/S0301-9322(98)00078-0).
65. Shepherd, J. and B. Sturtevant, *Rapid evaporation at the superheat limit*. Journal of Fluid Mechanics, 1982. **121**: p. 379-402 DOI: <http://dx.doi.org/10.1017/S0022112082001955>.
66. Zeng, Y. and F.L. Chia-fon, *Modeling droplet breakup processes under micro-explosion conditions*. Proceedings of the Combustion Institute, 2007. **31**: p. 2185-2193 DOI: <https://doi.org/10.1016/j.proci.2006.07.237>.
67. Watanabe, H., Y. Matsushita, H. Aoki, and T. Miura, *Numerical simulation of emulsified fuel spray combustion with puffing and micro-explosion*. Combustion and flame, 2010. **157**: p. 839-852 DOI: <https://doi.org/10.1016/j.combustflame.2010.01.013>.
68. Watanabe, H., Y. Suzuki, T. Harada, H. Aoki, and T. Miura, *Development of a mathematical model for predicting water vapor mass generated in micro-explosion*. Energy, 2011. **36**: p. 4089-4096 DOI: <https://doi.org/10.1016/j.energy.2011.04.038>.
69. Girin, O.G., *Dynamics of the emulsified fuel drop microexplosion*. Atomization and Sprays, 2017. **27** DOI: 10.1615/AtomizSpr.2017017143.
70. Nissar, Z., O. Rybdylova, S. Sazhin, M. Heikal, A.R.B. Aziz, and M.A. Ismael, *A model for puffing/microexplosions in water/fuel emulsion droplets*. International Journal of Heat and Mass Transfer, 2020. **149**: p. 119208 DOI: <https://doi.org/10.1016/j.ijheatmasstransfer.2019.119208>.
71. Sazhin, S., O. Rybdylova, C. Crua, M. Heikal, M. Ismael, Z. Nissar, and A.R.B. Aziz, *A simple model for puffing/micro-explosions in water-fuel emulsion droplets*. International Journal of Heat and Mass Transfer, 2019. **131**: p. 815-821 DOI: <https://doi.org/10.1016/j.ijheatmasstransfer.2018.11.065>.
72. Sazhin, S.S., T. Bar-Kohany, Z. Nissar, D. Antonov, P.A. Strizhak, and O.D. Rybdylova, *A new approach to modelling micro-explosions in composite droplets*. International Journal of Heat and Mass Transfer, 2020. **161**: p. 120238 DOI: <https://doi.org/10.1016/j.ijheatmasstransfer.2020.120238>.
73. Zhang, Y., Y. Huang, R. Huang, S. Huang, Y. Ma, S. Xu, and Z. Wang, *A new puffing model for a droplet of butanol-hexadecane blends*. Applied Thermal Engineering, 2018. **133**: p. 633-644 DOI: <https://doi.org/10.1016/j.applthermaleng.2018.01.096>.
74. Guildenbecher, D., C. López-Rivera, and P. Sojka, *Secondary atomization*. Experiments in Fluids, 2009. **46**: p. 371 DOI: <https://doi.org/10.1007/s00348-008-0593-2>.
75. Nicholls, J. and A. Ranger, *Aerodynamic shattering of liquid drops*. Aiaa Journal, 1969. **7**: p. 285-290 DOI: <https://doi.org/10.2514/3.5087>.
76. Tryggvason, G., R. Scardovelli, and S. Zaleski, *Direct numerical simulations of gas-liquid multiphase flows*. 2011: Cambridge University Press.
77. Hirt, C.W. and B.D. Nichols, *Volume of fluid (VOF) method for the dynamics of free boundaries*. Journal of Computational Physics, 1981. **39**: p. 201-225 DOI: [http://dx.doi.org/10.1016/0021-9991\(81\)90145-5](http://dx.doi.org/10.1016/0021-9991(81)90145-5).

78. Malik, M., E.S.C. Fan, and M. Bussmann, *Adaptive VOF with curvature-based refinement*. International Journal for Numerical Methods in Fluids, 2007. **55**: p. 693-712 DOI: <https://doi.org/10.1002/flid.1490>.
79. Brackbill, J., D.B. Kothe, and C. Zemach, *A continuum method for modeling surface tension*. Journal of computational physics, 1992. **100**: p. 335-354.
80. Fluent, A., *Release 16.0*, ANSYS. 2014, Inc.
81. Patankar, S., *Chapter Seven-Finishing Touches*. Numerical Heat Transfer and Fluid Flow, New York, 1980.
82. Malgarinos, I., N. Nikolopoulos, and M. Gavaises, *Coupling a local adaptive grid refinement technique with an interface sharpening scheme for the simulation of two-phase flow and free-surface flows using VOF methodology*. Journal of Computational Physics, 2015. **300**: p. 732-753 DOI: <http://dx.doi.org/10.1016/j.jcp.2015.08.004>.
83. Basaran, O.A., *Nonlinear oscillations of viscous liquid drops*. Journal of Fluid Mechanics, 1992. **241**: p. 169-198 DOI: <https://doi.org/10.1017/S002211209200199X>.
84. Tanguy, S., M. Sagan, B. Lalanne, F. Couderc, and C. Colin, *Benchmarks and numerical methods for the simulation of boiling flows*. Journal of Computational Physics, 2014. **264**: p. 1-22 DOI: <https://doi.org/10.1016/j.jcp.2014.01.014>.
85. *NIST (National Institute of Standards and Technology)*.
86. Abramzon, B. and W. Sirignano, *Droplet vaporization model for spray combustion calculations*. International journal of heat and mass transfer, 1989. **32**: p. 1605-1618 DOI: [https://doi.org/10.1016/0017-9310\(89\)90043-4](https://doi.org/10.1016/0017-9310(89)90043-4).
87. Stefanitsis, D., I. Malgarinos, G. Strotos, N. Nikolopoulos, E. Kakaras, and M. Gavaises, *Numerical investigation of the aerodynamic breakup of Diesel and heavy fuel oil droplets*. International Journal of Heat and Fluid Flow, 2017. **68**: p. 203-215 DOI: 10.1016/j.ijheatfluidflow.2017.10.012.
88. Ubbink, O. and R. Issa, *A method for capturing sharp fluid interfaces on arbitrary meshes*. Journal of Computational Physics, 1999. **153**: p. 26-50.
89. Barth, T. and D. Jespersen. *The design and application of upwind schemes on unstructured meshes*. in *27th Aerospace sciences meeting*. 1989. DOI: <https://doi.org/10.2514/6.1989-366>.
90. Kyriakides, N., C. Chryssakis, and L. Kaiktsis, *Influence of heavy fuel properties on spray atomization for marine diesel engine applications*. 2009, SAE Technical Paper.
91. Riazi, M., *Characterization and properties of petroleum fractions*. Vol. 50. 2005: ASTM international.
92. Wadhwa, A.R., V. Magi, and J. Abraham, *Transient deformation and drag of decelerating drops in axisymmetric flows*. Physics of Fluids, 2007. **19**: p. 113301 DOI: <https://doi.org/10.1063/1.2800038>.
93. Khan, M.Y., Z.A. Karim, A.R.A. Aziz, and I.M. Tan, *A case study on the influence of selected parameters on microexplosion behavior of water in biodiesel emulsion droplets*. Journal of Energy Resources Technology, 2017. **139**: p. 022203 DOI: <https://doi.org/10.1115/1.4034230>.
94. Kimoto, K., Y. Owashii, and Y. Omae, *The vaporizing behavior of the fuel droplet of water-in-oil emulsion on the hot surface*. Bulletin of JSME, 1986. **29**: p. 4247-4255 DOI: <https://doi.org/10.1299/jsme1958.29.4247>.
95. Pilch, M. and C. Erdman, *Use of breakup time data and velocity history data to predict the maximum size of stable fragments for acceleration-induced breakup of a liquid drop*. International journal of multiphase flow, 1987. **13**: p. 741-757 DOI: [https://doi.org/10.1016/0301-9322\(87\)90063-2](https://doi.org/10.1016/0301-9322(87)90063-2).

96. Stefanitsis, D., I. Malgarinos, G. Strotos, N. Nikolopoulos, E. Kakaras, and M. Gavaises, *Numerical investigation of the aerodynamic breakup of droplets in tandem*. International Journal of Multiphase Flow, 2019. **113**: p. 289-303 DOI: <https://doi.org/10.1016/j.ijmultiphaseflow.2018.10.015>.
97. Strotos, G., M. Gavaises, A.P. Theodorakakos, and G.C. Bergeles. *Evaporation of a suspended multicomponent droplet under convective conditions*. in *Proceedings of CHT-08 ICHMT International Symposium on Advances in Computational Heat Transfer*. 2008. Begel House Inc. DOI: <http://dx.doi.org/10.1615/ICHMT.2008.CHT.2460>.
98. Strotos, G., I. Malgarinos, N. Nikolopoulos, and M. Gavaises, *Predicting the evaporation rate of stationary droplets with the VOF methodology for a wide range of ambient temperature conditions*. International Journal of Thermal Sciences, 2016. **109**: p. 253-262 DOI: <https://doi.org/10.1016/j.ijthermalsci.2016.06.022>.
99. Strotos, G., I. Malgarinos, N. Nikolopoulos, and M. Gavaises, *Predicting droplet deformation and breakup for moderate Weber numbers*. International Journal of Multiphase Flow, 2016. **85**: p. 96-109 DOI: <https://doi.org/10.1016/j.ijmultiphaseflow.2016.06.001>.
100. Strotos, G., I. Malgarinos, N. Nikolopoulos, M. Gavaises, K.-S. Nikas, and K. Moustris, *Determination of the aerodynamic droplet breakup boundaries based on a total force approach*. International Journal of Heat and Fluid Flow, 2018. **69**: p. 164-173 DOI: <https://doi.org/10.1016/j.ijheatfluidflow.2018.01.001>.
101. Hinze, J., *Fundamentals of the hydrodynamic mechanism of splitting in dispersion processes*. AIChE Journal, 1955. **1**: p. 289-295 DOI: <https://doi.org/10.1002/aic.690010303>.
102. Hsiang, L.-P. and G.M. Faeth, *Near-limit drop deformation and secondary breakup*. International journal of multiphase flow, 1992. **18**: p. 635-652 DOI: [https://doi.org/10.1016/0301-9322\(92\)90036-G](https://doi.org/10.1016/0301-9322(92)90036-G).
103. Moon, S., T. Tsujimura, M. Oguma, Z. Chen, Z. Huang, and T. Saitou, *Mixture condition, combustion and sooting characteristics of ethanol–diesel blends in diffusion flames under various injection and ambient conditions*. Fuel, 2013. **113**: p. 128-139.
104. Pan, K.-L. and M.-C. Chiu, *Droplet combustion of blended fuels with alcohol and biodiesel/diesel in microgravity condition*. Fuel, 2013. **113**: p. 757-765.
105. Hulwan, D.B. and S.V. Joshi, *Performance, emission and combustion characteristic of a multicylinder DI diesel engine running on diesel–ethanol–biodiesel blends of high ethanol content*. Applied Energy, 2011. **88**: p. 5042-5055.
106. Pidol, L., B. Lecointe, L. Starck, and N. Jeuland, *Ethanol–biodiesel–diesel fuel blends: performances and emissions in conventional diesel and advanced low temperature combustions*. Fuel, 2012. **93**: p. 329-338.
107. Rajasekar, E., A. Murugesan, R. Subramanian, and N. Nedunchezian, *Review of NOx reduction technologies in CI engines fuelled with oxygenated biomass fuels*. Renewable and Sustainable Energy Reviews, 2010. **14**: p. 2113-2121.
108. Shinjo, J., J. Xia, L. Ganippa, and A. Megaritis, *Puffing-enhanced fuel/air mixing of an evaporating n -decane/ethanol emulsion droplet and a droplet group under convective heating*. Journal of Fluid Mechanics, 2016. **793**: p. 444-476.
109. Altun, S., C. Oner, F. Yasar, and H. Adin, *Effect of n-butanol blending with a blend of diesel and biodiesel on performance and exhaust emissions of a diesel engine*. Industrial & engineering chemistry research, 2011. **50**: p. 9425-9430.
110. Liu, Y., W. Cheng, M. Huo, C. Lee, J. Li, C.C. City, J.L. Province, and W. Street. *Effects of micro-explosion on butanol-biodiesel-diesel spray and combustion*. in

Proceedings of the ILASS-Americas 22nd Annual Conference on Liquid Atomization and Spray Systems, Cincinnati, OH, USA. 2010.